A Dissertation Submitted to
Shanghai Jiao Tong University for the degree of
Doctor of Philosophy in Physics

Search for new phenomena in dijet events with quark/gluon tagger using the ATLAS detector

Wanyun Su

Tsung-Dao Lee Institute
Shanghai Jiao Tong University
Shanghai, P.R.China
November 30, 2023

申请上海交通大学博士学位论文

在 ATLAS 双喷注末态中利用夸克/胶子标定寻找新粒子

作者：苏琬云

导师：李数、Shih-Chieh Hsu (University of Washington, Seattle)

李政道研究所
上海交通大学

2023 年 11 月 30 日

上海交通大学
学位论文原创性声明

本人郑重声明：所呈交的学位论文，是本人在导师的指导下，独立进行研究工作所取得的成果。除文中已经注明引用的内容外，本论文不包含任何其他个人或集体已经发表或撰写过的作品成果。对本文的研究做出重要贡献的个人和集体，均已在文中以明确方式标明。本人完全知晓本声明的法律后果由本人承担。

学位论文作者签名：
日期：　　年　　月　　日

上海交通大学
学位论文使用授权书

本人同意学校保留并向国家有关部门或机构送交论文的复印件和电子版，允许论文被查阅和借阅。

本学位论文属于：

□ 公开论文
□ 内部论文，保密 □ 1 年 / □ 2 年 / □ 3 年，过保密期后适用本授权书。
□ 秘密论文，保密 ___ 年（不超过 10 年），过保密期后适用本授权书。
□ 机密论文，保密 ___ 年（不超过 20 年），过保密期后适用本授权书。
（请在以上方框内选择打“√”）

学位论文作者签名：　　　　指导教师签名：
日期：　　年　　月　　日　日期：　　年　　月　　日

摘 要

粒子物理学的标准模型是描述物质世界微观构成及其相互作用规律的成功且系统的理论，为理解宇宙中的基本力和粒子提供了全面的框架。它描述了电磁、弱和强相互作用力的传播子（矢量玻色子），物质构成的基本粒子（夸克和轻子），揭示基本粒子质量起源机制的希格斯玻色子，及其之间的相互作用规律。尽管标准模型在解释许多粒子物理学方面取得了巨大的成功，但它也有其局限性。例如，暗物质和中微子质量等现象在标准模型中仍然无法解释。这些局限性激发了对标准模型之外新物理（BSM）的探索。

量子色动力学（QCD）是标准模型的关键组成部分，是描述强相互作用的理论。这种相互作用将夸克和胶子（构成质子、中子和其他强子的基本成分）结合在一起。在大型强子对撞机等高能碰撞中，根据 QCD 理论，夸克和胶子被散射后会强子化，形成喷注，从而能被探测器记录下来。

准确区分夸克喷注和胶子喷注对于理解粒子物理学中的许多过程至关重要。然而，由于强子化的原因，区分起源于夸克的喷注和起源于胶子的喷注是一个重大的挑战。本博士论文中呈现的物理分析旨在利用大型强子对撞机 LHC 实验上的 ATLAS 探测器在 Run2 实验阶段收集到的完整数据（2015 2018 年间，13TeV 质心能量下的质子-质子对撞数据），对标准模型之外的双喷注不变质量分布中的新共振态进行搜索。许多 BSM 新物理模型预测粒子可能衰变成一对胶子（例如卡鲁扎-克莱因引力子），本分析旨在寻找衰变成两个喷注的 BSM 共振态的证据，并采用了一种基于与喷注相关的带电轨迹分析的专门胶子标记方法，以提高探测新共振态的能力。

本分析中区分夸克和胶子喷注的过程（通常称为夸克/胶子标记）具有重要意义。本文研究了两种夸克/胶子喷注标记器的性能和校准：一种基于与喷注相关的带电轨迹数量（N_{trk}）的标记器，另一种则采用增强决策树（BDT）算法来结合各种喷注次级结构观测量。在 500 至 1200 GeV 喷注横向动量范围内，BDT 标记器在区分夸克喷注和胶子喷注方面的表现优于 N_{trk} 标记器。在高于此能级范围上，两种标记器的表现相当。同时对于 500 GeV 至 2 TeV 的喷注横向动量范围内，提供了数据与蒙特卡洛模拟之间夸克喷注标记效率的差异。在不同标记器工作点，其差异范围在 0.92 至 1.02 之间，包括大约 20% 的系统误差。该误差主要受到理论建模的影响。在数据上运用矩阵方法，从两个富含夸克/胶子地子样本中提取真实的夸克/胶子喷注比例，该样本由喷注的赝快度定义。

在分析中，通过参数化双喷注不变质量谱，估算了 QCD 本底。定义了三种

不同的谱：未标记的双喷注不变质量、一个胶子标记（1-*g* 标记）和两个胶子标记（2-*g* 标记）的信号道，用于搜寻 BSM 模型的引力子和量子黑洞（QBH）。由于没有观察到与本底明显的偏差，因此在三个类别中为 BSM 信号模型设置了 95% 置信水平（CL）的截面上限。引力子质量的观测下限为 3.81 TeV（未标记）、4.01 TeV（1-*g* 标记）和 4.26 TeV（2-*g* 标记）。对于 QBH 模型，质量的观测下限为 9.88 TeV（未标记）、9.89 TeV（1-*g* 标记），以及高于 10.00 TeV（2-*g* 标记）的 95% CL。尤其在高横向动量下，胶子标记后的搜索敏感性增强了 5%，为所考虑的 BSM 信号提高了搜索限制。在未来的研究中，该标记器有极大潜能提高标准模型的测量精细度，以及寻找超标准模型的灵敏度。

关键词：超越标准模型的新物理，大型强子对撞机 ATLAS 实验，强子喷注标定技术，新物理共振态寻找

ABSTRACT

The Standard Model (SM) of particle physics is a successful theory that provides a comprehensive framework for understanding the fundamental forces and particles in the universe. It describes the electromagnetic, weak, and strong nuclear interactions, and includes a range of elementary particles like quarks, leptons, and the Higgs boson. Despite its huge success in explaining many aspects of particle physics, the SM has its limitations. There are various phenomena, such as dark matter and neutrino masses, that remain unexplained within the SM. These limitations motivates a quest for new physics beyond the Standard Model (BSM).

Quantum Chromodynamics (QCD) is a pivotal component of the SM, representing the theory that describes the strong interaction. This interaction is responsible for binding quarks and gluons, the basic constituents of protons, neutrons, and other hadrons. In high-energy collisions, such as those in the Large Hadron Collider (LHC), QCD dynamics play a critical role. When quarks and gluons are scattered by collisions, they hadronised as jet and recorded by the detector.

Quark and gluon jets are central to understanding many processes within particle physics. However, distinguishing between a jet originating from a quark and one from a gluon presents a significant challenge due to the hadronisation. The physics analyses presented in this PhD dissertation search for new BSM physics in the dijet mass distribution using an integrated luminosity of 140 fb^{-1} of proton-proton collisions with a centre-of-mass energy at 13 TeV recorded by the ATLAS detector from the LHC. Many BSM models of new physics predict the particles could decay into a pair of gluons, this analysis aims at searching for the evidence of the BSM resonances that decay into two jets, with a specialized gluon-tagging approach adopted. This method hinges on the analysis of the charged tracks associated with a jet, to enhance the ability to detect new resonances .

The process of distinguishing jets arising from quarks and gluons, commonly known as quark/gluon tagging, is pivotal in this analysis. Thus the performance and the calibration of two quark/gluon jet taggers is studied: one tagger based on the number of charged tracks associated with the jets (N_{trk}), while the other employs a boosted decision tree (BDT) to combine various jet substructure observables. The BDT-tagger outperformed the N_{trk}-tagger in distinguishing quark-jets from gluon-jets up to 1200 GeV p_{T}, with both taggers showing comparable performance above this range. Differences between data and Monte Carlo simulation of quark-jet tagging efficiency are provided for jet transverse momenta ranging from 500 GeV to 2 TeV, encompassing various tagger working points, range between 0.92 and 1.02. These come with a combined systematic uncertainty of about 20%, predominantly caused by theoretical modelling uncertainty. A matrix method is performed on data to retrieve the quark/gluon fraction from quark/gluon-enriched subsamples, defined by the pseudorapidity of the jet.

In the analysis, the QCD background is estimated by the statistical framework which parametrised the dijet mass spectrum. Three different spectra are defined: the untagged dijet invariant mass, one gluon-tagged (1-g tagged) and two gluon-tagged (2-g tagged) channels for BSM signal Graviton and Quantum Black Hole (QBH) models. Because no significant deviation is observed, an upper limits for the cross-section then are set at the 95% confidence level (CL) for the three categories on signal models of BSM physics. The observed lower limits for Graviton mass were 3.81 TeV (untagged), 4.01 TeV (1-g tagged), and 4.26 TeV (2-g tagged). For the QBH model, the limits were 9.88 TeV (untagged), 9.89 TeV (1-g tagged), and above 10.00 TeV (2-g tagged) at 95% CL. Gluon tagging, enhanced by 5% per tagged gluon, especially at high p_{T}. By incorporating gluon-tagging on event selections, the search limits are improved for BSM signals considered.

KEY WORDS: New physics beyond the Standard Model, LHC, ATLAS, jet tagging, Search for new resonance

Contents

1 Introduction

Over the past seventy years, thousands of physicists have developed a notable insight into the fundamental structure of matters, known as fundamental particles, and the interactions they undergo through four fundamental forces. One of the best understandings of how these particles and three of the forces interact with each other is encapsulated in the Standard Model (SM) [1, 2] of particle physics. Developed in the early 1970s, it has been successfully proved by almost all experimental results. The huge success of the discovery of Higgs Boson in 2012 predicted by the SM was awarded the Nobel Prize in Physics in 2013. The SM has become established as a well-tested physics theory.

Although the SM accurately describes the phenomena within its domain, there are still theoretical flaws that prevent some fundamental physical phenomena from being fully explained by the SM. First of all, the model contains many parameters that cannot be derived from calculations alone but must be determined by experiment. In 1998, the Japanese Super-Kamiokande neutrino detector published results on neutrino oscillations that suggested the neutrinos have a non-zero rest mass, This groundbreaking finding, which deviates from the predictions of the SM, has profound implications for our understanding of the universe. It suggests that the SM, as it currently stands, might be an incomplete description of the fundamental constituents and forces of nature. Furthermore, two of the most intriguing and elusive concepts in modern physics - gravity and dark matter - remain absent from the SM. Gravity, one of the fundamental forces, is not accounted for in the SM, a limitation that has led physicists to explore BSM theories. The presence of dark matter, inferred from astrophysical observations, indicating the necessity for new physics to explain these unaccounted-for aspects of the universe.

Many models of physics beyond the Standard Model (BSM) [3] predict the presence of new particles that couple to quarks and/or gluons. Such particles could be produced in proton-proton collisions at the Large Hadron Collider (LHC) [4] and then decay into quarks and gluons, during this process two hadronic jets are created, which then can be seen by the detector. The new energy regime ($\sqrt{s} = 13$ TeV) with an integrated luminosity of 140 fb^{-1} provided by the LHC opens a window to search for BSM particles.

This thesis explores potential BSM physics by examining the two-jet (dijet) invariant mass (m_{jj}) distribution, detecting BSM resonances that result in dijet decay. Given that some new resonances might decay predominantly into gluons, a gluon-tagging technique, which considers associated charged tracks within a jet, has been utilized, classified the search regions into untagged, 1-gluon(g) tagged and 2-g tagged regions. A critical aspect of this work is the quark/gluon tagging, a process that differentiates jets initiated by quarks from those by gluons. This research evaluates the effectiveness of two quark/gluon tagging methods: one assessing the number of charged tracks linked with jets and the other using a boosted decision tree that integrates multiple jet substructure variables. Discrepancies between actual data and Monte Carlo (MC) simulation for tagger efficiency are documented for jet transverse momenta between 500 GeV and 2 TeV across diverse tagger working points. Employing a matrix method on the collected data, the quark/gluon composition is extracted from subsamples enriched in quark or gluon content, determined by jet pseudorapidity.

In the SM, these dijet events are generated mainly by quantum chromodynamic (QCD) processes and appeared to be a smoothly decreasing m_{jj} distribution, however, a new particle that decays into quarks or gluons could appear as a resonance in the m_{jj} spectrum. If the resonant samples can be classified based on the type of parton that initiated the jets, the sensitivity of the search for such resonances could be largely increased. Hence, classifying jets as initiated from a quark or a gluon can be effective for improving SM measurements and searches for BSM physics.

Recent developments [5, 6, 7, 8, 9, 10, 11, 12, 13, 14, 15, 16, 17, 18, 19, 20, 21] in quark/gluon (q/g) tagging have resulted from advances in the theoretical [22], phenomenological [23, 24, 25, 26] and experimental understanding of q/g tagging as well as the development of powerful machine learning techniques that can utilize the entire jet internal radiation pattern. The calibration of q/g taggers is performed to account for the systematics of searching results.

This thesis is structured as follows. Chapter 2. describes the theoretical framework of the SM, its limitations and various potential extensions beyond it. An introduction to the LHC and the ATLAS detector is given in Chapter 3. Jet reconstructions and calibrations are briefly described in Chapter 4. The quark/gluon tagger definitions and the selection criteria used to generate the various event samples employed in the discriminant extraction, the method and the scale factor results are presented in Chapter 5. The details of the search for new resonances in the dijet spectrum and the limit setting results are shown in Chapter 6. In the end, the conclusion and outlook of the research are presented in Chapter 7.

2 The theory framework

2.1 The Standard Model

The SM of particle physics, which describes the three fundamental interactions - strong, weak and electromagnetic interactions, alongside the elemental constituents that constitute all forms of matter,emerges as an unparalleled triumph in the scientific quest to decode the universe's most fundamental aspects. The SM divides particles into two categories, fermions and bosons, based on the values of their spin: fermions are the particles that makeup matter, such as electrons in leptons, quarks and neutrinos, which have half-integer spin; bosons are the particles that transmit forces, such as photons and mesons that transmit electromagnetic forces, gluons that transmit strong nuclear forces, W and Z that transmit weak nuclear forces, have integer spin. Different properties shown in fermions and bosons are due to the difference in spin. According to the spin-statistics theorem, fermions obey the Pauli exclusion principle, whereas bosons do not, thus bosons do not have a theoretical limit on their spatial density. All particles and forces with their masses, charges and spines are summarised in Figure 2.1.

The SM serves as an exemplar of a quantum field theory, offering the mathematical underpinning for such a framework. The Lagrangian controlled the dynamics and kinematics of the system satisfies the $SU(3)$ x $SU(2)_L$ x $U(1)_Y$ gauge symmetry, in which $U(1)_Y$ corresponds to a particle B with weak hypercharge Y. $SU(2)_L$ corresponds to particles W_α (α = 1, 2, 3) with weak isospin T and only left-handed chiral particles. The electroweak force which unifies the electromagnetism and the weak interaction as a Yang-Mills field is represented by the group $SU(2)_L$ x $U(1)_Y$, mathematically. In SM, the Z^0 boson and the photon (γ) are given by:

$$\begin{pmatrix} \gamma \\ Z^0 \end{pmatrix} = \begin{pmatrix} \cos\theta_\mathrm{W} & \sin\theta_\mathrm{W} \\ -\sin\theta_\mathrm{W} & \cos\theta_\mathrm{W} \end{pmatrix} \begin{pmatrix} B \\ W_3 \end{pmatrix} \tag{2.1}$$

where θ_W is the weak mixing angle.

The charged massive bosons $W^\pm$ are given by W_1 and W_2:

$$W^\pm = \frac{1}{\sqrt{2}}(W_1 \mp iW_2) \tag{2.2}$$

$SU(3)$ corresponds to eight vector fields $A^\alpha(\alpha = 1, 2, ...,8)$ representing gluon fields,

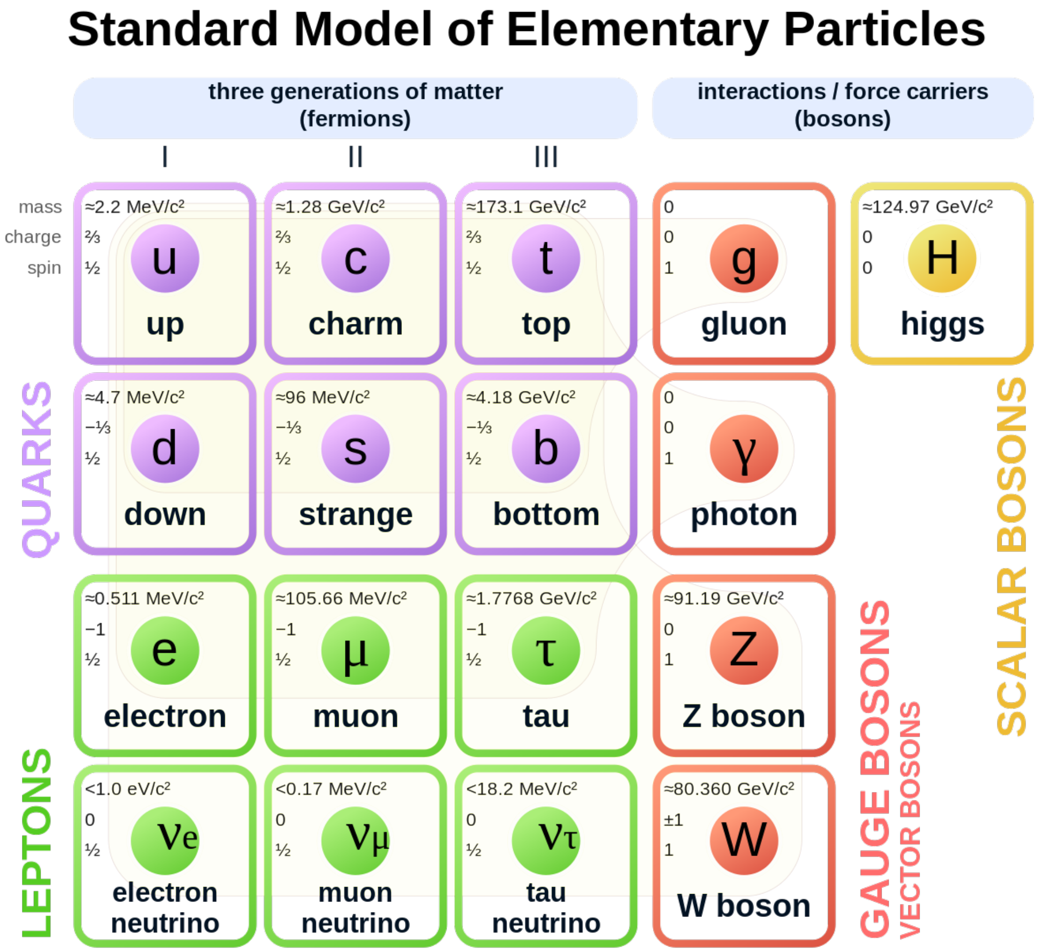

Figure 2.1 The Standard Model of particle physics [27]

which are vector gauge bosons that carry the colour charge of the strong interaction and mediate between quarks in QCD. The Higgs boson, unlike all other known bosons such as the photon, is a scalar boson and has a non-zero average value in vacuum. It is resulted from the process of spontaneous symmetry breaking. The Higgs mechanism explains the generation of the property "mass" for gauge bosons. At a critical temperature, the Higgs field introduces a vacuum expectation value that causes spontaneous symmetry breaking during interactions, leads the bosons it interacts with acquire masses. A Yukawa coupling is used in the SM to describe the interaction between the Higgs field and fundamental fermions, explain the generation of the masses of fermions.

This chapter therefore focuses on the present SM, various extensions and variants of the SM that have been proposed by theoretical physicists are explored in Section.2.2.

2.1.1 Quantum chromodynamics

QCD is the theory of the strong interaction between quarks and gluons, and it is a fundamental component of the SM of particle physics. Satisfying the $SU(3)$ symmetry group invariant, QCD is a non-abelian gauge theory. Over the years, QCD has collected a huge body of experimental evidence, proved that it has been a successful application from a quantum field theory.

The Lagrangian of QCD can be expressed as:

$$\mathscr{L}_{\mathrm{QCD}} = \bar{\psi}_i \left(i\gamma^{\mu} \left(D_{\mu}\right)_{ij} - m\delta_{ij} \right) \psi_j - \frac{1}{4} G^{a}_{\mu\nu} G^{\mu\nu}_{a} \tag{2.3}$$

where ψ_i is the quark field in the fundamental representation of the $SU(3)$ gauge group, indexed by i and j running from 1 to 3; m corresponds to the quark mass; the γ^{μ} are Dirac matrices relating the spinor representation to the vector representation of the Lorentz group.

D_{μ} is defined as the gauge covariant derivative:

$$\left(D_{\mu}\right)_{ij} = \partial_{\mu}\delta_{ij} - ig_s \left(T_a\right)_{ij} \mathscr{A}^{a}_{\mu} \tag{2.4}$$

which couples the quark field with a coupling strength g_s to the gluon fields via the infinitesimal $SU(3)$ generators T_a. By including the Gell-Mann matrices λ_a (a=1...8), an explicit representation of T_a is defined by T_a=λ_a/2.

The gauge invariant gluon field strength tensor $G^{a}_{\mu\nu}$ is given by:

$$G^{a}_{\mu\nu} = \partial_{\mu}\mathscr{A}^{a}_{\nu} - \partial_{\nu}\mathscr{A}^{a}_{\mu} + g_s f^{abc} \mathscr{A}^{b}_{\mu} \mathscr{A}^{c}_{\nu} \tag{2.5}$$

where $\mathscr{A}^{\alpha}_{\mu}$ are the gluon fields, indexed by a, b and c running from 1 to 8; f^{abc} are the structure constants of $SU(3)$. The coupling strength g_s can be referred to strong coupling constant α_s:

$$\alpha_s = \frac{g_s^2}{4\pi} \tag{2.6}$$

There are some salient properties that QCD exhibits:

Colour confinement

This is a consequence of the force between two colour-charged particles that can not be isolated in a condition that below the Hagedorn temperature of approximately 2 terakelvin. To separate two quarks in a hadron, extremely high energy is required, leading to the creation of a quark-antiquark pair that formed a pair of hadrons rather than a single hadron. In addition, glueballs which are formed only of gluons are colourless and also consistent with confinement, causing difficulty in identification in experiments.

Asymptotic freedom and the running coupling

This is a feature of QCD that demonstrates the strong interactions between quarks and gluons become asymptotically weaker as the energy scale of them increases and the corresponding length scale decreases. This is opposite to the behaviour of colour-charged particles at low energies where the confinement of quarks and gluons exhibits. At high energy, the coupling decreases logarithmically as a function of momentum transfer Q:

$$\alpha_{\mathrm{s}}\left(Q^2\right) \overset{\mathrm{def}}{=} \frac{g_{\mathrm{s}}^2\left(Q^2\right)}{4\pi} \approx \frac{1}{\beta_0 \ln\left(Q^2/\Lambda^2\right)} \tag{2.7}$$

where β_0 is a one-loop beta function in QCD and has the dependence of the coupling parameter g_{s}. The quantity Λ is referred to QCD scale that is measured in processes where the strong coupling constant and other measurable vary with momentum transfer Q. However, this is only effective at leading order (LO). By including higher order terms, the calculation expanded in order of α_s resulted in more complexity and less significance as the scale of Q increases. On the other hand, as Q tends to be infinite large, the coupling strength becomes zero thus the behaviours of quarks are asymptotically free. These variation of coupling α_s under the different scales of energy in QCD is described as the running coupling.

The calculation of matrix element in QCD can be rather complex as more and more perturbative contributions are considered, which requires the application of complicated integrals over a large number of variables. A Feynman diagram is used as a representation of the expressions of these integrals pictorially and an improvement of undertaking the critical calculations.

With more interactions points involved in, more complicated the calculations become. The effects of self-interactions between particles themselves can happen by producing a virtual particle which is restricted by the uncertainty principle, represented as a

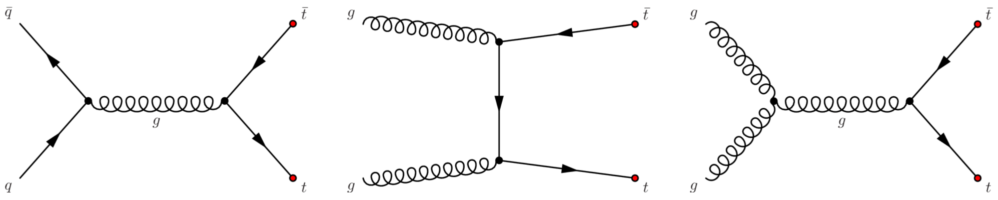

(a) (b) (c)

Figure 2.2 Feynman diagrams of strong interaction in top-antitop quarks production via (a) one gluon exchange in quark-antiquark annihilation, gluon-gluon fusion in (b) t-channel and (c) s-channel.

loop in a Feynman diagram. The accuracy of the calculation has dependency on the coupling α_s and is contributed to a fraction at each order. By including an infinite number of virtual particles, the calculations are led to divergent and infinite.

A set of techniques named renormalization are employed in solving the infinities showed up in the calculations, by which the infinite self-interactions are parametrised by re-scaling them as finite values to compensate the effects. The ultraviolet (UV) divergence arises when considering the contributions from extremely high-energy interactions, leading to integrals that tend to infinity. To manage this, the concept of the renormalization scale (μ_R) is employed. The renormalization scale acts as a threshold, beyond which the effects of these high-energy contributions are 'normalized' or adjusted, ensuring that the calculations remain physically meaningful and finite. In contrast, the factorization scale (μ_F) addresses a different aspect of divergence in QCD. This scale is concerned with the behaviour of interactions at very low, or infinitesimal, energies. As the energy approaches zero, integrals can again diverge, posing a problem for accurate computations. The factorization scale is thus introduced to regulate these low-energy contributions, separating the long-distance (or low-energy) effects from the short-distance (or high-energy) ones. This allows for a more controlled and precise approach in calculating the dynamics of quarks and gluons in various energy regimes.

However, it is imperative to emphasize that not all QCD phenomena are amenable to perturbative treatment. The transition to low-energy regimes results in a substantial increase in α_s, heralding the dominance of non-perturbative effects. These effects are essential for understanding phenomena such as quark confinement and chiral symmetry breaking, with the former ensuring that quarks and gluons are perpetually bound within hadrons, and the latter influencing the masses of light quarks through spontaneous symmetry breaking. Such non-perturbative facet of QCD affects the modelling dependence in the analysis later on. A meticulous consideration of these non-perturbative aspects is studied in the Chapter 5, ensuring that our models are both accurate and reliable.

2.2 Physics beyond the Standard Model

2.2.1 Kaluza-Klein Graviton

In particle physics, Kaluza–Klein theory (KK theory) [28] is a significant concept that served as a classical unified field theory, attempts to unify gravitation and electromagnetism by proposing the existence of a fifth dimension, beyond the conventional four spacetime dimensions. An intriguing aspect of this model is the KK gravitons, while gravitons are hypothetical elementary particles that mediate the force of gravity in quantum field theories, the KK gravitons are a set of massive excitations of the graviton in these extra spatial dimensions, exhibit enhanced coupling with the SM, surpassing the expected Planck scale limitations, makes their production and subsequent decay at colliders of interest.

Within this theoretical framework, the Randall-Sundrum (RS1) [29] model stands out due to its distinctive incorporation of an extra dimension. It posits a five-dimensional anti-de Sitter spacetime, where our observable universe is represented by a four-dimensional boundary or brane. Crucially, RS1 features an extra, compactified spatial dimension between two such branes. The gravitational interactions become weaker as one moves away from the TeV brane, offering a solution to the hierarchy problem. This warping of spacetime results in the graviton having a spectrum of massive KK modes, influencing its interactions in our observable universe.

While still theoretical, searching for these KK gravitons, especially at high-energy physics experiments like those at the LHC, offers an unique perspective on the effects of extra dimensions and thereby deepen our understanding of the universe's fundamental nature. Due to their enhanced couplings with the SM, the KK gravitons can decay into any pair of SM particles, with the decay rates being largely determined by the masses of these particles. Among these, the gluon-gluon channel often dominates because of the large colour charge of gluons and the large number of available gluon states.

The graviton sector within the RS1 model is fully determined by two key parameters: m_{KK} and $k/\overline{M}_{Pl}$, where m_{KK} is the mass of KK graviton, k is a scale of order the Planck scale, M_{Pl} is effective four-dimensional (reduced) Planck scale.

2.2.2 Quantum Black Hole

Quantum Black Hole (QBH), also called micro black holes, is regarded as hypothetical mini (less than a solar mass unit) black hole that dominated by quantum mechanical effects at sizes close to the Planck length [30]. Some hypotheses predict that QBH could be produced at energies as low as the TeV range, which can be generated in particle accelerators such as the LHC, and can be observed through the particles that are emitted by the process of Hawking radiation [31]. Theoretical calculations indicate that as black holes decrease in size, their rate of evaporation accelerates. This phenomenon leads to an abrupt release of particles, akin to a sudden eruption, when a micro black hole approaches its final stages of evaporation.

In the simplest scenario, the decay of QBH via Hawking radiation can be approximately described as isotropic decay to a many-particle final state. The threshold of quantum-gravity energy scale $M_D \equiv \left[M_{Pl}^2/(8\pi r_c^n)\right](1/(2+n))$ is set to be well below the the actual thermal black hole production threshold for gravitational interactions so that two-body states in final states are the dominant, a resonance-like result is expected in predominantly two-body final states as jets closed to M_D. Such isotropic final states is aimed as probes of quantum gravitational effects in this dijet analysis.

3 The ATLAS Experiment

3.1 The Large Hadron Collider

The LHC, built by European Organization for Nuclear Research (CERN) located in Geneva, Switzerland, is the largest circular particle accelerator in the world. The goal of it is to probe the various theoretical predictions made by physicists.

It consists superconducting magnets that construct a 27-kilometer ring lying in the tunnel under the ground. Inside the LHC, two beams made of protons or ions are accelerated to extreme high speed in opposite direction in individual vacuum pipes then made into collision by a strong magnetic field within the structures.

The LHC is the last section of the CERN accelerator complex where a series of machines accelerates the particles to increasingly higher and higher energies. The highest energies of beams are reached at the LHC.

Seven detectors are placed around four collision points in the collider. Different types of particles are accelerated according to the research, the main beams are protons, but the LHC also run beams of heavy ions as lead–lead collision or proton-lead collisions.

The energy of particles is increased by a series of processes before being injected into the main accelerator. For a proton-proton collision, negative hydrogen ions are generated by the linear particle accelerator Linac4 at 160 MeV then injected into the Proton Synchrotron Booster, where protons are obtained by stripping electrons away from the atom and accelerated to 2 GeV. After entered the Proton Synchrotron the energy of the protons is 26 GeV, and then their energies are increased in Super Proton Synchrotron to 450 GeV before they are finally injected into the main ring.

One of the characteristics that defines the power of an accelerator is the centre-of-mass energy, which represents the total momentum of the system and thus indicates the total mass of potential new particles as well as probes the internal structure of known particles under the law of energy invariant within the system. In 2010, the first collisions were made at an energy of 3.5 TeV each beam, later in 2018, an energy of 6.5 TeV per beam was achieved, resulted in the centre-of-mass energy of 13 TeV where the protons moved at more than 99.9% speed of light. It took less than 90 μs for photons to go through the whole LHC ring.

Other quantities such as luminosity, denoted as $\mathscr{L}$, also represents the performance

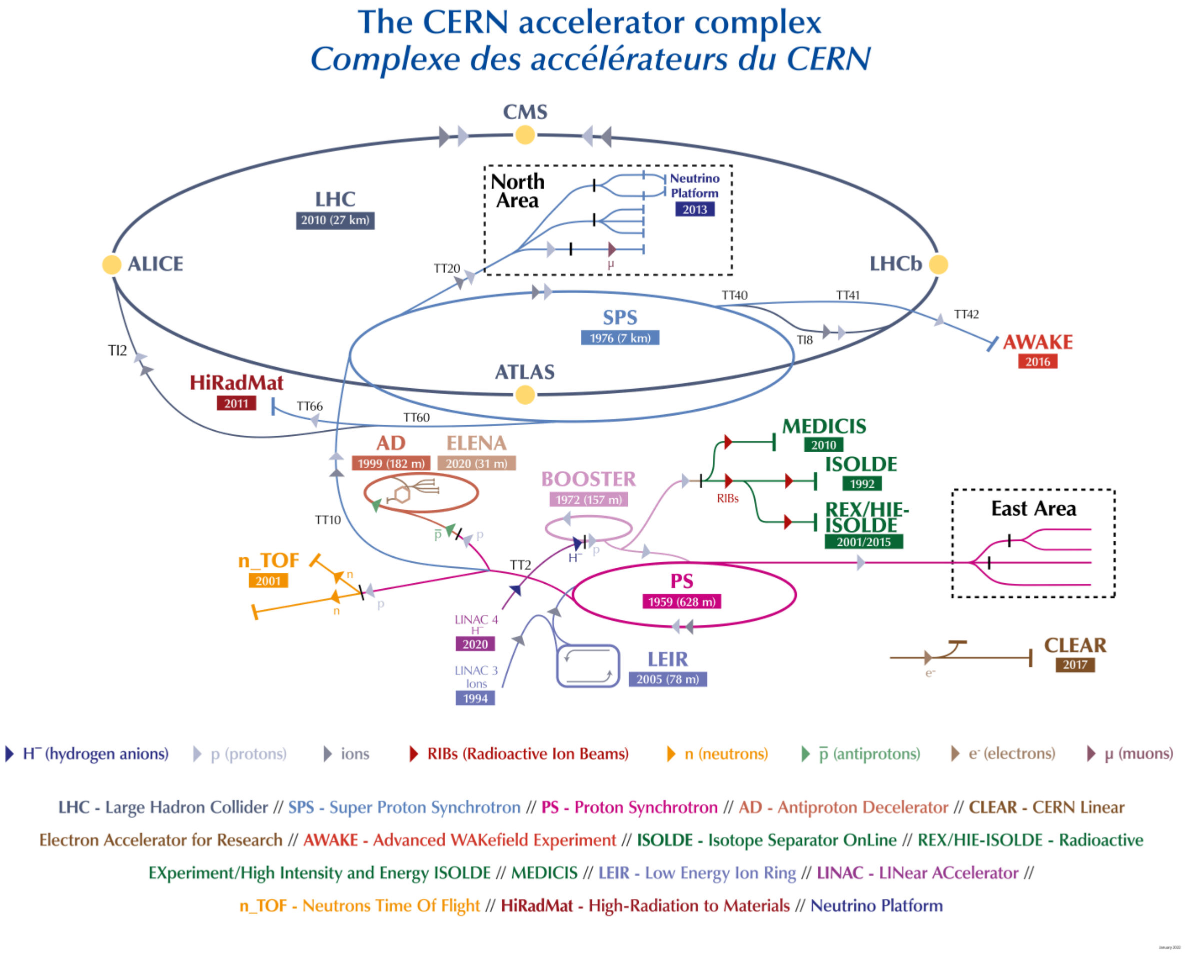

Figure 3.3 The CERN accelerator complex

of an accelerator. It is the rate of interactions during a certain period of time and can be expressed as:

$$\mathscr{L} = \frac{N^2 f_{rev}}{4\pi\sigma_x\sigma_y} \tag{3.1}$$

where N is the number of particles in a bunch, in the case that a beam has Gaussian distribution and has brunches crossing frecuency f_{rev}. σ_x and σ_y denote as transverse beam widths in the x- and y-plane. The luminosity takes the units of $\mathrm{cm}^{-2} \cdot \mathrm{s}^{-1}$.

The total number of physics events detected can be express as:

$$N_{\text{event}} = \sigma_{\text{event}} \cdot \int \mathscr{L} dt \equiv \sigma_{\text{event}} \cdot L \tag{3.2}$$

where L is the integrated luminosity with respect to time, σ_{event} is referred to the cross section of a specific physics process. The integrated luminosity takes the units of cm^{-2} which equals to the unit femtobarn (fb).

At the LHC, thousands of magnets around the accelerator are operated at a very low temperature of -271.3°C to maintain its superconducting state which allow them to conduct electricity without loss of energy. Hence, a system of liquid helium is used for cooling the accelerator and supply services.

Besides, superconducting radio frequency cavities which resonate electromagnetic fields are employed to accelerate the protons. Instead of having continuous beams, the protons are made into bunches, so that the collisions are taken place at discrete intervals between two beams with 115 billion protons per bunch at the frequency of 25 ns.

3.2 The ATLAS detector

The ATLAS detector [32] is the largest volume detector ever constructed for general-purpose particle research at the LHC. It has the shape of a cylinder with 44 meters long, 7000 tonnes in weight and 25 meters in diameter, sitting in a cavern underground. It is designed to collect evidence of the properties of SM and search for new predictions made by particle physics beyond the SM.

To record the energy, momentum and trajectory of particles after collisions, the detector consisting of 6 different detecting subsystems placed in layers surrounding the interaction point to measure them individually and effectively.

An overall layout of the ATLAS detector is shown in Figure 3.4.

3.2.1 Inner detector

Charged particles above a certain p_{T} threshold are detected by the ATLAS Inner Detector (ID) which immersed in a 2 T solenoidal field, covered the pseudorapidity range $|\eta| < 2.5$. Appearing as tracks in the ID, an excellent momentum resolution as well as both primary and secondary vertex of them are provided by the ID. Within the range $|\eta| < 2.0$, electron identification is also provided.

The layout of the ID is shown in Figure 3.5 in cylindrical coordinate: $r = \sqrt{x^2 + y^2}$, where x-axis alongside the LHC ring and y-axis is perpendicular to the x-axis.

A cylindrical container around the ID has a length of 3512 mm each way and a radius of 1150 mm, tracks of 10 GeV traverse the sensors and structural elements in the

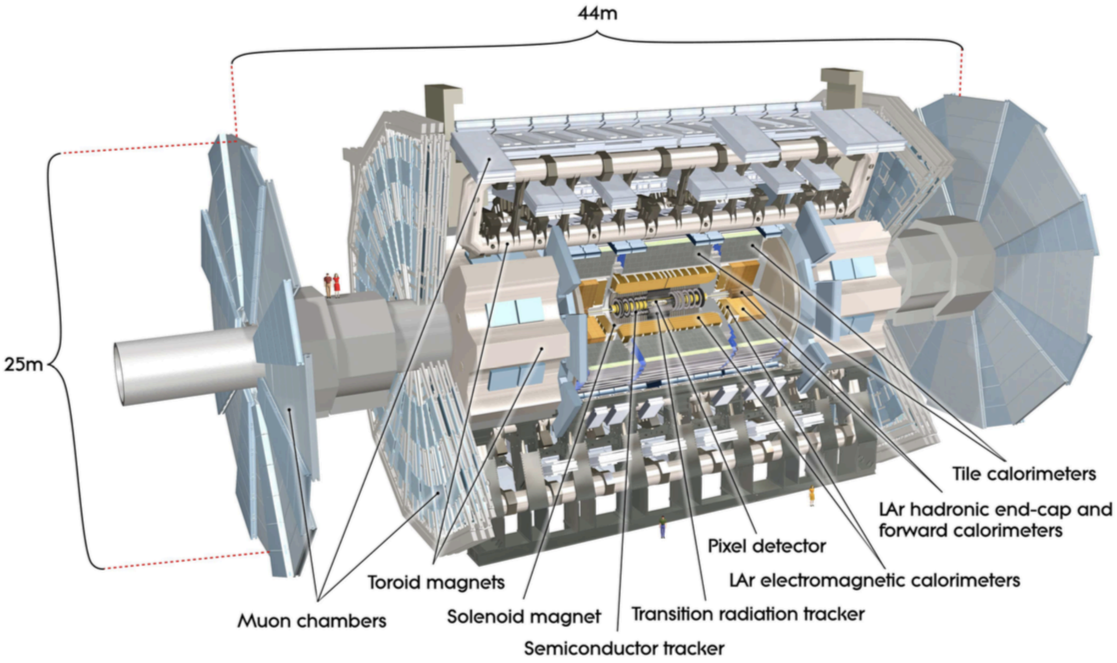

Figure 3.4 Cut-away view of the ATLAS detector

barrel and end-cap regions, respectively.

Within the inner region, a series of discrete space points provided by the silicon pixel detector and stereo pairs of silicon microstrip semiconductor tracking (SCT) layers gives high-resolution pattern recognition abilities. By increasing radial distances, the transition radiation tracker (TRT) provides extra pattern recognition and momentum resolution capabilities.

The pixel detector

A series of high-granularity measurements is provided by the pixel detector [33] which is composed of the innermost sub-detector of the ID, it is designed as close to the interaction point as possible. Three sub-sections: two end-cap perpendicular to the beam axis and a barrel alongside the beam axis as a concentric cylinder with four layers (average radii of 33.25, 50.5, 88.5 and 122.5 mm, respectively) in it.

The innermost pixel layer (or B-layer, IBL) is essential to b-tagging performance and supersymmetry searches as it cover the full acceptance of short-lived particles such as B hadrons and τ leptons from the beginning of Run-2 to enhance the measurement of the secondary vertex. Besides, a new readout sensor and chip responsible for higher radiation damage and higher hit rate, respectively, is em-

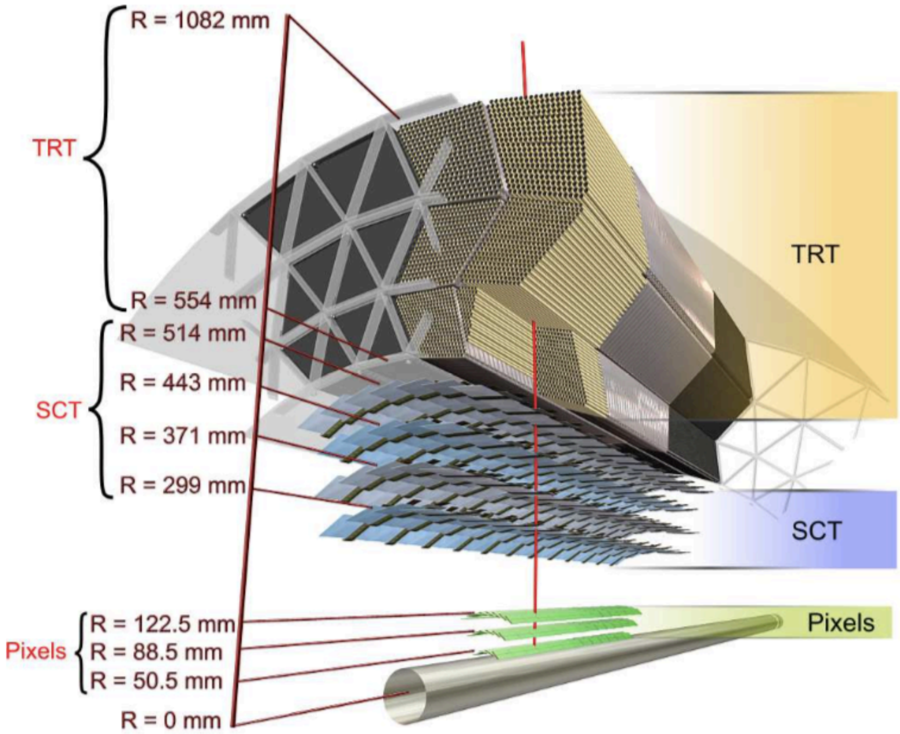

Figure 3.5 Cut-away view of the ATLAS ID. Sensors and structural elements traversed by a charged track of 10 GeV p_{T} in the barrel inner detector along with their envelopes in r.

ployed in the IBL compared to the other three layers in the barrel region. A new n-in-n planar and 3D silicon sensors with hit efficiency of greater than 97% is developed as well. The better impact parameter resolution is achieved by reducing the pixel size of the chip down to 50 × 250 μm^2. Around 80 million readout sections counting them all provide the great hit resolution of 10 μm in radius plane and 115 μm alongside the z-axis in the pixel detector.

The semiconductor tracker

Surrounding the pixel detector is the SCT which encompasses silicon based semiconductor sensing components in barrel and end-cap geometries. Four silicon microstrip layers, located at radii of 300, 373, 447 and 520 mm, in the barrel region of the SCT provide high granularity points. The mean size of each strip pitch is 80 μm for the rectangular barrel sensors as daisy-chained with 6 cm-long. For the end-cap sensors, nine disks cover $|\eta| < 2.5$ are chosen. As a results, there are thus 768 readout strips with 6.36 × 6.40 cm^2 in size in total, with additional two strips at the edge of the sensor. 6.1 m^2 of silicon detectors with 6.2 million readout channels as a whole integrated the SCT.

The transition radiation tracker

The outermost layer of the ID is the TRT which encompasses polyimide drift(straw) tubes that designed to enable as much less wall thickness and material as possible while maintaining the good experimental properties. With 4 mm in diameter and 150 cm in length, 73 layers of 144 cm alongside the beam with 50 thousands tubes and 37 cm tubes consisting 160 tubes planes in the end-cap with 320 thousands radial tubes.

The xenon-based gas filled up in a given tube provides the track hit of a particle as it ionized as the emitting electrons drifting to the center wire of the tube volume. An average of 36 hits per charged-particle track is given by the TRT, The resulting electrical signals are obtained by converting the drifting charge currents. In total 420 thousands of electronics channels in which a good spatial resolution and drift-time measurement are provided by the TRT, enhancing the precision measurements of momentum in the ID.

3.2.2 Calorimeters

Outside of the ID lies the ATLAS calorimeters system which is designed to obtain the energy lost of the particles that travel through the detector components. Multiple layers of high-density material are placed to consume the energy of the incoming particles inside the materials and stop them from further moving. An “active” medium is left inside the layers that allows experimental physicists measure the energy of those particles.

Two types of calorimeters are employed in the ATLAS calorimeters system: the energy of electrons and photons are measured by the electromagnetic calorimeters as they create reaction with matter. Hadronic showers that created by the interaction between hadrons and atomic nuclei, are sampled by the hadronic calorimeters. Muons and neutrinos can not be stopped by the calorimeters as they interact only weak force but the track footprints could be seem in the calorimeters. The layout of the calorimeters is shown in Figure 3.6.

The electromagnetic (EM) calorimeter covers a range of $|\eta| < 3.2$ by combining the one barrel and two end-cap modules as cylindrical cryostat, with an outer radius of

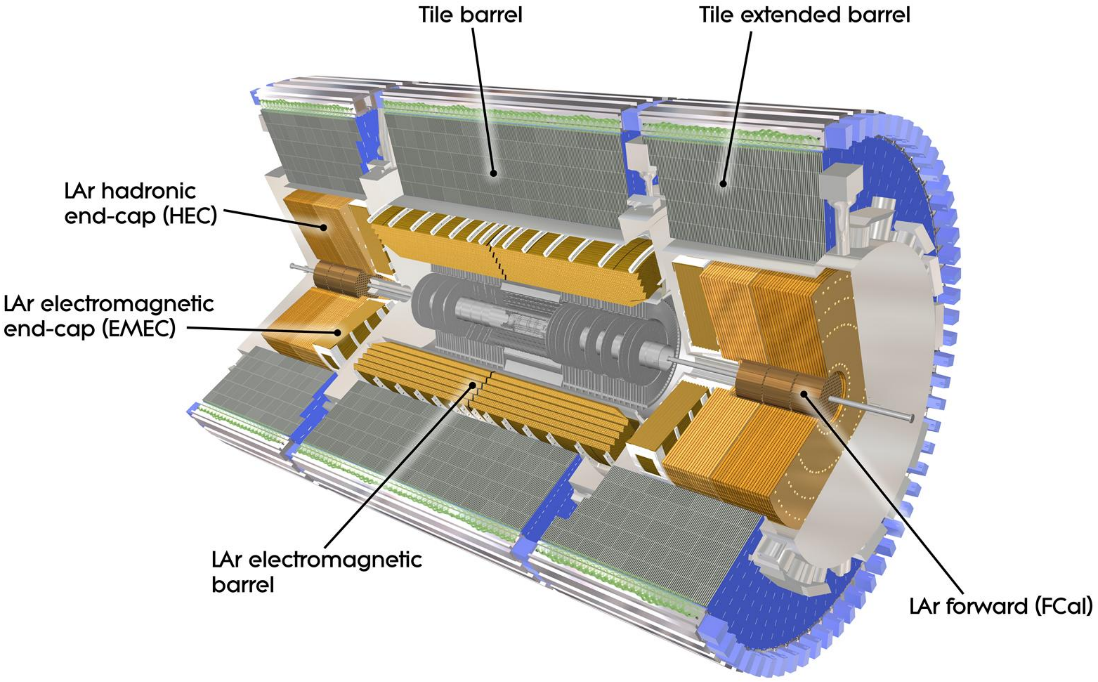

Figure 3.6 Outline of the ATLAS Run 2 trigger and data-acquisition system.

2.25 m, an end-cap thickness of 0.632 m and a length of 3.17 m. The hadronic calorimeter covers the central barrel region of $|\eta| < 1.0$ and two extended barrels in a region of $0.8 < |\eta| < 1.7$. with a radius of 2.28 m at the inside and 4.25 m at the outside. Figure 3.7 demonstrates the positions of the end-cap of the calorimeters including the EM and Hadronic calorimeters.

The electromagnetic calorimeter

The EM calorimeter that surrounding the ATLAS ID is designed for the high-granularity measurements of the energy of photons, electrons and hadrons with Liquid Argon (LAr) sandwiched between the multiple layers ionised. It converts the incoming particles into electric currents by absorbing the energy of these particles as they interact with the metal with the bremsstrahlung phenomenon. A pair of electron-positron produced by an electron radiation in the EM calorimeter can initiate further electron-positron pairs (as showers) until the energy of the particles fall below the certain threshold, the dominate process thus become ionisation in the LAr where drifting electrons are produced. Furthermore, the missing transverse energy can be obtained by subtracting the total energy of the known particles,

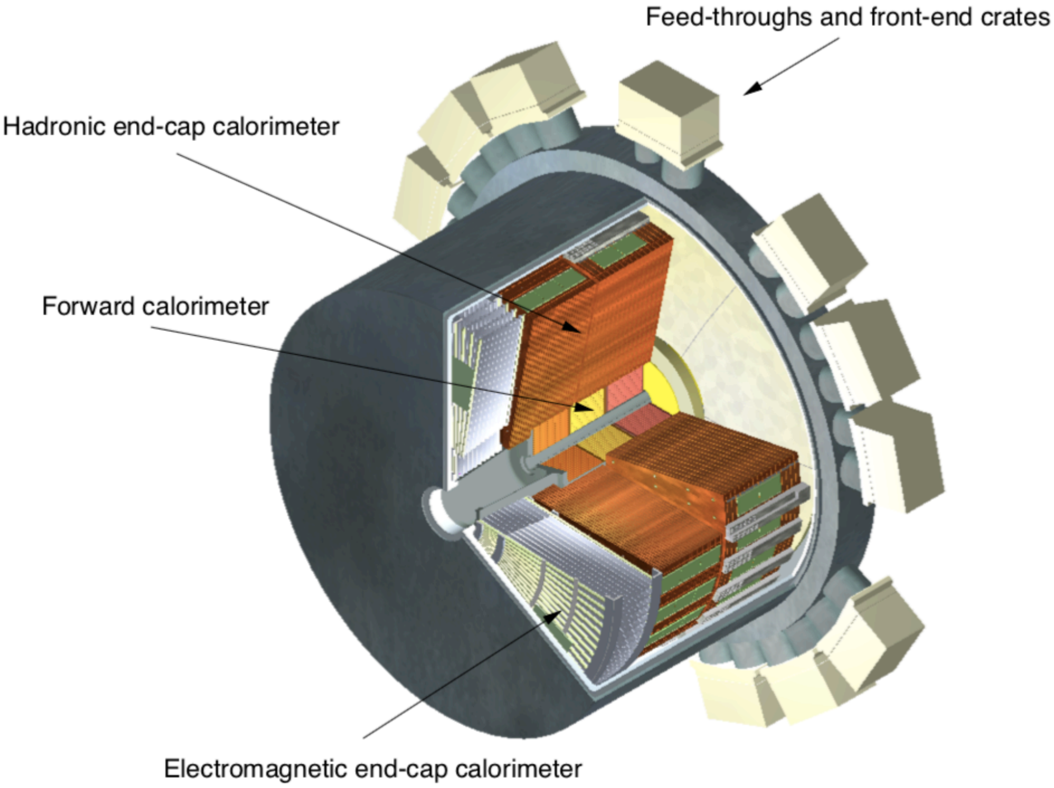

Figure 3.7 Cut-away view of an end-cap cryostat of the ATLAS calorimeter system.

which contributes to the analysis of neutrinos and new particles.

At -184 °C where the argon exists in liquid form, the calorimeter is kept as the cables that transverse electronic signals are sealed in vacuum and connected to the warmer area where located the readout system.

The hadronic calorimeter

Surrounded the EM calorimeter, lies the tile hadronic calorimeter where hadrons that contain strong force thus could not fully deposit their relatively large energy in the EM calorimeter are absorbed by the tile calorimeter. Steel and plastic scintillating tiles are placed in layers in order to record the trajectories of incoming particles as hadronic showers are formed by the interactions of the particles with the materials and emitting particles continue interacting with materials in the hadronic calorimeter and more particles are produced in steel layers. On the other hand, photons are produced by the plastic scintillators where electric currents are gained according to the energy of the particle.

By enveloping the EM calorimeter, a hadronic shower that contained EM showers can be fully absorbed by the great thickness in the hadronic calorimeter. Around 420 thousands of plastic scintillator tiles are placed in sync, leading a weight of 2.9 thousands tonne in total.

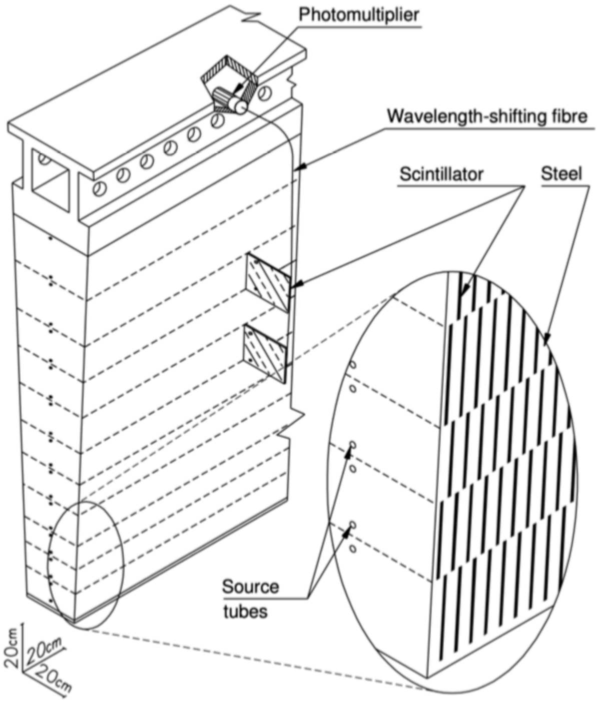

Figure 3.8 A schematic view of a tile calorimeter components of optical readout tiles and scintillating tiles.

As illustrated in Figure 3.8, photomultiplier tubes (PMT) are placed around the outer radii of the tile calorimeter and connected with wavelength-shifting fibres by which scintillation light is transferred. Projective geometry is designed for the whole readout system as the energy of most hadronic showers is deposited in the first or last two layers. Though the coarser granularity of the readout cells of hadronic calorimeter has been compared to the EM calorimeter, the hadronic calorimeter is qualified for the measurement of transverse momentum and jet reconstruction.

In the forward regions, the hadronic calorimeters are integrated with LAr calorimeters due to higher radiation exposition compared to the barrel regions. There are two calorimeters that were developed to tackle such issue: the hadronic end-cap calorimeter (HEC) that covers $1.5 < |\eta| < 3.2$ and the forward calorimeter (FCal) that covers $3.1 < |\eta| < 4.9$.

The HEC located further beside the EM end-cap calorimeter has two wheels in each end-cap. LAr is used for filling up 8.5 mm between copper layers in the HEC, by which the active medium is provided. The readout electrodes are provided in separate drift zones in order to secure the stability of the whole system. The FCal has three wheels placed alongside the z-direction: one electromagnetic layer (FCal 1) and two hadronic layers (FCal 2 and FCal 3). LAr is also used as an active medium in all of the layers. As for the absorber, copper is employed in FCal 1 as it has heat removal properties. Tungsten is used in both FCal 2 and FCal 3 in order to constrain the lateral spread of hadronic showers.

3.2.3 Muon spectrometer

The muon spectrometer (MS), specially designed for the muon detection is located in the outermost section of the ATLAS in order to provide sufficient measurement of high-momentum muons which are almost "invisible" to the ID and calorimeters due to little energy deposit when traveled through the them. By deflecting the trajectories of muons, the MS employs the magnetic field by a barrel toroid magnet system in $|\eta| < 1.4$ and end-cap toriod systems in $1.6 < |\eta| < 2.7$.

Four subsections of the MS: add up to 4000 separate muon chambers. Thin Gap Chambers (TGC) and Resistive Plate Chambers (RPC) account for triggering and the second coordinate measurement of muons. TGC is set at the end of the detector whereas RPC which provides 5,000 V/mm electric field is placed in the central region. Monitored Drift Tubes (MDT) is designed for the curve of muon tracks measurement with fine tube resolution of 80 μm. Cathode Strip Chambers (CSC) accounts for measuring coordinates precisely located at ends of detector with a fine resolution of 60 μm. Figure 3.9 demonstrates the MS with all four subsections. In total three separate points within the muon trajectory are measured to reconstruct the momentum of the muon.

3.2.4 Trigger and data acquisition

The ATLAS trigger and data acquisition system is a crucial component of the experiment, designed to manage the immense volume of data generated by the LHC. Given the context of approximately 1 billion proton-proton collisions occur per second and an

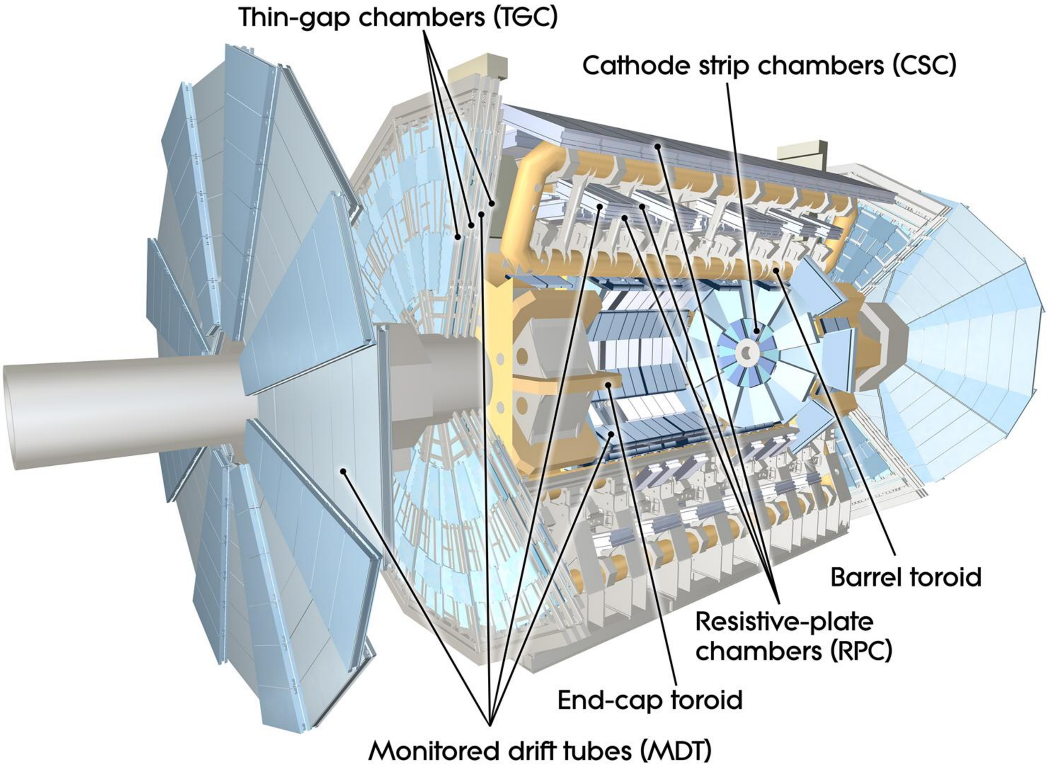

Figure 3.9 Cut-away view of the ATLAS Muons Spectrometer with subsections labeled.

integrated luminosity of 140 fb^{-1} , the role of this system becomes even more critical. However, many of these collisions are unlikely to produce characteristics of interest. As a result, large numbers of events can be discarded without affecting the search for new physics. The trigger and data acquisition systems are introduced to eliminate the irrelevant data so that only events of suitable quality and quantity are recorded.

During the year of 2015-2018, the trigger system in ATLAS selected significant events in a two staged process, as illustrated in Figure 3.10: The first-level (L1) trigger is implemented on hardware, and reduced event rates from 40 MHz to 100 kHz in less than 2.5 μs right after the data happened. Working with the electrical information provided by the calorimeters and the MS, the L1 trigger employs custom-made electronics to filter and store the events in the readout sections as buffers before passing them to the High-Level trigger (HLT) [34]. Certain physics objects such as photons, jets and leptons are identified in the L1 trigger, in which energy depositions of electrons and photons in the EM calorimeter and jets in the hadronic calorimeter are provided. Information of tracks in high-momentum muons is recorded in the layers of the MS and forwarded to the L1

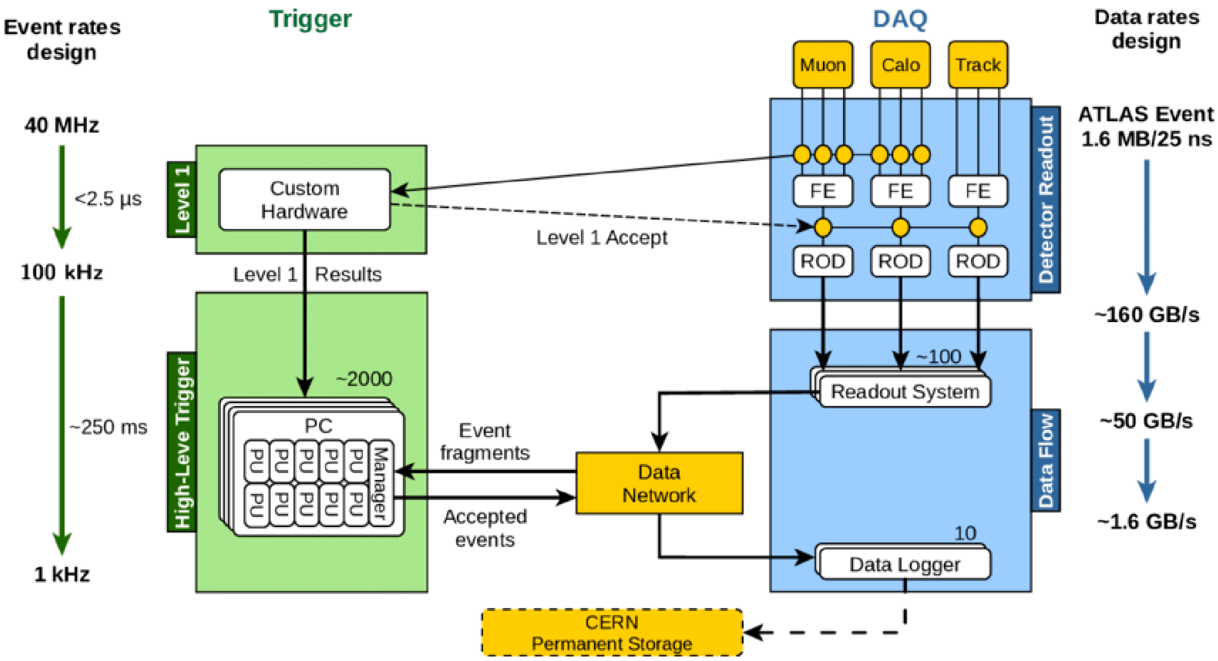

Figure 3.10 illustration of the ATLAS Run 2 trigger and data acquisition system.

trigger.

The events are further reduced from 100 kHz to 1 kHz in merely 250 microseconds by the second level trigger: HLT. Based on the offline software, the HLT utilize fast selection algorithms to analyse and reject events in the early stage, resulting in better precision and intense CPU usage of about 1.6 GB per second. The accepted data from the HLT will be passed to permanent storage at CERN via Data Logger [35].

4 Jets in ATLAS

In the LHC, a large number of quarks and gluons are produced during the inelastic proton-proton collisions, resulting in jets. These collimated outcome particles are hadronised because of colour confinement in the QCD process. As a result of this, only colour-neutral jets clustered by particles can be seen in the detector.

The information of jets is crucial to most of the analysis such as the measurements of the SM particles and searches for the BSM phenomena. Good qualities of jets, for example the high efficiency of jet reconstruction, jet energy calibration including energy scale and energy resolution, are thus important to the analysis.

4.1 Jet reconstruction

Jets are defined in two way: MC simulated jets at particle level and detector level jets with the information from the ID and calorimeters. The production and hadronisation processes of jets are illustrated in Figure 4.11.

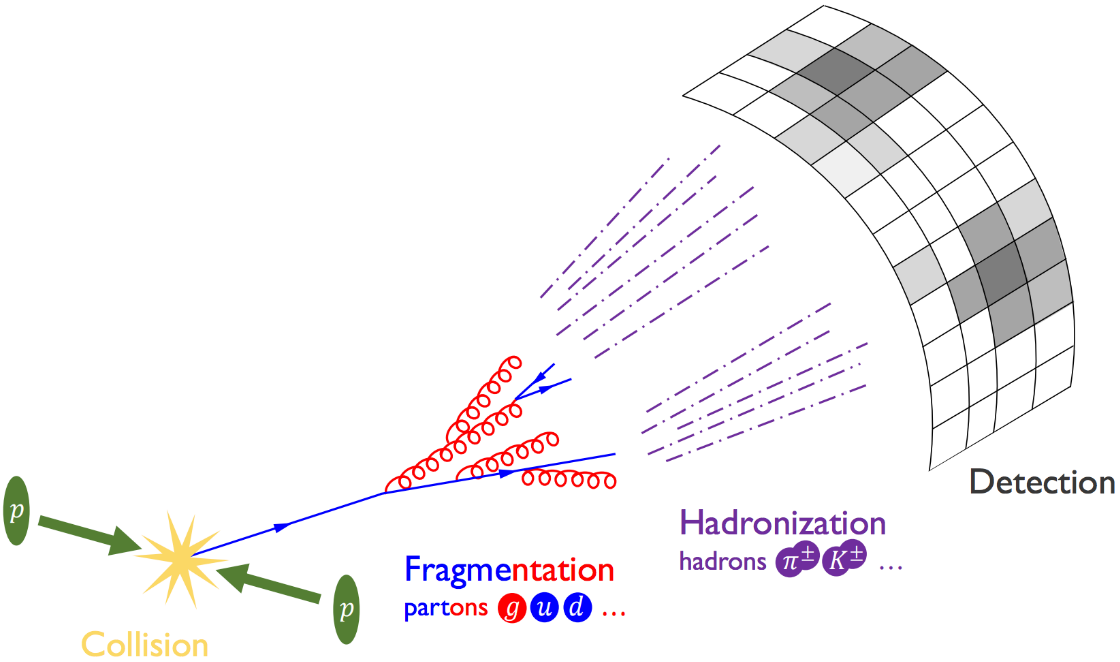

Figure 4.11 illustration of jets produced by pp collision and hadronised before seen by the detector.

Jets from the MC simulation are defined as truth-particle jets which have lifetimes longer than 10 ps as stable particles. Truth-particles indicate the ideal measurement from a detector under perfect-condition and high resolution without defects or the effects from pile-up (background interactions per bunch-crossing in the LHC). Whereas track jets are constructed with the use of charged information in the ID, and calorimeter jets with the use of energy information in the calorimeters.

There are several types of jets aim for different analysis depended on the constituents and algorithm used for reconstructing the jets. ATLAS previously used topological clusters (topo-clusters) jets, which is a group of topological related cells in calorimeter with significantly high energy deposits. A pile-up suppressed algorithm is applied to select certain cells with low noise. Cell above certain signal-to-noise (S/N) threshold (usually by four times its standard deviation) are used to seed the algorithm. By neighbouring the seed a topo-cluster is defined. In the hard-scatter process, jets of interest are expected to produced from the primary interaction point (known as vertex). The primary vertex is defined if there are at least two tracks with the highest sum of squared track momentum associated to it.

Jets are constructed from any set of four-vectors. EMTopo jets are the jets that use topo-cluster initially calibrated to electromagnetic (EM) scale in the calorimeters. A local cluster weighting (LCW) scale is also used for calibrating hadronic clusters by applying weights for low hadronic interaction response. Besides, particle flow (PFlow) [36] jets are built by combining the information from both the ID and the calorimeter, where the energy that charged particles deposit in the calorimeter is deducted from the detected topo-clusters and replaced by the momenta of tracks that are matched to those topo-clusters. Consequently, the PFlow jets produced through this method demonstrate enhanced energy and angular precision, higher reconstruction efficacy, and better stability in the face of pile-up, in comparison to jets reconstructed solely from calorimeter data.

A recombination algorithm called anti-k_t algorithm is employed to build the jets with a radius parameter R in rapidity-azimuth $(y-\phi)$ plane around a cluster. The algorithms are defined as follows:

$$d_{ij} = \min\left(k_{\mathrm{t}i}^{2p}, k_{\mathrm{t}j}^{2p}\right)\frac{\Delta_{ij}^{2}}{R^{2}} \tag{4.1}$$

$$\Delta_{ij}^{2} = (y_i - y_j)^2 + (\phi_i - \phi_j)^2 \tag{4.2}$$

$$d_{iB} = k_{\mathrm{t}i}^{2p} \tag{4.3}$$

where the distance d_{ij} between any pair of particles i and j is given by the minimum transverse momenta k_t of the two particles. The geometrical distance Δ_{ij} represents the separation of a pair of particles in $(y-\phi)$ plane. Radius parameter R indicates the size of the final jets. The distance d_{iB} between any detected particle i and the beam B is also given. Parameter p indicates the relative power of of energy with respect to geometrical scales and is used to distinguish the different types of algorithms.

When p is set to 0, the Cambridge-Aachen (CA) algorithm is given as the distance d_{ij} and d_{iB} only based on spatial separation and are independent of the transverse momenta. This algorithm is usually used for large-radius jets and jet substructure performance study.

For the k_t algorithm, p is set to 1 so that the distance d_{ij} is dominated by the minimum k_t. This algorithm is preferred for clusters that are soft and collinear splits are merged first, resulted in irregular footprint with the most interesting splits.

The anti-k_t algorithm [37] on the other hand set p = -1, leaving the distance $d_{ij} \propto \min\left(\frac{1}{k_{ti}^2}, \frac{1}{k_{tj}^2}\right)$ shorten as the transverse momenta of two particles increase. This is widely used in the LHC for hard clustering as it is less vulnerable to the effects from the pile-up and resulted in circular footprint as shown in Figure 4.12 for $R = 1.0$.

For most of ATLAS analysis, jets with $R = 0.4$ are used for quarks and gluons analysis. Other ones such as $R = 1.0$ are also widely used to study energetic particles like W and Z bosons. R = 0.2, 0.6, 1.2, 1.5 and variable radii are also analysed.

The anti-k_t $R = 0.4$ PLow jets are used in the quark/gluon taggers calibration described in this thesis.

4.2 Jet calibration and cleaning

The motivation of jet calibration [38, 39] is to correct the translation from received signals to initial partons for several detector effects. At the initial stage of the process, corrections for pile-up are applied to eliminate the excess energy from extra proton-proton interactions occurring either in the same bunch crossing (in-time) or in adjacent ones (out-of-time). This adjustment involves two main parts: one is a correction dependent on the jet’ s area and the transverse momentum density of the event, and the other

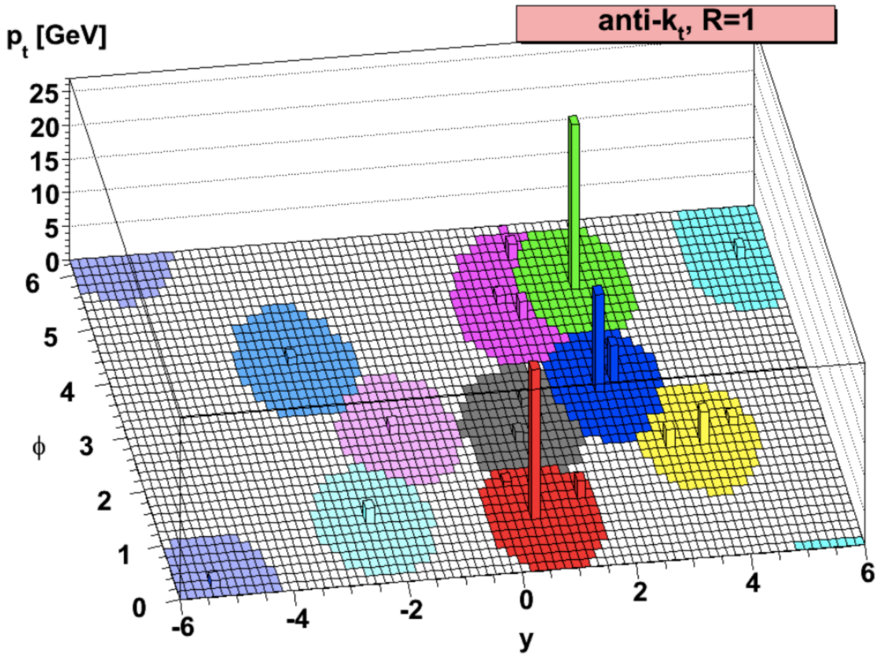

Figure 4.12 Plot of parton-level jets clustered using anti-k_t algorithms with radius parameter set to 1.

is a residual correction. This residual correction is obtained from MC simulations and is parametrized according to the average number of interactions per bunch crossing, denoted as μ, and the number of reconstructed primary vertices present in the event (NPV). The absolute Jet Energy Scale (JES) calibration aligns the jet's energy and direction with truth jets from dijet MC events. Additionally, the global sequential calibration, based on dijet MC events, enhances the jet p_{T} resolution and reduces associated uncertainties by mitigating the reconstructed jet response's dependency on variables derived from the tracking, calorimeter, and muon chamber detector systems. These calibrations are implemented on both actual data and MC simulations. Finally, an *in situ* residual calibration, exclusive to real data, rectifies any remaining discrepancies between the data and MC simulations.

The diagrams 4.13 shows the calibration scheme for small-R jets.

4.2.1 Pile-up corrections

In order to eliminate a great amount of energy deposits from pile-up, a jet area-based subtraction of pile-up contribution to the p_{T} of each jet per event is applied as the start of the calibration chain.

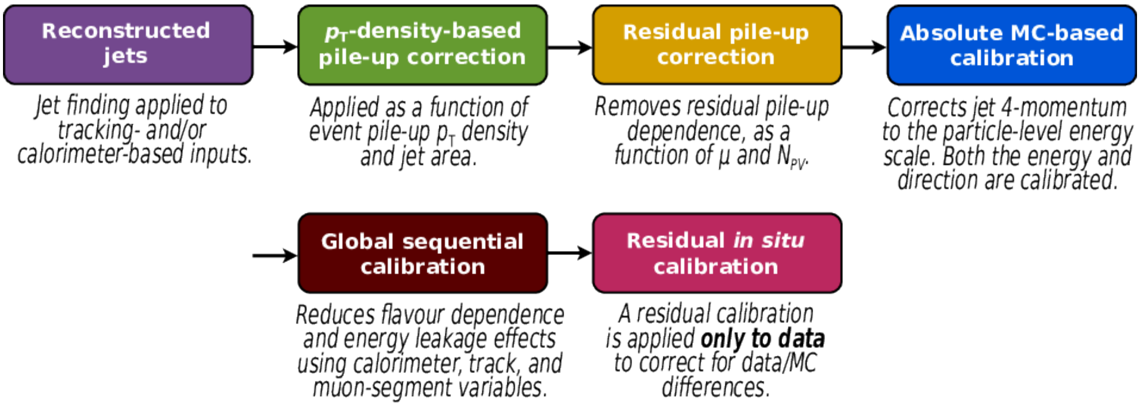

Figure 4.13 Overview scheme of jet calibration in the ATLAS.

After all pile-up corrections are applied, the jet p_{T} is given by:

$$p_{\mathrm{T}}^{\mathrm{corr}} = p_{\mathrm{T}}^{\mathrm{reco}} - \rho \times A - \alpha \times (N_{\mathrm{PV}} - 1) - \beta \times \mu \tag{4.4}$$

where $p_{\mathrm{T}}^{\mathrm{reco}}$ indicates the reconstructed jet p_{T} before any pile-up correction is applied. The jet area A is defined by certain number of ghost tracks associated with a jet after clustering thus can quantify the liability of a jet to pile-up. The pile-up p_{T} density ρ is used to evaluate the contribution from pile-up in the y-ϕ plane. To calculate the density ρ of each jet in the distribution p_{T}/A, a k_t algorithm with radius $R = 0.4$ is employed to reconstruct jet from positive-energy topo-clusters within the range of $|\eta| < 2$. The calculation of ρ performed in such η range for pile-up measurement is due to the fact that ρ tend to be zero beyond $|\eta| \approx 2$ as a result of lower occupancy in coarser segmentation in the forward region. Therefore, pile-up sensitivity in the forward region is not fully described after such correction.

An additional residual correction is thus applied from the MC simulation to account for the difference between the reconstructed jet p_{T} and truth jet p_{T} as a function of the number of reconstructed primary vertices in the event N_{PV} and the mean number of interactions per bunch crossing μ, which are sensitive to in-time and out-of-time pile-up, separately.

Both the initial values of α and β coefficients are derived in bins of truth jet p_{T} and geometric centre of the detector $|\eta_{det}|$. A logarithmic dependence on truth jet p_{T} is observed.

4.2.2 Jet energy scale and η calibration

Following the pile-up mitigation, the absolute jet energy scale and η calibration are introduced to correct the four-momentum of the reconstructed jet to the truth-particle jets, accounting for defecting calorimeter response, energy losses when particles passed through certain materials, boundary effects and biases in the reconstructed jet in different η due to the transition between the granularities and technologies changes in calorimeter.

Since the detector responses differ across the detector η range, the reconstructed jets are thus divided into small bins of η_{det} and the energy of the truth jet E^{truth} as the response distribution for fixed E^{truth} is Gaussian. The average jet energy response $\mathscr{R}$ is defined as $E^{\text{reco}}/E^{\text{true}}$ using the mean of a Gaussian fit in η_{det} and E^{truth} bins, and is further parameterized as a function of E^{reco}. Such response for PFlow jets is higher than that for EMtopo jet at low energies as the tracking information is considered.

Besides JES correction, the bias from the η of the reconstructed jet to that of the truth jet is taken into account. The bias is defined as a significant deviation from zero in the signed difference between the reconstructed jet η^{reco} and truth jet η^{truth}, separately. Then a second correction is applied as such difference is parameterized as a function of η_{det} and E^{truth}.

The calibration is derived as a function of energy and η from the MC samples which do not have the effects from pile-up, and only correct the jet p_{T} and η instead of full four-momentum. The EMtopo and PFlow jets after full JES and η calibration are regarded as EM+JES scale and PFlow+JES scale, respectively. Small non-closures beyond $|\eta_{det}| \approx 3.2$ in the calibration are seen due to approximate treatment of hadronic showers in the forward region, lead to an additional systematic uncertainty.

4.2.3 Global sequential calibration

The global sequential calibration (GSC), based the global jet observables such as the the fraction of jet energy measured in the different layer of hadronic and the EM calorimeters, the tracking information associated with the jets, and the number of muon track segment. For each observable, a series of multiplicative corrections are applied on the four-momentum as a function of p_{T}^{truth} and $|\eta_{det}|$. Considered any observable x, the correction is derived from the inverted jet response $\mathscr{R}$:

$$C(x) = \frac{\mathscr{R}^{-1}}{\langle \mathscr{R}^{-1}(x) \rangle} \tag{4.5}$$

where $\langle \mathscr{R} \rangle$ is the average jet response.

As a result, the fluctuations in the jet particle composition are reduced and the jet resolution can be improved without changing the average jet energy response which depends on the flavour and the energy distribution of the constituent particles. The shape of a jet varies between quark- and gluon-initiated jets as hadrons are often included in a quark-initiated jet with higher fraction of the jet p_{T} with higher calorimeter response.

After applied GSC for PFlow jet, the average jet p_{T} response on each observable is reduced to lower than 2% with small deviations from correlations between observables.

The fractional jet resolution $\sigma_{\mathscr{R}}/\mathscr{R}$ is derived from the jet resolution $\sigma_{\mathscr{R}}$, which is defined by the standard deviation of a Gaussian fit to the distributionof jet p_{T} response. This fractional jet resolution is used to determine the size of the fluctuations in the jet energy reconstruction.

4.2.4 Residual *in situ* calibration

The final step of the jet calibration is performed only in data to account for the differences of jet response measurement in data and the MC, the derived ratio of it is used as a correction in data. The differences are introduced by the inadequate nature of the detector materials and the imperfect simulation of the real physics processes. Such differences can be quantified by weighting the p_{T} of a jet to other reference objects that well-measured. The correction factor can be denoted as follows:

$$c = \frac{\mathscr{R}^{\mathrm{data}}_{\mathrm{in\ situ}}}{\mathscr{R}^{\mathrm{MC}}_{\mathrm{in\ situ}}} \tag{4.6}$$

the response $\mathscr{R}_{\mathrm{in\ situ}}$ represents the average ratio of the jet p_{T} to the reference object p_{T} in bins of reference object p_{T}, where the average value is founded from peak value of a Gaussian fit to the distribution. The double ratio is robust to secondary effects thus more reliable in term of the measurement of jet energy.

Three stages are carried out in such *in situ* calibration. First, η-intercalibration is performed on the energy scale of forward jets ($0.8 \leq |\eta_{det}| < 4.5$) to match the central jets ($|\eta_{det}| < 0.8$) using the jet p_{T} in dijet events. Then Z+jet and γ+jet analyses balance the measurement of p_{T} response of a well-calibrated Z boson or photon. Finally, a multijet balance (MJB) analysis is employed to calibrate low-p_{T} jets to a very high-p_{T} jet. Both MJB and Z/γ+jet analyses are used only for jets in the central region ($|\eta| < 1.2$), but are also applicable to forward jets due to the effect of the η-intercalibration. Every measurement is converted from being dependent on the reference object p_{T} to being a function of the jet p_{T}. By statistically combining the$Z$+jet and γ+jet and MJB analyses, a unified and smooth calibration is achieved, applicable across the entire spectrum of momentum.

Since the three in situ analyses (η-intercalibration, Z/γ+jet MPF, and MJB) are executed one after another, the systematic uncertainties from one analysis are carried over to the subsequent ones. Systematic uncertainties within each analysis originate from three main sources: inaccuracies in simulating physics processes, uncertainties in measuring the reference object, and uncertainties in predicting the expected p_{T} balance due to the event's topology.

To address mis-modelling, we compare predictions from two MC generators, with their discrepancy serving as the measure of uncertainty. The measurement uncertainties of the reference object are obtained from the $\pm 1\sigma$ uncertainties in each object's calibration and are then propagated throughout the analysis. Finally, event topology uncertainties are evaluated by altering the event selection criteria and observing the resulting impact on the MC simulation-to-data ratio.

5 The construction and calibration of quark/gluon jets taggers

The classification of jets originated from a quark or a gluon is useful for improving the SM measurements and searches for BSM physics at the LHC. According to the QCD, gluons are in the adjoint representation of the $SU(3)$ gauge group thus carry both colour and anti-colour quantum numbers, whereas quarks are in the fundamental representation and have only a single colour number [40]. As a result, a gluon-initiated jet (gluon-jet) tend to have more constituents and a broader radiation pattern than a quark-initiated jet (quark-jets).

The manifestation of colour charges is intrinsic to quarks and gluons; however, the confinement phenomenon inherent in QCD theory indicates that only colour neutral hadrons can be observed in the detector. Such principle brings significant challenges for the identification of quark- or gluon-jets in ATLAS. The identification method relies on the number of charged tracks within the jets and the reconstruction algorithm for it. The calibration described in this paper demonstrates the measurement of the tagging efficiencies of the aforementioned jet taggers. The more advanced boosted decision tree (BDT) algorithm is employed to constructed the jet tagging variable based on the charge multiplicity inside jets. A matrix method is established with the use of quark/gluon fraction in quark-/gluon-enriched subsamples, defined by the pseudorapidity of jets. The scale factors extracted from the difference between data and simulation are provided for tagger working points corresponding to 50%, 60%, 70% and 80% fixed quark-jet efficiencies for both quark- and gluon-jets, respectively.

In addition to earlier investigations that concentrated on single-variable taggers within a lower p_{T} range [41, 42], this research emphasizes the development of a novel q/g tagger that incorporates multiple jet substructure parameters. Additionally, it aims to expand the application of q/g tagging to a broader energy spectrum.

5.1 Data and Monte Carlo samples

5.1.1 Data

The data recorded in 2015-2018 with integrated luminosity of 140 fb^{-1} (full Run 2 data)[43] is used in this study. The data samples are processed through the un-skimmed DAOD_JETM1 derivation scheme in order to obtain multi-jet events. The lowest unprescaled small-R single-jet trigger is employed for this analysis. The jet p_{T} threshold for the trigger in this analysis is 420 GeV, keeping the selection consistent across years, together with additional requirements that ensure events of good qualities are used [44]. The additional selections are:

- Good Run List (GRL): Make sure a steady state of all relevant detectors so that physics processes recorded by them are good.
- LAr: Liquid Argon Calorimeter error rejected.
- Tile: Tile Calorimeter error rejected.
- SCT: SCT single event upsets rejected.
- Core: Incomplete event build rejected.
- Primary Vertex: the highest $\sum p_{\mathrm{T}}^2(trk)$ vertex has at least two tracks associated with it
- Trigger: Passes the lowest unprescaled single-jet trigger, HLT_j420

Additional kinematic selection criteria are discussed in Section 5.2.

5.1.2 Monte Carlo simulation

For this calibration, multi-jet events are generated and modelled with several MC simulations, processed through the same DAOD_JETM1 derivation scheme. For the nominal result, PYTHIA 8.230 [45] MC generator is used with leading-order (LO) matrix element (ME) for dijet production. Parton density functions (PDFs) are considered for systematic uncertainties evaluation as the PDF set [46] is used for PYTHIA 8.230 with the A14 tune [47]. Alternative samples with different choices of parton shower modelling, ME generation, and the simulation of the multi-parton interactions are included to estimate the systematic uncertainties.

Two set of MC samples generated using SHERPA 2.2.5 [48] are used with the same ME for the (2→2) process at LO, to provide the uncertainties of hadronisation modelling [49, 50]. The CT10 PDF [51] sets are included in both SHERPA samples where one based on the cluster hadronisation whereas the other used SHERPA interface to the Lund string fragmentation [52] model as PYTHIA 8.230.

Two set of MC samples generated using HERWIG 7.1.3 [53] are used for parton shower uncertainties as one uses angular ordering shower whereas the other one uses dipole shower. These samples are produced at next-to-leading order (NLO) with a PDF set of MMHT [54].

Another set of multijet samples that produced with POWHEG [55, 56, 57] interfaced to PYTHIA at NLO accuracy is employed with NNPDF2.3 LO PDF [58] set, to estimate the effects from the ME uncertainty as different perturbative scales in the ME and parton distribution functions are included. The renormalization and factorisation scales are set to the p_{T} of the underlying Born configuration. These samples included different perturbative scales in the ME and parton distribution functions are used for the estimation of ME uncertainty.

A list of the MC samples used is given in table 5.1.

PDF set	Generator	Cross-section	Parton shower	Hadronisation
NNPDF2.3	PYTHIA 8.230	LO	p_{T}-ordered	String
CT10	SHERPA 2.2.5	LO	p_{T}-ordered	Cluste
CT10	SHERPA 2.2.5	LO	p_{T}-ordered	String
MMHT	HERWIG 7.1.3	NLO	Dipole	Cluster
MMHT	HERWIG 7.1.3	NLO	Angular-ordered	Cluster
NNPDF2.3	Powheg+PYTHIA	NLO	p_{T}-ordered	String

Table 5.1 The MC simulation used for the multi-jet processes in this calibration. The PDF sets, generators for a hard process, the order in α_s of cross-section calculations and the simulator of parton showers, and hadronisation are shown.

5.2 Object and event selection

In order to perform the calibration of the quark-/gluon-jet tagger, it is requisite to establish two distinct subsamples. One subsample should be predominantly composed of quark-jets, called quark-enriched sample, while the other should predominantly consist of gluon-jets, as gluon-enriched sample. These subsamples are gained from the dijet events. This section describes the reconstruction and selection of jet objects used in this calibration, as well as the approach to construct quark- and gluon-enriched subsamples.

5.2.1 Physics object definition

The PFlow jets that are reconstructed with the algorithm with a radius parameter R set to 0.4. An overall jet energy calibration described in section 4.2 has been done to rectify residual detector effects and pile-up. In order to ensure a good quality jet, an event-based jet cleaning with standard loose cut is applied to reject events with flawed leading or subleading jet.

Tracks that reconstructed [59] from the ID are required to have $p_{\mathrm{T}} > 500$ MeV, and within the ID range $|\eta| < 2.5$. Additional criteria such as primary vertex are required to ensure selected tracks originating from the collision and prevent the mis-reconstructed tracks from pile-up hits in the detector. The alignment of tracks with calorimeter-based jets is executed through the application of the ghost-association technique. This entails a repetition of the jet clustering procedure augmented by the inclusion of 'ghost' representations of registered tracks [60]. These ghost tracks share the same direction as their actual counterparts but possess an infinitesimally small p_{T}, thereby ensuring that they do not induce any alterations to the intrinsic characteristics of the calorimeter-based jets. A criterion for track-jet correspondence is established: a given track is associated to a jet if its corresponding ghost track is contained in the jet after reclustering.

Jet reconstructed from the simulated MC is known as "truth jets" [38], with the same $R = 0.4$ algorithm as PFlow jets. Geometric correspondence between truth jets and PFlow jets is established via angular proximity, adhering to the criterion $\Delta R < 0.4$. Each truth jet is bestowed with a flavour label, referred to as a truth label [41, 42]. The truth flavour label attributed to a jet is defined by the flavour of the highest-energy parton situated within a cone of size $\Delta R < 0.4$ around the jet's axis, prior to the process of hadronisation in the parton shower. Following this definition, jets arising from the splintering of gluons into b- or c-quark pairs are labelled as heavy flavour jets. These heavy flavour jets are often identifiable by the long-lived or leptonically decaying hadrons. Therefore, no distinct discriminant tailored for heavy-flavour quarks is investigated within the current framework [61, 62]. Jets will be unlabelled if there is no corresponding truth parton with $p_{\mathrm{T}} > 1$ GeV is found within the cone surrounding the truth jet. These instances of unlabelled jets commonly emerge as a consequence of pile-up effects, and less than 1%

of the dataset used. They are thus ignored [63].

5.2.2 Event selection and definition of quark and gluon-enriched samples

Events are chosen by the single-jet trigger, HLT_j420. The jet p_{T} is required to be greater than 500 GeV, as more quark-jets and better resolution on the jet constituents are given. Only the leading two jets with the highest p_{T} are used, as dijet events, and are required to be $|\eta| < 2.5$ so that their charged constituents are collected within the coverage of the ID. To maintain the equilibrium in p_{T} and suppress non-isolated jets, a criterion demands that the ratio of the p_{T} of the leading jet to that of the sub-leading jet remains within 1.5. The two leading p_{T} jets serve as the cornerstone for the formulation of quark-enriched and gluon-enriched subsamples.

The quark-enriched sample is derived from the jet with higher $|\eta|$ among the leading two jets, while the gluon-enriched sample is extracted from the jet with lower $|\eta|$. This selection strategy capitalizes on the intrinsic behaviour of PDFs at higher proton momentum fraction range, where there exists a higher likelihood of encompassing valence quark-jets. Consequently, jets situated in more forward regions (higher $|\eta|$) have a higher probability of being quark-jets, while jets positioned closer to the central region (lower $|\eta|$) manifest an increased likelihood of corresponding to gluon-jets [64].

Selection	Multi-jet sample
Trigger	HLT_j420
Number of jets	≥ 2
$p_{\mathrm{T}}(j_1)$	> 500
$p_{\mathrm{T}}(j_2)$	> 500
$p_{\mathrm{T}}(j_1)/p_{\mathrm{T}}(j_2)$	< 1.5
$\|\eta(j_1)\|$	< 2.1
$\|\eta(j_2)\|$	< 2.1
Target parton	Quark(Higher $\|\eta\|$) or Gluon (Lower $\|\eta\|$)

Table 5.2 The selections to retrieve quark/gluon-enriched samples. "j_i" represents the i-th jet in p_{T}-ordering.

The distribution of leading and subleading jets p_{T} in dijet event after selections is shown in Figure 5.14 for both MC and data.

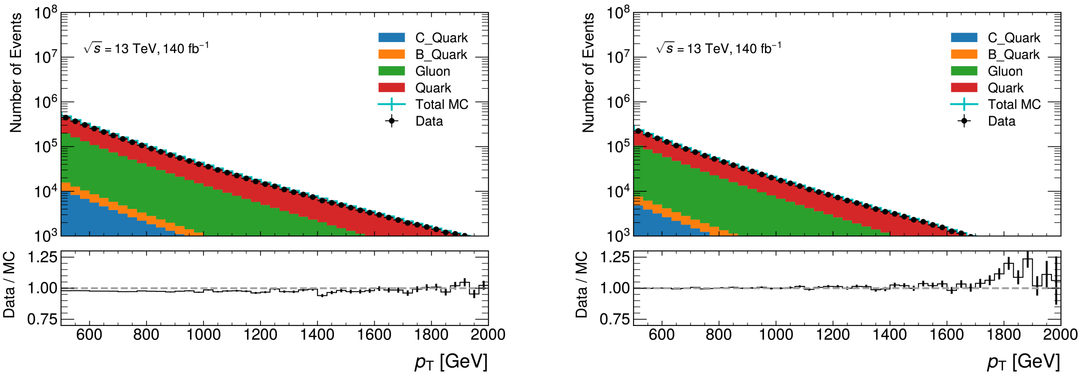

(a) leading jet

(b) subleading jet

Figure 5.14 The p_T distribution of the leading jets and sub-leading jets with PYTHIA samples for dijet event.

5.3 Quark/gluon tagger construction

According to QCD, the colour factor of gluons is larger than that of quarks by factor 9/4 ("Casimir ratio") [40], which makes gluons emit more particles in the hadronisation than quarks. As a result, a gluon-initiated jet has more charged multiplicity associated and its width is larger than that of a quark-initiated jet. Therefore, the information of the track multiplicity inside a jet is crucial to distinguish quarks from gluons.

The q/g tagging variables used in this study are based on the track multiplicity and are specified as : number of tracks (N_{trk}), jet width (W_{trk}) [41, 65], and two point energy correlation function ($C_1^{\beta=0.2}$) [66, 67] computed from the associated tracks. The expressions are defined as follows:

N_{trk}

N_{trk} is a number of tracks associated with the jet.

$$N_{\text{trk}} = \sum_{trk \in jet} \tag{5.1}$$

W_{trk}

W_{trk} is a track-p_T-weighted width of the jet divided by the scalar sum of track transverse momenta. It is defined as

$$W_{\text{trk}} = \frac{\sum_{trk \in jet} p_{\text{T,trk}} \Delta R_{trk,jet}}{\sum_{trk \in jet} p_{\text{T,trk}}}, \tag{5.2}$$

where $p_{\mathrm{T,trk}}$ is a p_{T} of a charged track reconstructed by the ID and $\Delta R_{trk,jet}$ is a distance in the $\eta - \phi$ plane between the track and the jet axis.

$C_1^{\beta=0.2}$

Two point energy correlation function is defined as

$$C_1^{\beta=0.2} = \frac{\sum_{i,j\in jet}^{i\neq j} p_{T,i} p_{T,j} \left(\Delta R_{i,j}\right)^{\beta=0.2}}{\left(\sum_{trk\in jet} p_{\mathrm{T,trk}}\right)^2}, \tag{5.3}$$

where i and j denote tracks associated with the jet and the sum runs over all the combination of two tracks. The β is fixed to 0.2, which is known to be suitable for q/g tagging.

5.3.1 The BDT tagger

Multivariate Analysis (MVA) is a technique introduced to discriminate signal from background, one type of classification algorithm in MVA is the BDT. A tree structure is built to classify datasets through a sequence of branching binary decisions. Data with desirable features is kept by discriminating algorithm whereas others are rejected. Each decision point made construct a node at each level of the decision tree, and a score is assigned to every classifier that goes into the boosting process based on its error rate. One decision node can have two or more branches to split the datasets. Such procedure is iterated from top to down so that a termination condition such as the minimum number of samples in a node or a maximum depth in a tree depth is met. A diagram of a single decision tree is shown in Figure. 5.15. After all series of cuts are applied, the BDT is defined. Therefore, a cut based on the BDT score can be employed as the most correct classification of datasets.

The BDT tagger is constructed by the combination of tracking-related observables: N_{trk}, W_{trk}, $C_1^{\beta=0.2}$ and p_{T} of a jet are included as the distribution of the track multiplicity is affected by them. In this study, the BDT score is used to classify quark- or gluon-jets from the multi jet samples, with the truth-labelled information from MC to train until a quark signal efficiency larger than 90% is reached.

The BDT tagger is trained using the LGBMClassifier from lightGBM [68] framework, and hyper-parameter tuning is performed with Optuna [69]. The MC PYTHIA samples are employed.

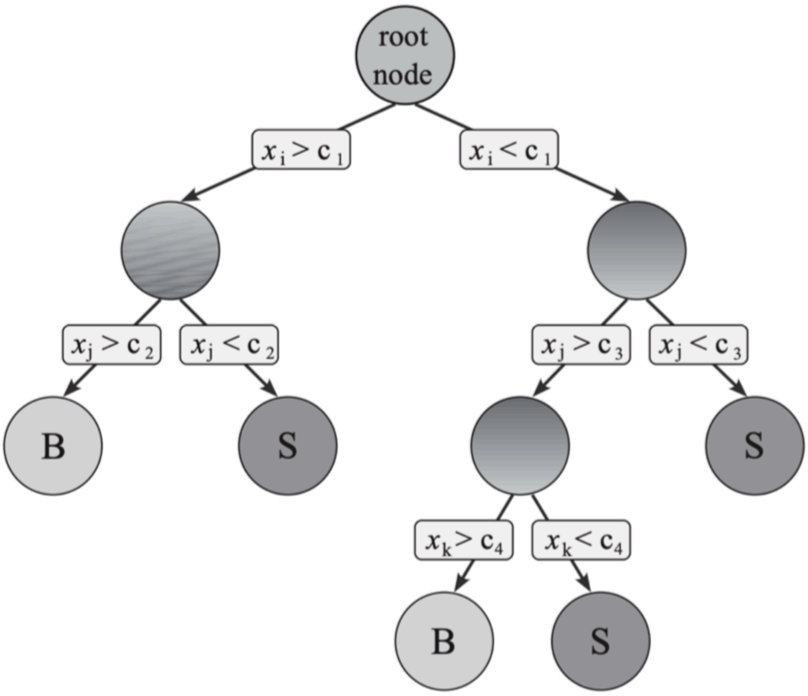

Figure 5.15 A scheme of a single decision tree with a depth of three

An individual score is allocated to each BDT within the boosting procedure, factoring in its error rate. This BDT score serves as the criterion for classifying a given jet as either a quark-jet or a gluon-jet.

5.3.1.1 Feature selections

Drawing upon the features employed during the training process, an exploration of the correlation matrix is undertaken to assess the interdependence among jet attributes, including p_{T}, $|\eta|$, and jet substructure variables N_{trk}, W_{trk}, $C_1^{\beta=0.2}$, and the BDT. Figure 5.16 shows N_{trk}, W_{trk} and $C_1^{\beta=0.2}$exhibit notable interrelationships among themselves, displaying relatively robust correlations. In contrast, p_{T} and η display a diminished level of correlation. The distributions of all single jet substructure variables and BDT score with systematic uncertainty in forward and central regions are shown in Figure 5.17. The distributions of all single jet substructure variables and BDT score with systematic uncertainty of quark- and gluon-jets in different p_{T} ranges from the MC simulation are shown in Figure 5.18.

Rather than employing multiple BDTs for different p_{T} ranges, an universal BDT can be trained using events in all p_{T} ranges. Given the intrinsic correlation between

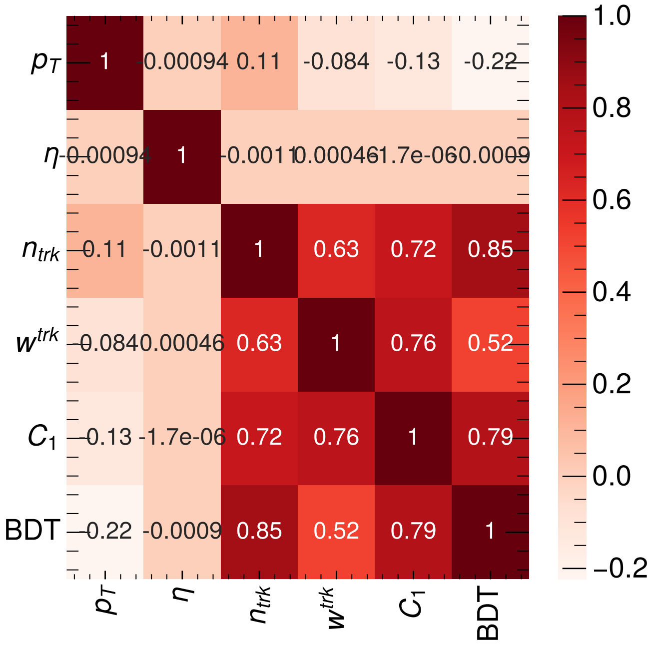

Figure 5.16 correlation matrix of jet variables.

N_{trk} and the jet p_{T}, a natural way to choose features is including p_{T} in addition to three q/g tagging variables. Concerning the remaining variable, η, two comparative scenarios are juxtaposed: one involves its inclusion, and the other pertains to its exclusion. This comparison facilitates an assessment of whether or not to incorporate $|\eta|$.

1. p_{T}, N_{trk}, W_{trk} and $C_1^{\beta=0.2}$
2. p_{T}, $|\eta|$, N_{trk}, W_{trk} and $C_1^{\beta=0.2}$

The result depicted in Figure 5.19 shows a distinct discrepancy when $|\eta|$ is encompassed within the training. This violates the assumptions that the partons distribution in more forward and more central regions should not change. Specifically, the distribution of BDT scores for forward quarks substantially diverges from that of central quarks, a trend that is similarly observed for gluons. Moreover, adopting the BDT tagger that incorporates $|\eta|$ would result in inadequate performance for jets situated within the central region when this tagger is applied to a pure sample of quark-jets (e.g., Z+jet samples). In the present analysis, the BDT is endowed with the spectra of p_{T}, N_{trk}, W_{trk}, and $C_1^{\beta=0.2}$, as exemplified in scenario 1. At detector-level, however, the observed radiation pattern

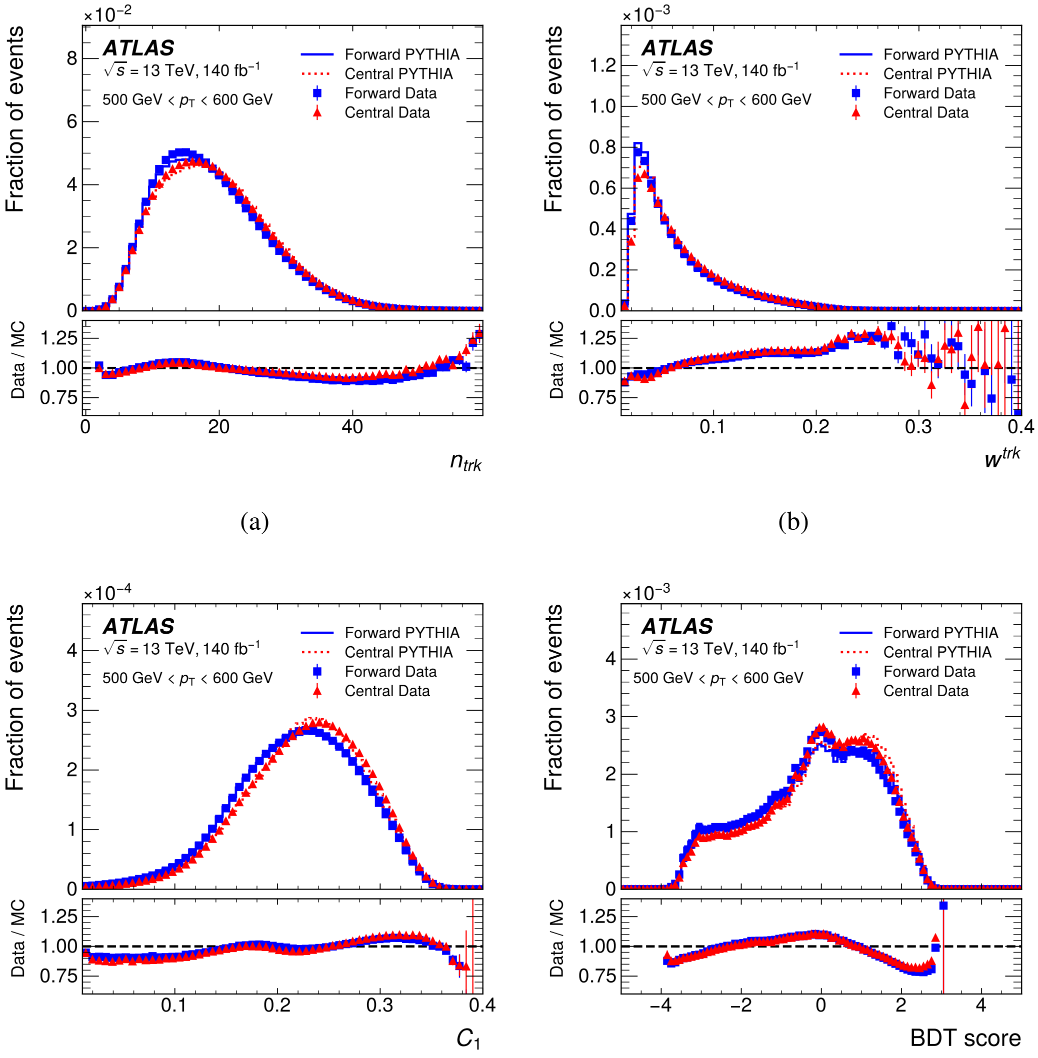

(a) (b)

(c) (d)

Figure 5.17 The distributions of N_{trk} (a), W_{trk} (b), C_1 (c) and BDT score (d) in the forward and central regions in data (closed symbols) and the PYTHIA MC (lines) are shown in the upper panels. The bottom panels show the ratio of the data and the MC. The distributions shown are for jet p_{T} in the range between 500 GeV and 600 GeV. The vertical error bars show the statistical uncertainty.

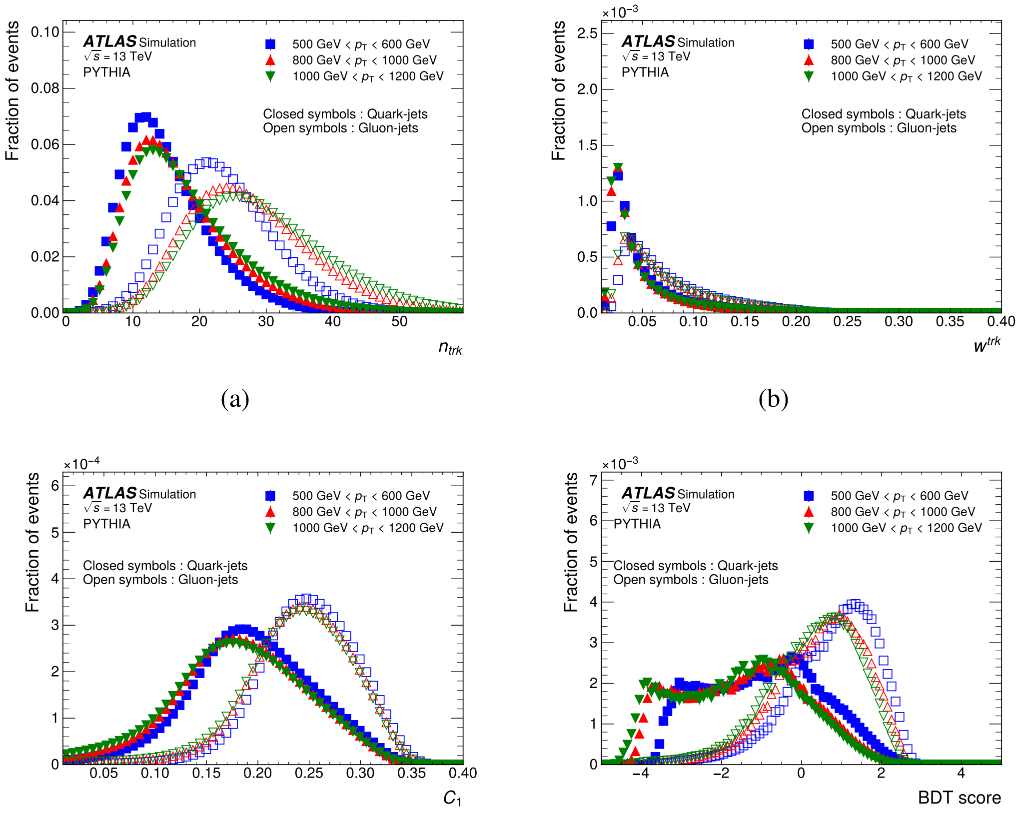

(a)

(b)

(c)

(d)

Figure 5.18 The distributions of N_{trk} (a), W_{trk} (b), C_1 (c) and BDT score (d) in the quark-jets (closed symbols) and gluon-jets (open symbols) in given p_{T} regions using the PYTHIA MC samples.

within jets no longer remains unaffected by $|\eta|$, owing to variances in the detector material and technology. To counteract this effect, a subsequent re-weighting procedure is implemented, described in Section 5.5.

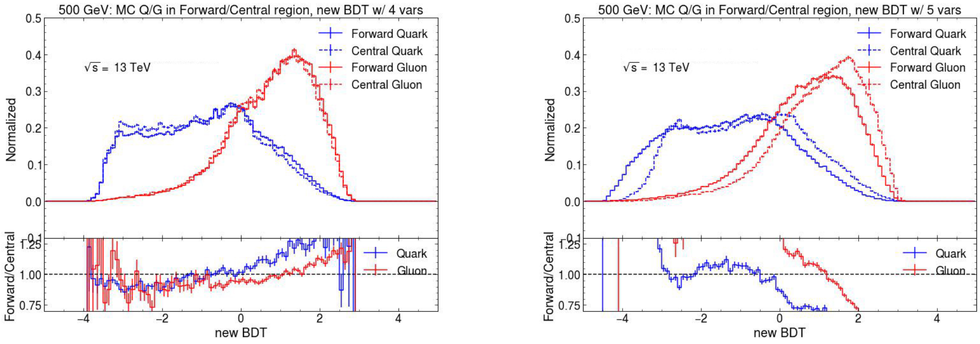

(a) Training without $|\eta|$, scenario 1

(b) Training with $|\eta|$, scenario 2

Figure 5.19 The comparison of BDT distribution for different scenarios in the jet p_{T} range from 500 to 600 GeV.

5.3.1.2 Training weights

An additional data processing step is conducted to modify the event weights, such that a flat distribution of the p_{T} spectrum is given. This adjustment is motivated by the observation that higher p_{T} jets have less probability to occur, so the training on the higher p_{T} jets need to be emphasise. This newly introduced weight, referred to as the "flat p_{T}-weight" within this context, is exclusively employed during the training process. Conversely, for other scenarios, such as assessing tagger performance on validation datasets and subsequent calibration endeavours, the original event weights based on physical considerations remain employed.

5.3.1.3 Training Configuration

Approximately 30% of the data from each period of the MC PYTHIA 8 A, D, E is randomly allocated for the training investigation, constituting an aggregate of roughly 60 million jets. The dataset division for training, validation, and testing is structured in a ratio of 80% for training, 10% for validation, and 10% for testing.

Optuna is employed to conduct a search for optimal hyperparameters. Following the hyperparameter tuning process, the most optimal model is achieved after 100 iterations of such procedure. The optimised parameters are listed:

- bagging_fraction 0.9176347488279626
- bagging_freq 2
- feature_fraction 0.9084973008559477
- lambda_l1 0.0016400096502256838
- lambda_l0.006327330258011633
- min_child_samples 13
- num_leaves 224

The performance of a classification model at all classification criteria can be illustrated using a receiver operating characteristic (ROC) curve. The idea is to compare the true positive rate (TPR, also known as sensitivity, recall or probability of detection) against the false positive rate (FPR, also known as the probability of false alarm) at different criteria given. Consider a binary classification case, where the outputs are either labelled as positive (p) or negative (n), in total there are four possible outputs from a two-class prediction problem. A true positive (TP) is given if the output from a prediction is p and the actual value is also p, otherwise a false positive (FP) is assigned if the actual value is n. Conversely, a true negative (TN) is given if both the prediction outcome and the actual value are n, whereas a a false negative (FN) is assigned if the actual value is p. TPR as a synonym for recall is defined as:

$$TPR = TP/(TP+FN) \tag{5.4}$$

while the FPR is defined as:

$$FPR = FP/(FP+TN) \tag{5.5}$$

In this analysis, the prediction true is defined by higher $|\eta|$ jet and prediction negative is defined by lower $|\eta|$ jet. The actual truth value is given by the quark jet from the MC truth information, whereas the actual negative value is given by the gluon truth information. Thus the quark efficiency is the TPR and the gluon rejection is FPR. An Area Under the ROC Curve (AUC) is used to evaluate the performance of a classifier, the better performance is indicated by higher AUC values.

Several ROC plots are made to compare different features and the BDT in different p_{T} ranges. To check whether the BDT tagger is overtrained, the shape comparison is shown in Figure 5.20, between training dataset and validation dataset. No overtraining is observed as the distribution of training dataset is very similar to that of testing dataset.

Figure 5.21 shows the ROC curve for all single jet variables and the BDT-tagger in given p_{T} ranges in forward and central regions. Figure 5.22 shows the AUC of both N_{trk}-only tagger and the BDT-tagger as a function of jet p_{T}.

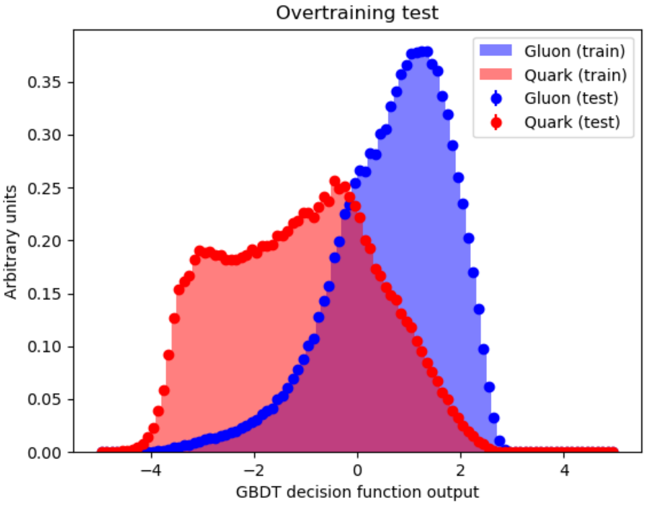

Figure 5.20 Overtraining validation

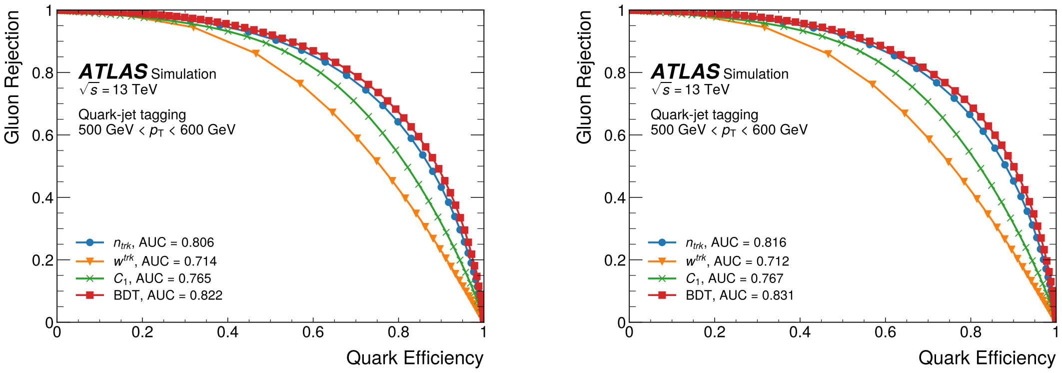

(a) Forward region

(b) Central region

Figure 5.21 The ROC Curve for different taggers in the given jet p_{T}.

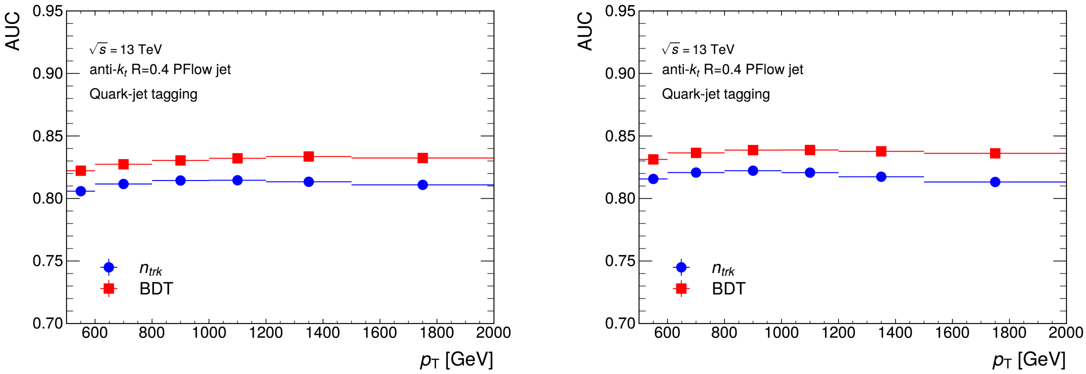

(a) Forward region (b) Central region

Figure 5.22 The AUC for different taggers across jet p_T.

The N_{trk}-only tagger is found to be the most sensitive observable than other individual jet substructure variables for q/g tagging, W_{trk} and $C_1^{\beta=0.2}$ are less sensitive to the number of tracks inefficiencies because they are defined as ratios, the BDT-tagger which include the W_{trk} and $C_1^{\beta=0.2}$ has better AUC than N_{trk}-only tagger across all jet p_T ranges. This indicates that the BDT-based tagging mechanism has a heightened capacity to discriminate against gluon-jets at the same level of efficiency in identifying quark-jets with N_{trk}-only tagger . Both taggers are calibrated in this paper, more details are presented in the next section.

5.4 Matrix Method

The distribution of q/g tagging variables depend strongly on jet p_T. Thus a matrix method [42] used to extract the shape of the q/g tagging variables is performed on each p_T bin defined in Table 5.3 for quark- and gluon-jets, separately.

p_T bin boundary [GeV]					
500-600	600-800	800-1000	1000-1200	1200-1500	1500-2000
Forward & Central $\lvert\eta\rvert$ jet samples in multi-jet					

Table 5.3 The p_T range division for the calibration of the q/g tagging variables and samples used in extraction of pure quark and gluon jets.

To measure the performance of the q/g taggers under study, samples exclusively composed of either quark-jets or gluon-jets are needed. In order to deduce the distribution shapes of the q/g tagging variables pertaining to quark- and gluon-jets within the empirical data, a methodology that capitalizes on samples possessing varying q/g ratios is employed. This approach, known as the matrix method [42], facilitates the extraction of the distinct distributions of q/g tagging variables for the aforementioned jet categories.

Pure quark- or gluon-jets can be extracted from forward and central jet samples following the matrix:

$$\begin{pmatrix} p_F(x) \\ p_C(x) \end{pmatrix} = \underbrace{\begin{pmatrix} f_{F,Q} & f_{F,G} \\ f_{C,Q} & f_{C,G} \end{pmatrix}}_{\equiv F} \begin{pmatrix} p_Q(x) \\ p_G(x) \end{pmatrix} \tag{5.6}$$

$$\begin{pmatrix} p_Q(x) \\ p_G(x) \end{pmatrix} = F^{-1} \begin{pmatrix} p_F(x) \\ p_C(x) \end{pmatrix}. \tag{5.7}$$

where $p_{Q,G}(x)$ represents the distributions of the q/g tagging variable x in pure quark- and gluon-enriched jet samples, $p_F(x)$ and $p_C(x)$ show the distributions of jet variables in forward and central regions, respectively, $f_{F/C,Q/G}$ are the fractions of quarks and gluons in a forward or central region. The inverse matrix of F is thus constructed and used to extract pure quark/gluon $p_{Q,G}$. Data is used to obtain the distributions of the quark- and gluon-enriched samples, MC is used to calculate the fraction of quarks and gluons in them as shown in Figure 5.23, as well as the distributions of q/g tagging variables. The matrix is calculated in each x bin and each jet p_{T} range.

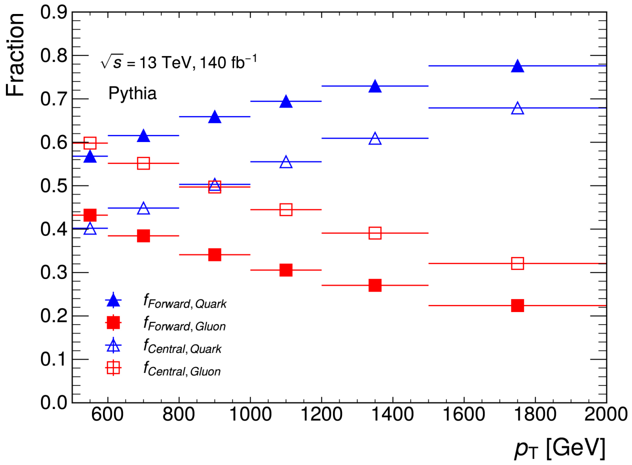

(a)

Figure 5.23 Fractions of quark-jets and gluon-jets in forward jet and central jet regions from PYTHIA dijet process. These values are used as elements in F matrix in Equation 5.6.

5.5 MC non-closure

The matrix method is valid under the assumption that the shapes of $p_Q(x)$ and $p_G(x)$ remain consistent, regardless of whether the jets are situated in the central or forward regions. Jet fragmentation at a pp collider is expected to be predominantly influenced by the jet p_{T} and is generally considered independent of η, considering the underlying parton type. Consequently, an approach aimed at extracting distributions associated with the radiation patterns of quark-jets and gluon-jets should be valid at the particle level. At the detector level, however, the measured radiation pattern within jets no longer retains its η-independence. This is due to variations arising from differences in detector materials and technologies, leading to distinctions between the central and forward regions in terms of response. As a consequence of these effects, the matrix method experiences deviations from closure,, indicating a disparity between the expected and actual outcomes.

The distributions of N_{trk} have been seen to have systematic difference for the truth-labelled quark/gluon jets in the quark-enriched and gluon-enriched regions in each p_{T} bin. To rectify this discrepancy and ensure alignment in the distribution of jet tagging variables between the central and forward regions, a re-weighting procedure is implemented. This procedure involves applying adjustments to account for the observed differences.

For each event, the central jet is weighted by a re-weighting factor :

$$w_{\mathrm{Q/G}}\left(x; p_{\mathrm{T,j}}\right) = \frac{p_{\mathrm{Q/G,\ forward}}\left(x; p_{\mathrm{T,j}}\right)}{p_{\mathrm{Q/G,\ central}}\left(x; p_{\mathrm{T,j}}\right)} \tag{5.8}$$

where q/g tagging variable x is calculated in each jet p_{T} bin for quark and gluon jets, respectively. By default the re-weighting factor derived from truth-labelled quark-jets is implemented for both types of jets, whereas the re-weighting factor derived from truth-labelled gluon-jets is used as an alternative to evaluate the systematic uncertainty from the re-weighting procedure, known as MC non-closure systematic uncertainty for the calibration.

The distributions of N_{trk} in extracted pure quark- and gluon-jets and truth-labelled MC before re-weighting as shown in Figure 5.24. After the re-weighting the distributions of N_{trk} are shown in Figure 5.25. The non-closure is at few percent level and is is taken as MC non-closure systematic uncertainty.

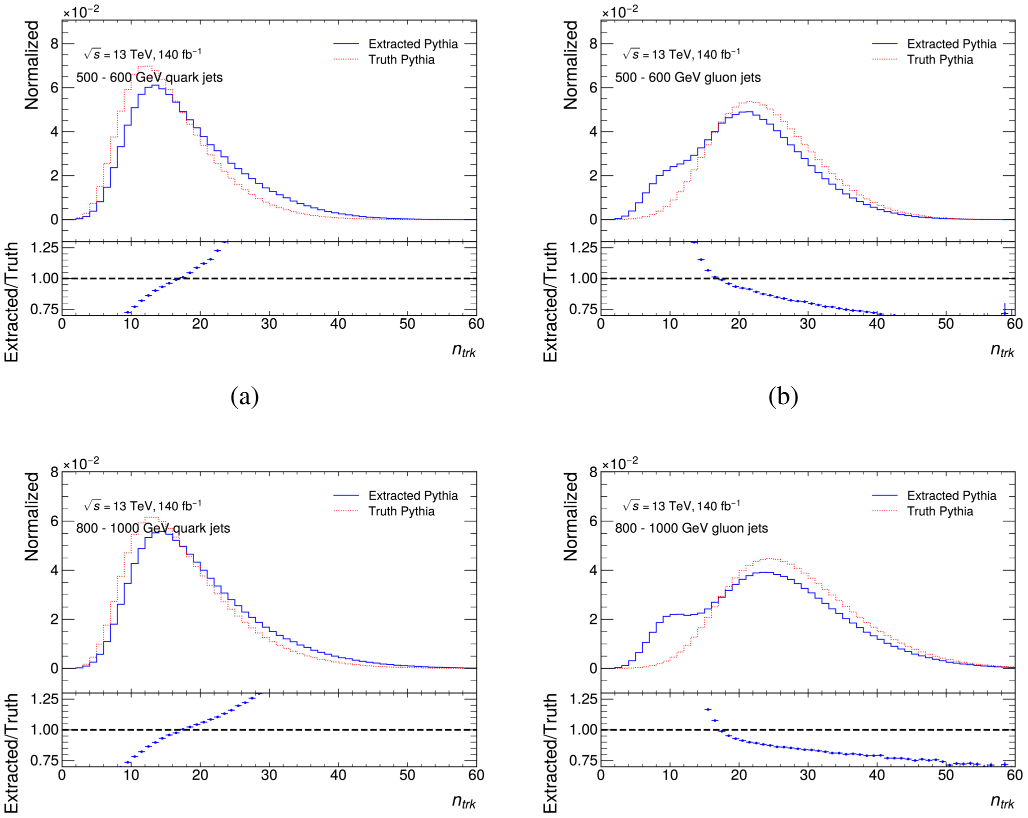

(a) (b)

(c) (d)

Figure 5.24 Before re-weighting: the N_{trk} distributions of quark-jet (a) (c) and gluon-jet in (b) (d) from PYTHIA 8 sample. Dashed and solid-line show the N_{trk} distributions in the truth MC and extracted MC, respectively. Bottom panels show the ratio of the extracted MC to the truth MC.

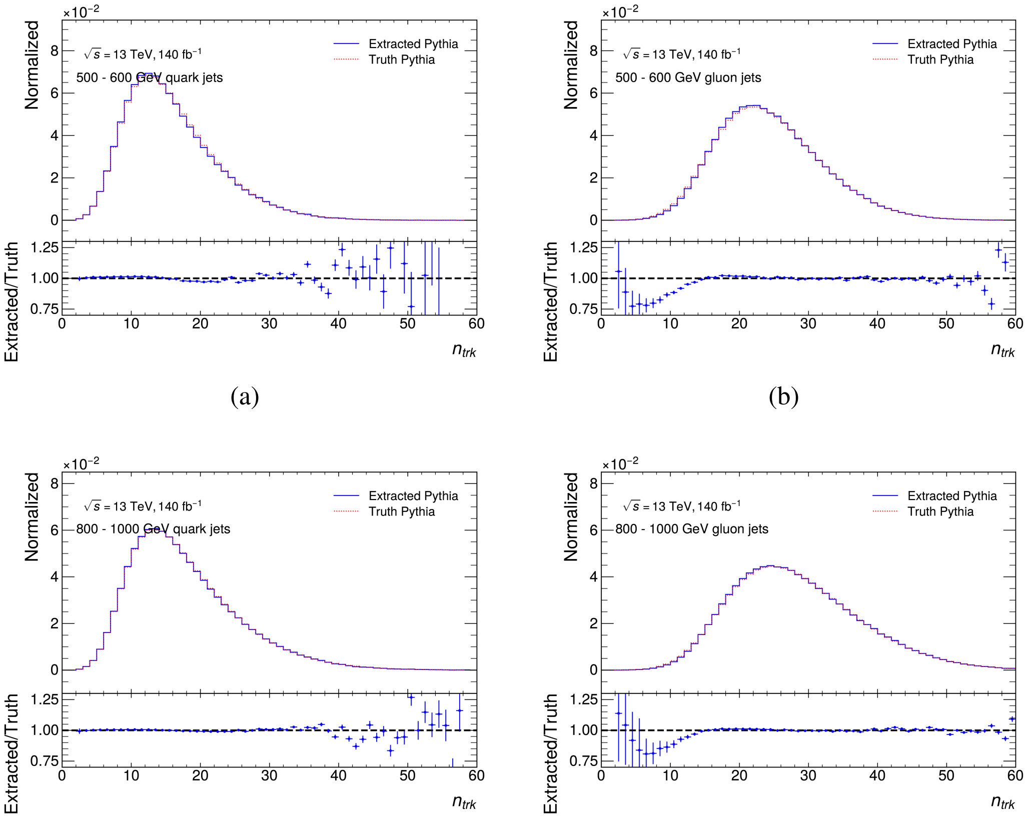

(a) (b)

(c) (d)

Figure 5.25 After re-weighting with quark factor: the N_{trk} distributions of quark-jet (a) (c) and gluon-jet in (b) (d) from PYTHIA 8 sample. Dashed and solid-line show the N_{trk} distributions in the truth MC and extracted MC, respectively. Bottom panels show the ratio of the extracted MC to the truth MC.

5.5.1 Closure test for BDT tagger

Similar to the distribution of N_{trk}, the distributions of BDT score for truth labelled-jets exhibit systematic disparities in forward and central regions. Therefore, the same re-weighting procedure as described is performed for BDT tagger as well. The MC non-closure test is thus conducted by comparing the distributions of BDT score for extracted and truth quark- and gluon-jets, separately, as shown in Figure 5.26. The distributions of BDT before and after re-weighting are shown in Figure 5.27 and Figure 5.28. The non-closure is about few percent level and taken as one systematic uncertainty.

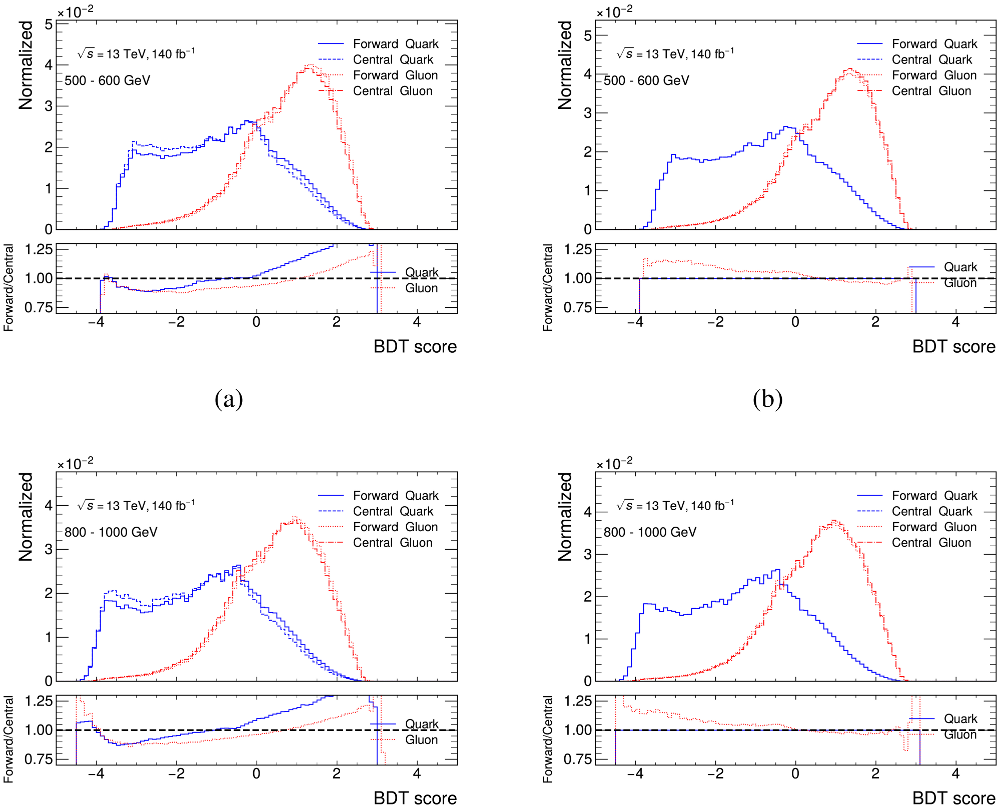

(a) (b)

(c) (d)

Figure 5.26 The distribution of BDT score for jets before (a) (c) and after (b) (d) re-weighting.

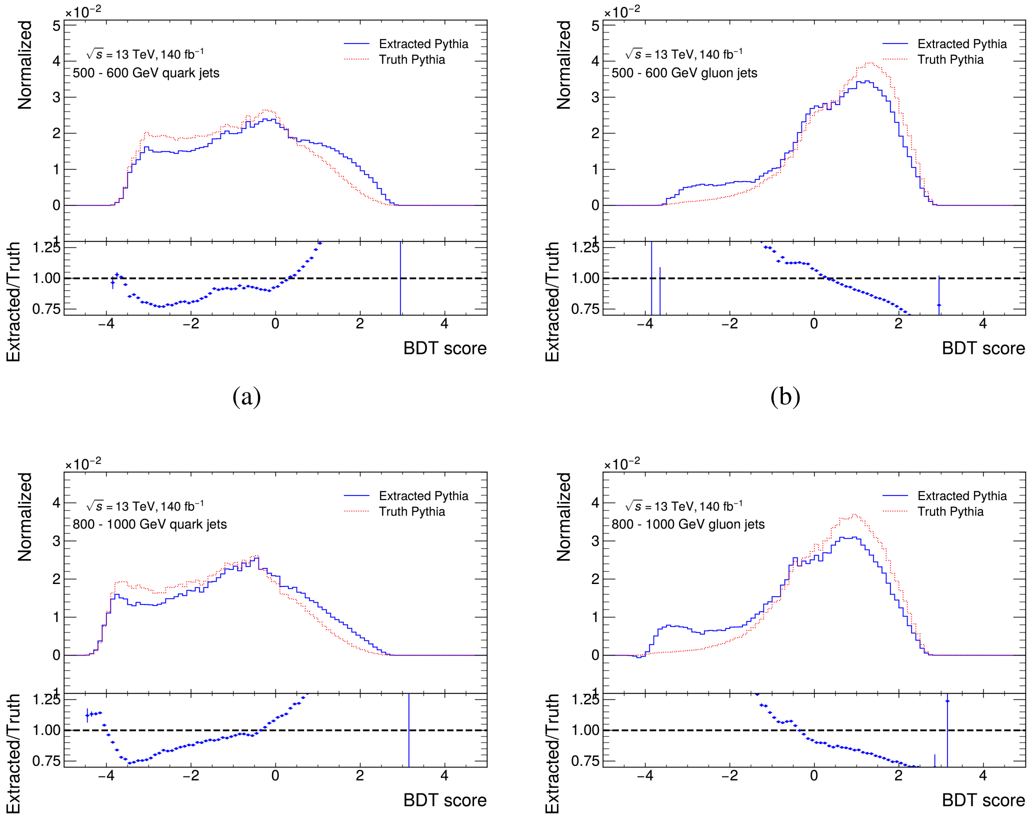

(a) (b)

(c) (d)

Figure 5.27 Before re-weighting: the MC-closure for quark-jet in (a) (c) and for gluon-jet in (b) (d) in BDT distributions from PYTHIA 8 sample. Dashed and solid-line histograms show the BDT distributions in the truth MC and extracted MC, respectively. Bottom panels show the ratio of the extracted MC to the truth MC.

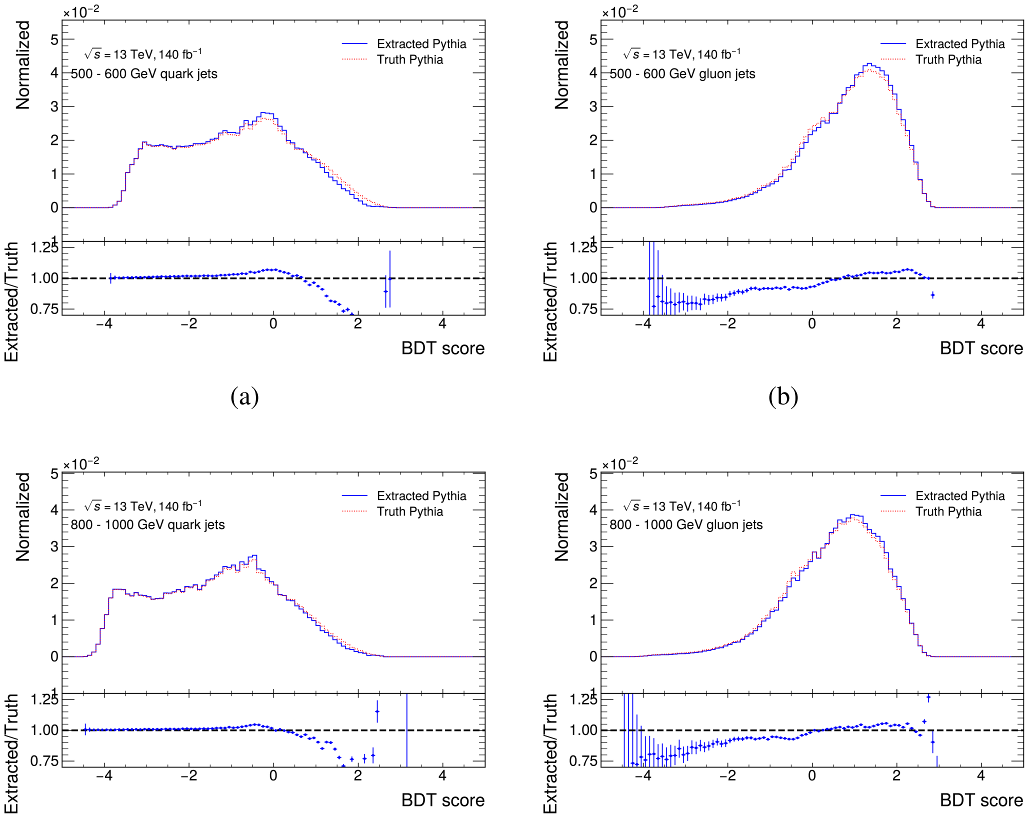

(a) (b)

(c) (d)

Figure 5.28 After re-weighting: the MC-closure for quark-jet in (a) (c) and for gluon-jet in (b) (d) in BDT distributions from PYTHIA 8 sample. Dashed and solid-line histograms show the BDT distributions in the truth MC and extracted MC, respectively. Bottom panels show the ratio of the extracted MC to the truth MC.

5.5.2 Summary for the MC Closure test

After applied the re-weighting factor to the jet tagging variables N_{trk} and BDT, the distributions of extracted quark-and gluon-jets converge with those of truth jets. The residual discrepancy, which has only few percent level to the total events is taken into account as MC non-closure systematic uncertainty. No obvious dependency on jet η is observed from the distributions of jet tagging variables.

5.6 Scale factor

The calibration of the q/g tagging variables is performed by applying binned scale factor (SF) in the simulation for each quark- and gluon-jet, respectively. The scale factor is obtained from distributions of the variables in quark- and gluon-jets from MC in order to match the shape of the simulation to that of the data.

The tagger working points (WP) are established for fixed quark-jets efficiency in the nominal MC sample, for both taggers. At a given working point, the efficiencies for quark- and gluon-jets are defined as follows:

$$\varepsilon_{Q/G}(x^{WP}) = \int_{x<x^{WP}} p_{Q/G}(x)dx. \tag{5.9}$$

Rejection factors corresponding to quark- and gluon-jets can also be given as:

$$\xi_{Q/G}(x^{WP}) = 1/\int_{x>x^{WP}} p_{Q/G}(x)dx = 1/(1-\varepsilon_{Q/G}(x^{WP})). \tag{5.10}$$

Discrepancies observed between the quark-jet tagging efficiencies and gluon-jet rejections obtained from data and the corresponding values anticipated from the MC simulations are quantified using data-to-MC scale factors (SF). These factors are computed separately for each q/g tagger in various p_{T} bins, at a fixed WP. The SF is defined using Equation 5.9 and 5.10 for quark- and gluon-jets, respectively :

$$\text{SF}_Q(x^{WP}) = \frac{\varepsilon_Q^{\text{Data}}(x^{WP})}{\varepsilon_Q^{\text{MC}}(x^{WP})}. \tag{5.11}$$

$$\text{SF}_G(x^{WP}) = \frac{\xi_G^{\text{Data}}(x^{WP})}{\xi_G^{\text{MC}}(x^{WP})}. \tag{5.12}$$

where $\varepsilon^{\text{Data}}_{Q/G}(x^{WP})$ and $\varepsilon^{\text{MC}}_{Q/G}(x^{WP})$ are $\varepsilon_{Q/G}(x^{WP})$ in data and MC, respectively. Same definitions apply to $\xi_{Q/G}(x^{WP})$. The WPs corresponding to fixed quark-jets tagging efficiencies of 50%, 60%, 70%, and 80% have been examined, revealing analogous trends in the characteristics of SFs.

Figure 5.29 to 5.32 show the distribution of all jet tagging variables in quark- and gluon-jets after matrix method extraction in all different MC samples and data in given p_{T} range.

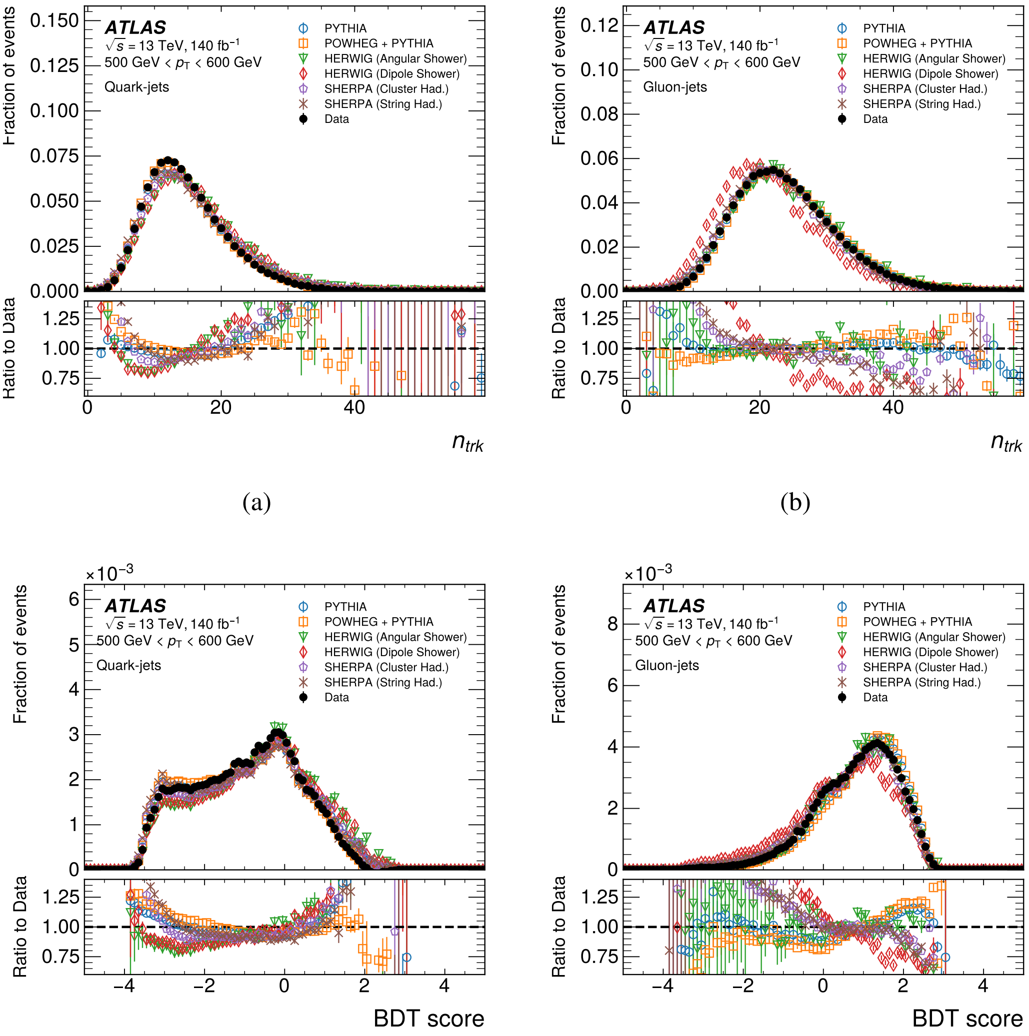

(a) (b)

(c) (d)

Figure 5.29 The distributions of N_{trk} (a,b) and BDT score (c,d) for quark-jets (left) and gluon-jets (right) using different generators (open symbols) and data (closed symbol) are shown in the upper panels. The lower panels show the ratio of each MC distribution and the data. The vertical error bars show the statistical uncertainty.

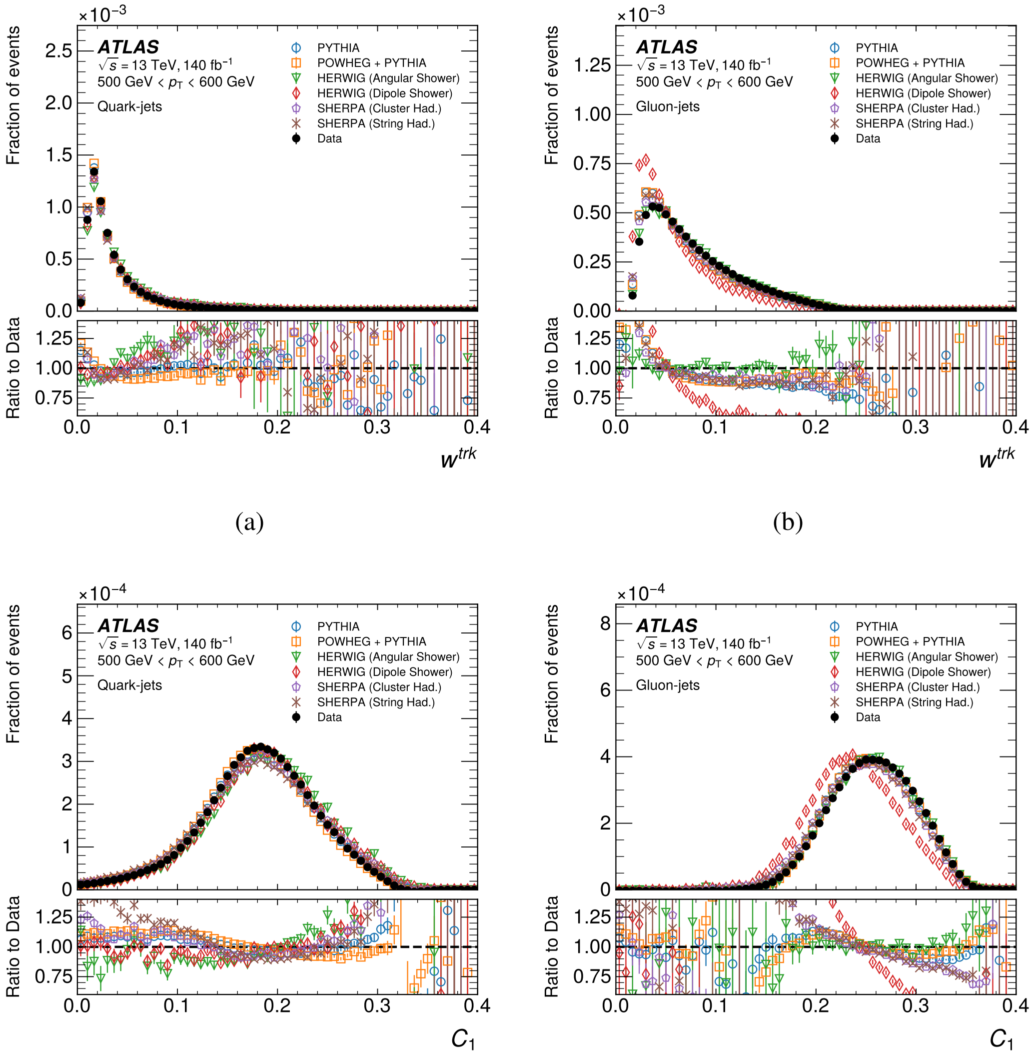

(a)

(b)

(c)

(d)

Figure 5.30 The distributions of W_{trk} (a,b) and C_1 (c,d) for quark-jets (left) and gluon-jets (right) using different generators (open symbols) and data (closed symbol) are shown in the upper panels. The lower panels show the ratio of each MC distribution and the data. The vertical error bars show the statistical uncertainty.

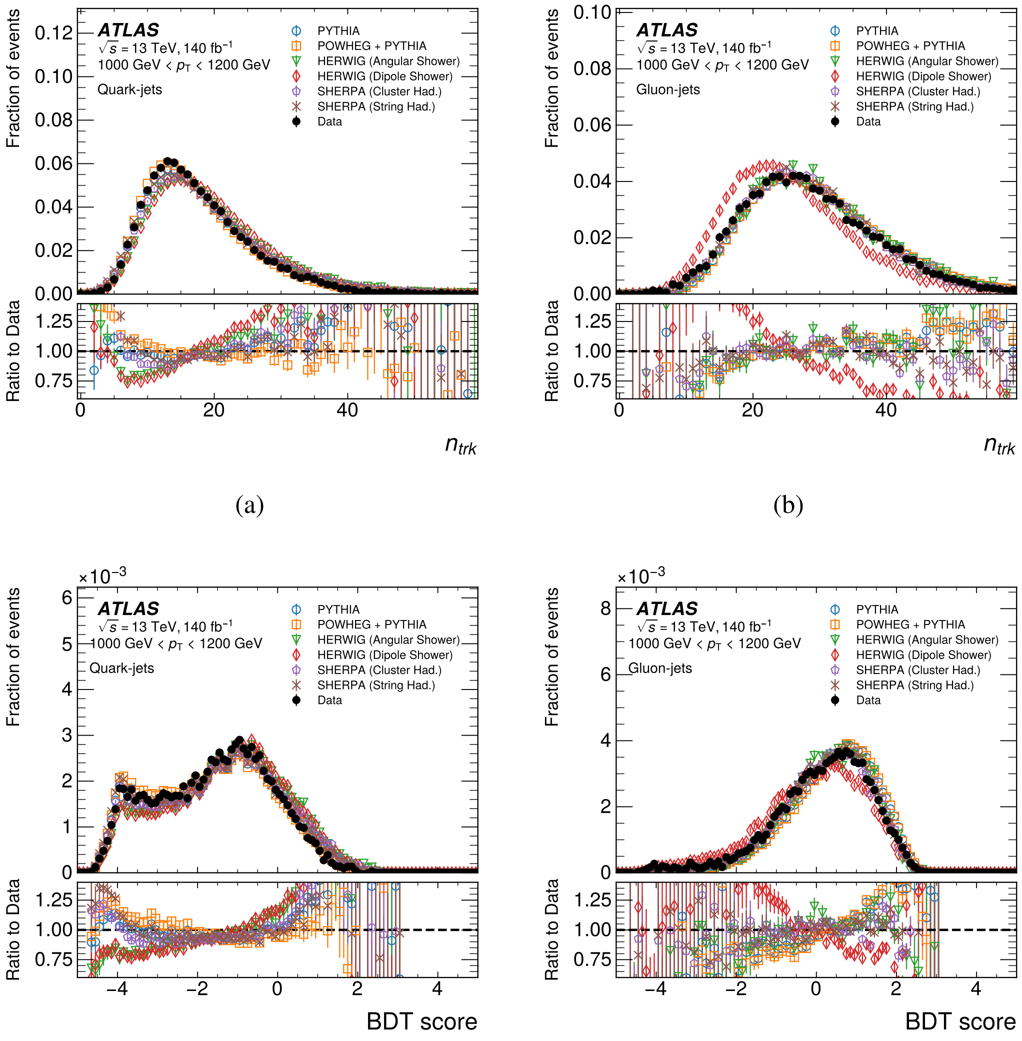

(a)

(b)

(c)

(d)

Figure 5.31 The distributions of N_{trk} (a,b) and BDT score (c,d) for quark-jets (left) and gluon-jets (right) using different generators (open symbols) and data (closed symbol) are shown in the upper panels. The lower panels show the ratio of each MC distribution and the data. The vertical error bars show the statistical uncertainty.

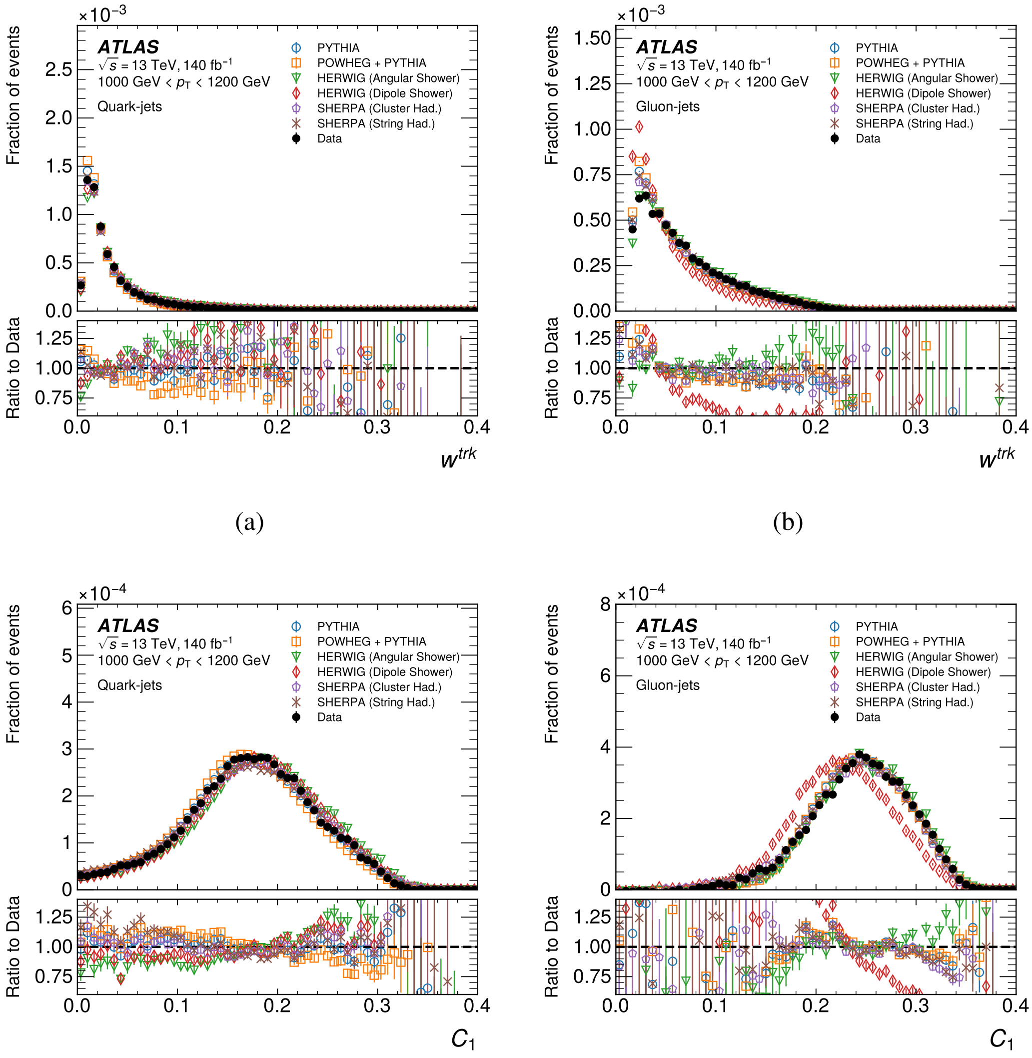

(a) (b)

(c) (d)

Figure 5.32 The distributions of W_{trk} (a,b) and C_1 (c,d) for quark-jets (left) and gluon-jets (right) using different generators (open symbols) and data (closed symbol) are shown in the upper panels. The lower panels show the ratio of each MC distribution and the data. The vertical error bars show the statistical uncertainty.

Cut values corresponding to the 50% WP are summarised in Table 5.4 for the N_{trk}-only tagger and Table 5.5 for the BDT-tagger. Figure 5.33 shows the gluon-jets efficiency of both N_{trk}-only tagger and the BDT-tagger as a function of jet p_{T}, for the MC and data, at four WPs.

Both the N_{trk}-only and BDT-taggers demonstrate commendable performance on data, with high quark signal efficiency across all p_{T} range. Notably, at the 50% working point, the N_{trk}-only tagger achieves approximately 90% rejection of gluon-jets, while the BDT tagger surpasses this performance by rejecting around 93% of gluon-jets. The BDT-tagger outperforms the N_{trk}-only tagger by exhibiting superior gluon-jets rejection rates at the identical WP. This disparity in performance arises from the inclusion of a more comprehensive set of jet substructure variables in the BDT approach. The discrepancy between the level of gluon-jet rejection observed in data and that predicted by the MC samples increases as the jet p_{T} increases. This phenomenon is closely tied to the dissimilarity between the modelling of gluons and their actual behaviour in data.

p_{T} [GeV]	500 - 600	600 - 800	800 - 1000	1000 - 1200	1200 - 1500	1500 - 2000
WP						
0.5	15.0	16.0	17.0	18.0	18.0	19.0
0.6	17.0	18.0	19.0	20.0	20.0	21.0
0.7	19.0	20.0	21.0	22.0	23.0	24.0
0.8	22.0	23.0	24.0	26.0	27.0	28.0

Table 5.4 Cut values of N_{trk} at different working point in each of jet p_{T} range

p_{T} [GeV]	500 - 600	600 - 800	800 - 1000	1000 - 1200	1200 - 1500	1500 - 2000
WP						
0.5	-0.8	-1.0	-1.2	-1.4	-1.6	-1.8
0.6	-0.4	-0.6	-0.8	-1.0	-1.2	-1.4
0.7	0.0	-0.2	-0.4	-0.6	-0.8	-1.0
0.8	0.4	0.2	0.0	-0.2	-0.3	-0.6

Table 5.5 Cut values of BDT at different working point in each of jet p_{T} range

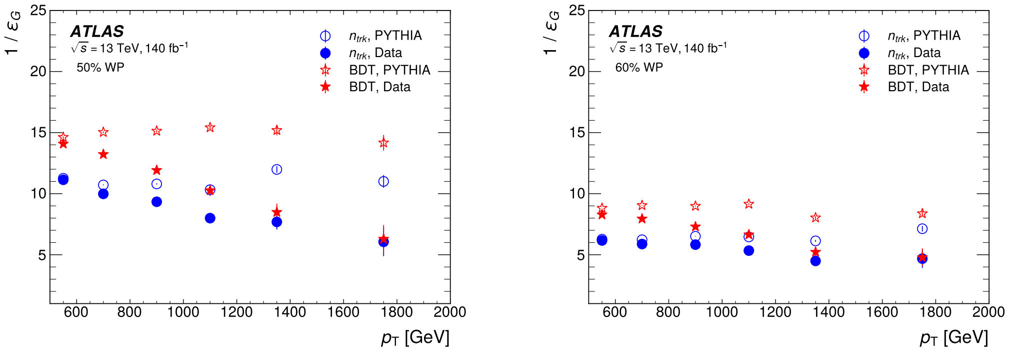

(a) Working Point:50% (b) Working Point:60%

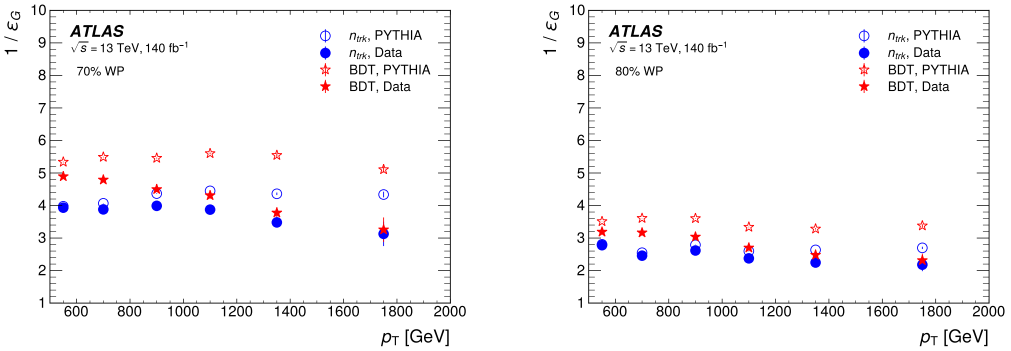

(c) Working Point:70% (d) Working Point:80%

Figure 5.33 Inverse of the gluon-jet efficiency of N_{trk} (circles) and BDT (stars) as a function of jet p_{T} at the each WP in data (closed symbols) and the PYTHIA (open symbols) MC. The vertical error bars show the statistical uncertainty.

5.7 Systematic uncertainties

In this study, different types of systematic uncertainty are taken into account. The distribution of N_{trk} and BDT for truth-labelled quark-/gluon-jets are given by the MC simulation samples, therefore, theoretical uncertainties originate from aspects encompassing the modelling of the MC simulation, such as choices involving parton showering, hadronisation, matrix element, PDFs, scale variations, and Splitting-Kernel effects. Furthermore, experimental uncertainties such as JES and JER, tracking reconstruction efficiencies are meticulously incorporated. The potential impact of methodological choices, including N_{trk} or BDT re-weighting, as well as the non-closure behaviour of MC simulations, is propagated to the resultant SFs.

The nominal result in this analysis is provided using PYTHIA 8 MC samples, all other MC samples are considered as alternative samples to study corresponding systematic uncertainty.

5.7.1 Parton shower modelling uncertainty

The different chose of algorithmic or parametric in the modelling of the parton shower could result in different SF result. This systematic uncertainty is estimated by comparing the SFs extracted from two MC samples with the same ME and hadronisation but different types of showers: HERWIG Angular-ordered and HERWIG Dipole samples. The corresponding fractions of quarks and gluons present in these two MC samples, are presented in Figure 5.34. The difference of extracted SFs between these two samples is less than 10% for quark signal efficiency and around 20% for gluon rejection efficiency. While the influence on quark scale factors is negligible, it takes on a dominant role in the context of gluon scale factors.

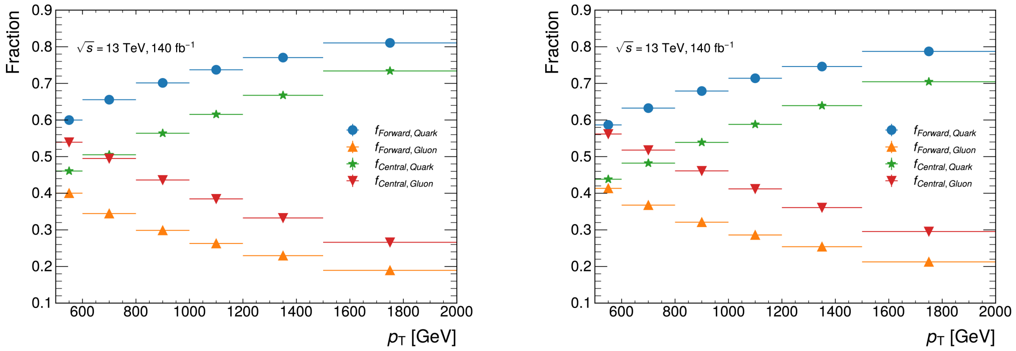

(a) HERWIG Angular

(b) HERWIG Dipole

Figure 5.34 Fractions of quark- gluon-jets of HERWIG angular (a) and HERWIG dipole (b) samples.

5.7.2 Hadronisation modelling uncertainty

The uncertainty from hadronisation modelling is given by the difference between the extracted SFs from the SHERPA MC samples with cluster-based hadronisation modelling and string-based hadronisation modelling, separately. The corresponding fractions of quarks and gluons present in these two MC samples are presented in Figure 5.35. The uncertainty on the SFs range from 1% to 8% for both jet types.

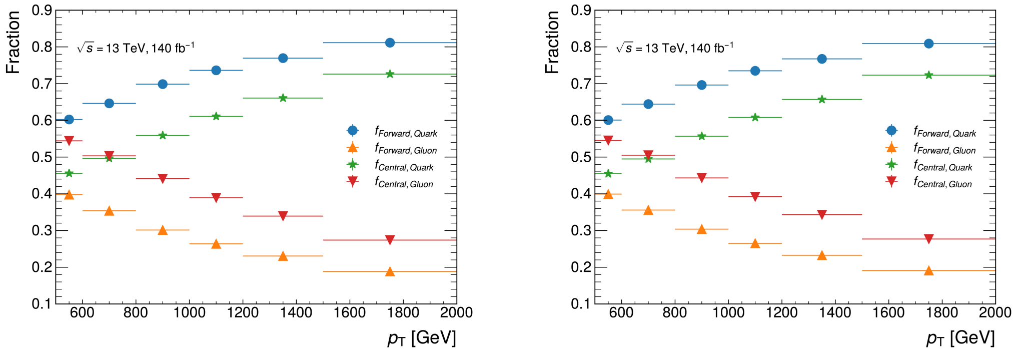

(a) SHERPA String-based

(b) SHERPA Cluster-based

Figure 5.35 Fractions of quark- and gluon-jets in each SHERPA sample.

5.7.3 Matrix element uncertainty

The uncertainty introduced by different types of ME in the MC samples is taken from the differences in the extracted SFs in two MC samples with different ME : POWHEG and PYTHIA . The corresponding fractions of quarks and gluons present in the POWHEG samples are presented in Figure 5.36.

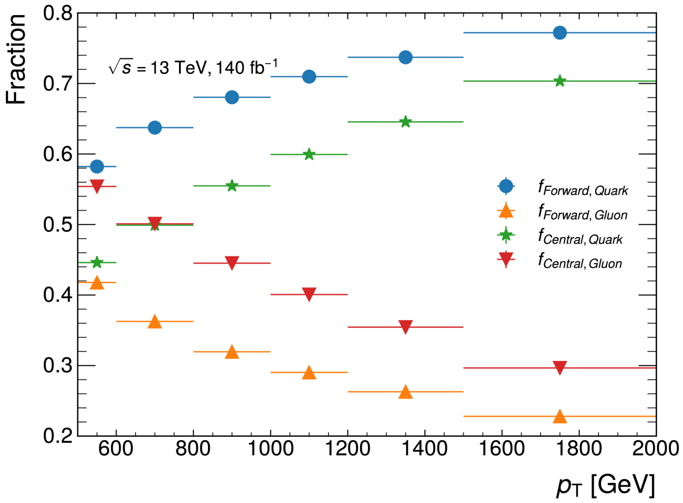

Figure 5.36 Fractions of quark jets and gluon jets in POWHEG samples.

5.7.4 PDF uncertainty

The uncertainty from the PDF set is evaluated using LHAPDF [70] package which provides the PDF internal variations for each PDF set, a NNPDF2.3 set is chosen to evaluate the various weights which depend on the momentum fraction. The PDF uncertainty is given by changing the nominal PDF weight to the systematic variation, then compare the SFs extracted from each of variations. The PDF uncertainty is around 5% - 7% level and almost negligible compared to others.

5.7.5 Scale variation uncertainty

The variation of the renormalisation (μ_R) and factorisation (μ_F) scales in QCD is used to evaluate the uncertainty caused by missing higher order corrections. The nominal PYTHIA sample is used for such estimation. In total there are 7 scale variations (μ_R, μ_F) in (2,2), (2,1), (1,1), (1,2), (1,0.5), (0.5,1), (0.5,0.5) studied in this analysis. The scale uncertainty is given by taking the maximum shift of the envelope with respect to the nominal one at each working points. The total scale uncertainty is around 4% - 7%.

5.7.6 Splitting-Kernel variation uncertainty

All formulations of shower processes are constructed on the fundamental foundation of the universal behaviour exhibited by singular infrared (soft and/or collinear) limits within QCD. Nonetheless, when one ventures beyond these limits into the physical phase space where these kernels are employed as approximations, there are in principle infinitely many different radiation functions to choose from, sharing the same singular terms but having different non-singular ones. The Splitting-Kernel variations [71] are variations of the non singular part of the splitting functions, for initial-state radiation and final-state radiation. Such uncertainty is less than 1%.

5.7.7 Tracking uncertainty

The number of associated tracks is the most important input for both taggers, with tracking-related systematics exerting an impact on the measurement of SFs. he uncertainty associated with reconstructed tracks is partitioned into two components: the uncertainty pertaining to track reconstruction efficiency and the MC fake rate [59]. Both sources of uncertainty are factored in to recalibrate the count of tracks associated with jets.

The track reconstruction efficiency uncertainty originates from material-related uncertainties, which constitutes the prevailing source, as well as from considerations related to the physics model. These uncertainties are estimated through a comparison of track efficiency across samples that encompass diverse detector modelling configurations. On the other hand, the MC fake rate is determined by contrasting the trends in a specific aspect of track multiplicity as a function of the average number of interactions per bunch crossing between empirical data and the MC simulation.The disparity in final SFs between the nominal value and the outcome of the systematic variation contributes to the tracking systematic uncertainty. This uncertainty spans a range of approximately 1% to 8%.

5.7.8 JES /JER uncertainty

The uncertainties associated with JES stem from the process of calibrating the transverse momentum balance between jets located in the central and forward regions, while also accommodating uncertainties linked to single-particle and test beam measurements. The JER uncertainties encompass the disparities between data and the MC. For each JES/JER variation, a corresponding SF is derived, and the difference between the nominal value and the variation is computed to determine the systematic uncertainty. The cumulative JES/JER uncertainty amounts to approximately 0.2%.

5.7.9 N_{trk} / BDT re-weighting

The quark-enriched and gluon-enriched regions are defined by comparing the η of leading and subleading jets, introduces to an η dependency from track reconstruction process. A re-weighting factor defined by Equation 5.8 is applied on N_{trk} and BDT taggers for each event to reduce the impact from different track multiplicity in different η range. The re-weighting factors acquired from truth-labelled gluon jets are regarded as an alternative source of contribution to the systematic uncertainty. It's worth noting that the differences arising from the re-weighting procedure remain comparatively minor (about 0.1% - 0.5%) in comparison to other sources of uncertainty.

The distributions of N_{trk} and BDT for extracted quark and gluon-jets after re-weighting with quark factor have been shown in the previous chapter. Figure 5.37, Figure 5.38 shows the distributions of extracted quark and gluon-jets after reweighting with gluon factor.

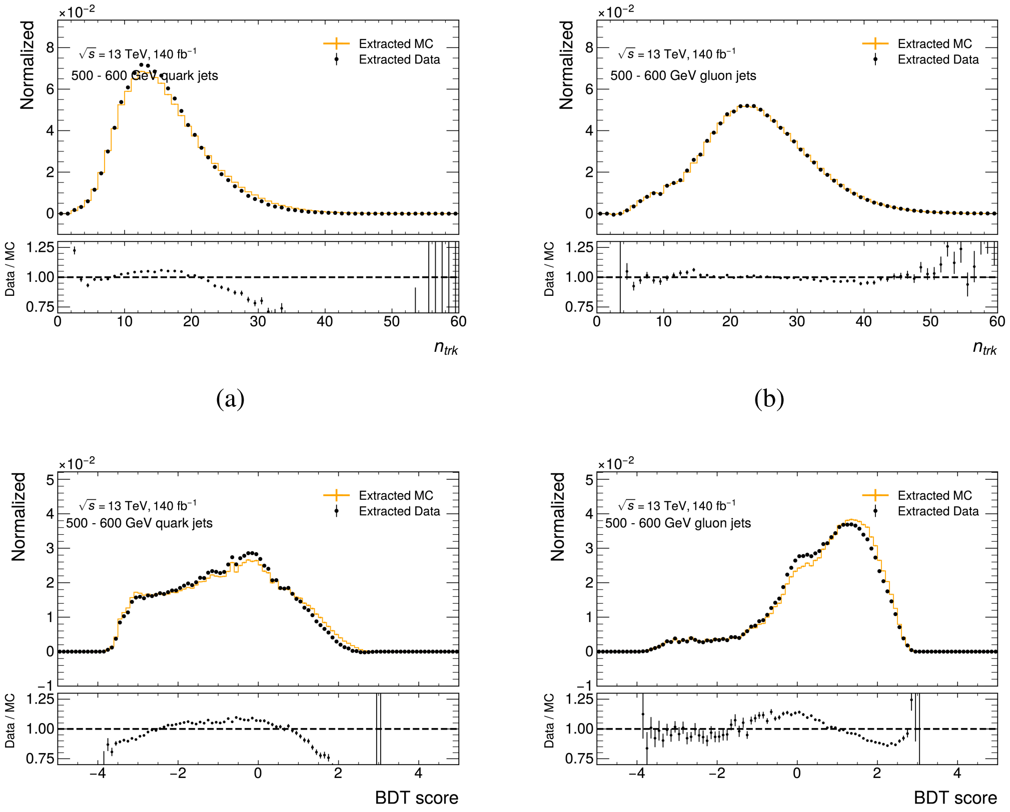

(a)

(b)

(c)

(d)

Figure 5.37 The N_{trk} (top) and BDT (bottom) distributions extracted by the matrix method from the data and MC of pure quark-jets (a) (c) and gluon-jets (b) (d) by PYTHIA 8. extracted by the matrix method from the data and MC. The gluon factor is applied. Solid-line histograms show the distributions of quark or gluon-jets defined by the jet parton flavour label in the MC. A bottom panel in each figure shows the ratio of the extracted data to the extracted MC by the matrix method.

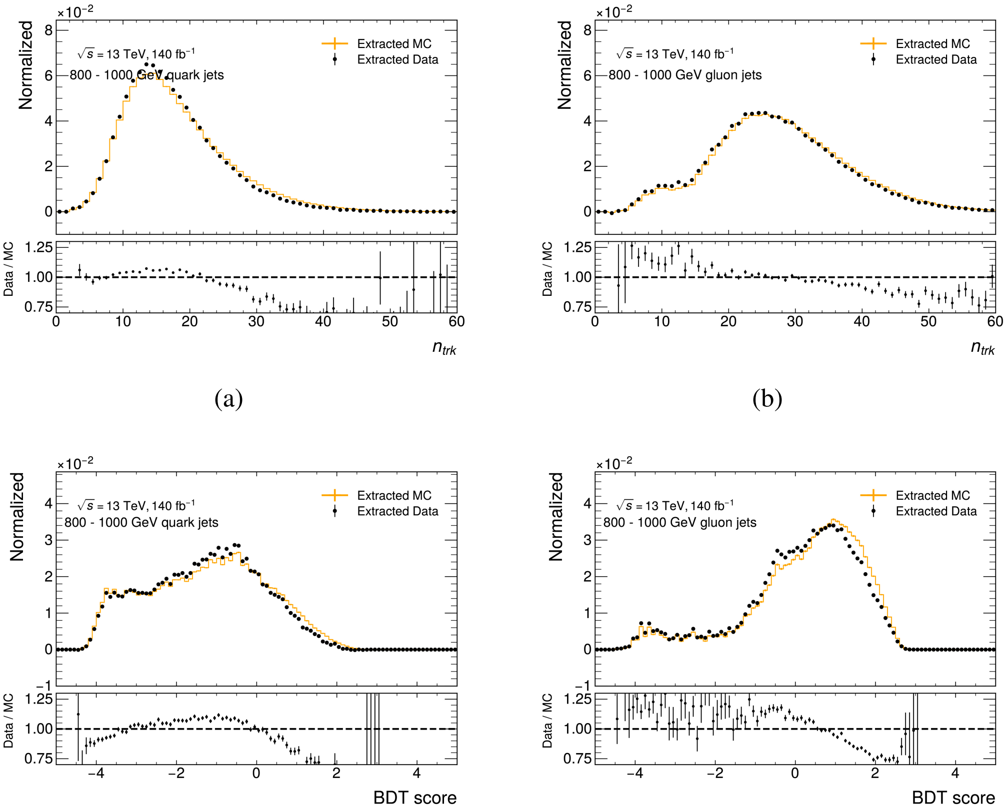

(a) (b)

(c) (d)

Figure 5.38 The N_{trk} (top) and BDT (bottom) distributions extracted by the matrix method from the data and MC of pure quark-jets (a) (c) and gluon-jets (b) (d) by PYTHIA 8. extracted by the matrix method from the data and MC.The gluon factor is applied. Solid-line histograms show the distributions of quark or gluon-jets defined by the jet parton flavour label in the MC. A bottom panel in each figure shows the ratio of the extracted data to the extracted MC by the matrix method.

5.7.10 The MC non-closure

As described in Section. 5.5, the MC closure test is conducted using MC samples wherein each jet is assigned a truth label. After re-weighting, the distributions of N_{trk} and BDT obtained through the matrix method exhibit consistency with the truth-labelled ones for quark- and gluon-jets, respectively. The remaining difference for both taggers is only 1% level.

5.7.11 Statistical uncertainty

The estimation of statistical uncertainty involves a stepwise process. It commences by varying the input data/MC distributions bin-by-bin, using Poisson/Gaussian distributions wherein the number of data events within each bin serves as the central value. These variations of the input histograms yield templates, subsequently employed as inputs for the template variations technique. This procedure is iterated 5000 times, with the standard deviation of these uncertainties of all toys taken is used to derive the statistical uncertainty of the SFs. This uncertainty is around 0.1%.

5.8 Results

Overall, both the N_{trk}-only tagger and the BDT-tagger exhibit commendable performance, and can effectively distinguish quark-jet from gluon-jet with high efficiency. The SFs for both quark- and gluon-jet fall within the range of approximately 0.9 to 1, indicating a reasonable agreement. The systematic uncertainty for quark-jet SFs hovers around 10%, while for gluon-jet SFs it's approximately 20%. Detailed of each uncertainty are shown in Section 5.7. The BDT-tagger showcases a slightly superior performance compared to the N_{trk} only tagger, i.e. higher gluon-jet rejection at the same WP.

The uncertainties of SF for each source of WP are estimated in each jet p_{T} range are given from Table 5.6 to Table 5.13 for quark-jets. Table 5.14 to Table 5.21 show the uncertainties of SF at each WP for gluon-jets. All systematics are ordered from largest to smallest in p_{T} range 500 - 600 GeV. the systematic uncertainties associated with quark-jet scale factors tend to be smaller than those linked to gluon-jet scale factors. Notably, for both quark- and gluon-jets, these uncertainties are primarily governed by the source of uncertainty stemming from parton showering.

Table 5.6 The quark scale factor (nominal) and the difference between the nominal and systematic variation results for 50% quark tag efficiency from N_{trk}tagger

	500-600	600-800	800-1000	1000-1200	1200-1500	1500-2000
nominal	1.02	1.04	1.04	1.03	1.02	1.01
scale variation	0.09	0.1	0.12	0.11	0.13	0.12
pdf weight	0.09	0.11	0.12	0.13	0.13	0.11
hadronization	0.09	0.07	0.06	0.05	0.04	0.04
tracking	0.08	0.07	0.06	0.05	0.05	0.04
matrix element	0.05	0.06	0.06	0.05	0.05	0.04
parton shower	0.02	0.03	0.05	0.06	0.07	0.08
MC nonclosure	0.02	0.04	0.04	0.03	0.02	0.01
splitting kernel	0.01	0.01	0.01	0.01	0.01	0.01
JES/JER	0.01	0.01	0.01	0.01	0.01	0.01
gluon reweight	0.01	0.01	0.01	0.01	0.01	0.01
Statistical	0.01	0.01	0.01	0.01	0.01	0.02
Total Uncertainty	0.19	0.19	0.21	0.21	0.22	0.19

Table 5.7 The quark scale factor (nominal) and the difference between the nominal and systematic variation results for 60% quark tag efficiency from N_{trk}tagger

	500-600	600-800	800-1000	1000-1200	1200-1500	1500-2000
nominal	1.03	1.04	1.04	1.03	1.01	1.01
pdf weight	0.09	0.1	0.12	0.12	0.12	0.1
tracking	0.08	0.07	0.06	0.05	0.05	0.04
scale variation	0.07	0.08	0.1	0.09	0.1	0.09
hadronization	0.06	0.05	0.04	0.04	0.03	0.03
matrix element	0.05	0.05	0.05	0.05	0.05	0.04
MC nonclosure	0.02	0.04	0.04	0.03	0.02	0.02
parton shower	0.02	0.03	0.03	0.04	0.06	0.08
splitting kernel	0.01	0.01	0.01	0.02	0.01	0.01
JES/JER	0.01	0.01	0.01	0.01	0.01	0.01
gluon reweight	0.01	0.01	0.01	0.01	0.01	0.01
Statistical	0.01	0.01	0.01	0.01	0.01	0.01
Total Uncertainty	0.16	0.17	0.18	0.18	0.18	0.17

Table 5.8 The quark scale factor (nominal) and the difference between the nominal and systematic variation results for 70% quark tag efficiency from N_{trk}tagger

	500-600	600-800	800-1000	1000-1200	1200-1500	1500-2000
nominal	1.03	1.04	1.04	1.03	1.02	1.0
pdf weight	0.08	0.09	0.11	0.11	0.11	0.08
tracking	0.07	0.06	0.05	0.05	0.04	0.03
scale variation	0.06	0.06	0.07	0.07	0.07	0.06
hadronization	0.05	0.04	0.04	0.03	0.03	0.02
matrix element	0.04	0.05	0.04	0.04	0.04	0.03
MC nonclosure	0.03	0.04	0.04	0.04	0.02	0.01
parton shower	0.02	0.02	0.02	0.03	0.04	0.05
splitting kernel	0.01	0.01	0.01	0.02	0.02	0.01
JES/JER	0.01	0.01	0.01	0.01	0.01	0.01
gluon reweight	0.01	0.01	0.01	0.01	0.01	0.01
Statistical	0.01	0.01	0.01	0.01	0.01	0.01
Total Uncertainty	0.14	0.14	0.16	0.16	0.15	0.13

Table 5.9 The quark scale factor (nominal) and the difference between the nominal and systematic variation results for 80% quark tag efficiency from N_{trk}tagger

	500-600	600-800	800-1000	1000-1200	1200-1500	1500-2000
nominal	1.03	1.03	1.03	1.02	1.01	1.0
tracking	0.06	0.05	0.05	0.04	0.03	0.02
pdf weight	0.06	0.07	0.09	0.09	0.08	0.06
scale variation	0.03	0.04	0.05	0.04	0.04	0.05
MC nonclosure	0.03	0.04	0.04	0.03	0.02	0.01
hadronization	0.03	0.02	0.02	0.02	0.02	0.02
matrix element	0.03	0.04	0.03	0.03	0.03	0.02
parton shower	0.01	0.01	0.02	0.01	0.02	0.03
splitting kernel	0.01	0.01	0.01	0.02	0.02	0.01
JES/JER	0.01	0.01	0.01	0.01	0.01	0.01
gluon reweight	0.01	0.01	0.01	0.01	0.01	0.01
Statistical	0.01	0.01	0.01	0.01	0.01	0.01
Total Uncertainty	0.11	0.11	0.13	0.12	0.11	0.1

Table 5.10 The quark scale factor (nominal) and the difference between the nominal and systematic variation results for 50% quark tag efficiency from BDT tagger

	500-600	600-800	800-1000	1000-1200	1200-1500	1500-2000
nominal	1.01	1.02	1.03	1.02	1.01	1.0
pdf weight	0.09	0.1	0.12	0.13	0.12	0.1
scale variation	0.09	0.1	0.12	0.12	0.13	0.1
hadronization	0.07	0.06	0.06	0.06	0.04	0.04
matrix element	0.05	0.06	0.06	0.05	0.05	0.04
tracking	0.05	0.05	0.05	0.04	0.04	0.04
MC nonclosure	0.01	0.01	0.02	0.01	0.01	0.01
parton shower	0.01	0.01	0.03	0.04	0.05	0.07
splitting kernel	0.01	0.01	0.01	0.01	0.02	0.01
gluon reweight	0.01	0.01	0.01	0.01	0.01	0.01
JES/JER	0.01	0.01	0.01	0.01	0.01	0.01
Statistical	0.01	0.01	0.01	0.01	0.01	0.02
Total Uncertainty	0.17	0.18	0.2	0.2	0.2	0.18

Table 5.11 The quark scale factor (nominal) and the difference between the nominal and systematic variation results for 60% quark tag efficiency from BDT tagger

	500-600	600-800	800-1000	1000-1200	1200-1500	1500-2000
nominal	1.02	1.03	1.04	1.03	1.02	1.01
pdf weight	0.09	0.1	0.11	0.12	0.12	0.1
scale variation	0.07	0.08	0.1	0.1	0.11	0.08
hadronization	0.06	0.05	0.05	0.05	0.03	0.04
tracking	0.05	0.05	0.05	0.04	0.04	0.04
matrix element	0.05	0.05	0.05	0.05	0.04	0.03
splitting kernel	0.01	0.01	0.01	0.01	0.02	0.01
gluon reweight	0.01	0.01	0.01	0.01	0.01	0.01
MC nonclosure	0.01	0.02	0.02	0.02	0.01	0.01
JES/JER	0.01	0.01	0.01	0.01	0.01	0.01
Statistical	0.01	0.01	0.01	0.01	0.01	0.01
parton shower	0.01	0.01	0.03	0.03	0.05	0.06
Total Uncertainty	0.15	0.16	0.18	0.18	0.18	0.15

Table 5.12 The quark scale factor (nominal) and the difference between the nominal and systematic variation results for 70% quark tag efficiency from BDT tagger

	500-600	600-800	800-1000	1000-1200	1200-1500	1500-2000
nominal	1.03	1.04	1.04	1.03	1.02	1.02
pdf weight	0.08	0.09	0.1	0.11	0.1	0.08
scale variation	0.06	0.06	0.08	0.08	0.08	0.06
tracking	0.06	0.05	0.05	0.05	0.04	0.04
hadronization	0.05	0.04	0.04	0.04	0.03	0.03
matrix element	0.04	0.04	0.04	0.04	0.03	0.02
splitting kernel	0.01	0.01	0.01	0.02	0.01	0.01
parton shower	0.01	0.01	0.02	0.03	0.04	0.04
gluon reweight	0.01	0.01	0.01	0.01	0.01	0.01
JES/JER	0.01	0.01	0.01	0.01	0.01	0.01
MC nonclosure	0.01	0.02	0.03	0.02	0.01	0.01
Statistical	0.01	0.01	0.01	0.01	0.01	0.01
Total Uncertainty	0.13	0.13	0.15	0.15	0.15	0.12

Table 5.13 The quark scale factor (nominal) and the difference between the nominal and systematic variation results for 80% quark tag efficiency from BDT tagger

	500-600	600-800	800-1000	1000-1200	1200-1500	1500-2000
nominal	1.03	1.04	1.04	1.03	1.02	1.01
pdf weight	0.07	0.07	0.08	0.09	0.08	0.06
tracking	0.06	0.05	0.05	0.04	0.03	0.03
scale variation	0.04	0.05	0.06	0.06	0.05	0.05
hadronization	0.04	0.03	0.03	0.02	0.02	0.02
matrix element	0.03	0.04	0.03	0.03	0.02	0.02
splitting kernel	0.01	0.01	0.02	0.02	0.02	0.01
parton shower	0.01	0.01	0.02	0.02	0.02	0.03
gluon reweight	0.01	0.01	0.01	0.01	0.01	0.01
JES/JER	0.01	0.01	0.01	0.01	0.01	0.01
MC nonclosure	0.01	0.01	0.02	0.02	0.01	0.01
Statistical	0.01	0.01	0.01	0.01	0.01	0.01
Total Uncertainty	0.11	0.11	0.12	0.12	0.11	0.1

Table 5.14 The gluon scale factor (nominal) and the difference between the nominal and systematic variation results for 50% gluon tag efficiency from N_{trk}tagger

	500-600	600-800	800-1000	1000-1200	1200-1500	1500-2000
nominal	0.99	0.98	0.98	0.96	0.94	0.92
parton shower	0.1	0.11	0.12	0.13	0.11	0.14
pdf weight	0.04	0.05	0.05	0.06	0.06	0.05
splitting kernel	0.02	0.01	0.01	0.01	0.01	0.01
tracking	0.01	0.02	0.02	0.02	0.02	0.01
hadronization	0.01	0.01	0.01	0.01	0.01	0.01
scale variation	0.01	0.01	0.01	0.01	0.01	0.01
MC nonclosure	0.01	0.01	0.02	0.04	0.06	0.07
matrix element	0.01	0.01	0.02	0.03	0.04	0.07
JES/JER	0.01	0.01	0.01	0.01	0.01	0.01
Statistical	0.01	0.01	0.01	0.01	0.01	0.02
gluon reweight	0.01	0.01	0.01	0.01	0.01	0.01
Total Uncertainty	0.11	0.12	0.13	0.15	0.15	0.18

Table 5.15 The gluon scale factor (nominal) and the difference between the nominal and systematic variation results for 60% gluon tag efficiency from N_{trk}tagger

	500-600	600-800	800-1000	1000-1200	1200-1500	1500-2000
nominal	0.99	0.98	0.97	0.95	0.92	0.91
parton shower	0.15	0.17	0.17	0.17	0.17	0.21
pdf weight	0.05	0.06	0.06	0.07	0.07	0.06
splitting kernel	0.03	0.01	0.01	0.01	0.01	0.02
scale variation	0.02	0.03	0.02	0.02	0.02	0.03
tracking	0.02	0.02	0.02	0.02	0.02	0.01
hadronization	0.01	0.01	0.01	0.01	0.01	0.01
MC nonclosure	0.01	0.02	0.02	0.04	0.07	0.08
matrix element	0.01	0.01	0.02	0.03	0.05	0.08
JES/JER	0.01	0.01	0.01	0.01	0.01	0.01
Statistical	0.01	0.01	0.01	0.01	0.01	0.03
gluon reweight	0.01	0.01	0.01	0.01	0.01	0.01
Total Uncertainty	0.17	0.18	0.18	0.2	0.2	0.25

Table 5.16 The gluon scale factor (nominal) and the difference between the nominal and systematic variation results for 70% gluon tag efficiency from N_{trk}tagger

	500-600	600-800	800-1000	1000-1200	1200-1500	1500-2000
nominal	0.99	0.97	0.96	0.94	0.91	0.87
parton shower	0.21	0.22	0.23	0.24	0.25	0.31
pdf weight	0.06	0.06	0.07	0.08	0.08	0.07
splitting kernel	0.04	0.01	0.01	0.01	0.01	0.01
scale variation	0.04	0.04	0.03	0.04	0.03	0.04
tracking	0.02	0.02	0.02	0.02	0.01	0.01
hadronization	0.01	0.01	0.01	0.01	0.01	0.01
MC nonclosure	0.01	0.02	0.03	0.05	0.08	0.12
matrix element	0.01	0.01	0.02	0.03	0.06	0.09
JES/JER	0.01	0.01	0.01	0.01	0.01	0.01
gluon reweight	0.01	0.01	0.01	0.01	0.01	0.01
Statistical	0.01	0.01	0.01	0.01	0.01	0.03
Total Uncertainty	0.23	0.24	0.24	0.26	0.28	0.35

Table 5.17 The gluon scale factor (nominal) and the difference between the nominal and systematic variation results for 80% gluon tag efficiency from N_{trk}tagger

	500-600	600-800	800-1000	1000-1200	1200-1500	1500-2000
nominal	0.98	0.97	0.95	0.93	0.89	0.85
parton shower	0.32	0.31	0.33	0.37	0.37	0.45
scale variation	0.07	0.07	0.05	0.07	0.07	0.05
splitting kernel	0.07	0.02	0.02	0.03	0.01	0.02
pdf weight	0.06	0.07	0.07	0.09	0.09	0.08
tracking	0.01	0.01	0.01	0.01	0.01	0.01
MC nonclosure	0.01	0.03	0.04	0.06	0.1	0.15
matrix element	0.01	0.01	0.02	0.04	0.07	0.11
hadronization	0.01	0.01	0.01	0.01	0.01	0.01
JES/JER	0.01	0.01	0.01	0.01	0.01	0.01
gluon reweight	0.01	0.01	0.01	0.01	0.01	0.01
Statistical	0.01	0.01	0.01	0.01	0.01	0.03
Total Uncertainty	0.34	0.33	0.34	0.39	0.41	0.49

Table 5.18 The gluon scale factor (nominal) and the difference between the nominal and systematic variation results for 50% gluon tag efficiency from BDT tagger

	500-600	600-800	800-1000	1000-1200	1200-1500	1500-2000
nominal	1.0	0.99	0.98	0.96	0.94	0.92
parton shower	0.09	0.08	0.1	0.1	0.1	0.13
pdf weight	0.04	0.04	0.05	0.05	0.06	0.04
splitting kernel	0.03	0.02	0.02	0.02	0.01	0.02
scale variation	0.01	0.01	0.01	0.01	0.01	0.03
MC nonclosure	0.01	0.02	0.03	0.05	0.06	0.09
hadronization	0.01	0.01	0.01	0.01	0.01	0.01
tracking	0.01	0.01	0.01	0.01	0.01	0.01
matrix element	0.01	0.01	0.02	0.02	0.04	0.07
gluon reweight	0.01	0.01	0.01	0.01	0.01	0.01
JES/JER	0.01	0.01	0.01	0.01	0.01	0.01
Statistical	0.01	0.01	0.01	0.01	0.01	0.02
Total Uncertainty	0.11	0.1	0.11	0.13	0.14	0.18

Table 5.19 The gluon scale factor (nominal) and the difference between the nominal and systematic variation results for 60% gluon tag efficiency from BDT tagger

	500-600	600-800	800-1000	1000-1200	1200-1500	1500-2000
nominal	0.99	0.98	0.97	0.95	0.93	0.91
parton shower	0.11	0.12	0.13	0.13	0.14	0.17
pdf weight	0.05	0.05	0.05	0.06	0.06	0.06
splitting kernel	0.05	0.03	0.03	0.03	0.01	0.04
MC nonclosure	0.02	0.03	0.04	0.06	0.08	0.1
scale variation	0.02	0.02	0.02	0.02	0.02	0.05
hadronization	0.01	0.01	0.01	0.01	0.02	0.01
tracking	0.01	0.01	0.01	0.01	0.01	0.01
matrix element	0.01	0.01	0.02	0.03	0.04	0.08
gluon reweight	0.01	0.01	0.01	0.01	0.01	0.01
JES/JER	0.01	0.01	0.01	0.01	0.01	0.01
Statistical	0.01	0.01	0.01	0.01	0.01	0.02
Total Uncertainty	0.13	0.14	0.15	0.16	0.18	0.23

Table 5.20 The gluon scale factor (nominal) and the difference between the nominal and systematic variation results for 70% gluon tag efficiency from BDT tagger

	500-600	600-800	800-1000	1000-1200	1200-1500	1500-2000
nominal	0.98	0.97	0.95	0.93	0.89	0.86
parton shower	0.15	0.15	0.17	0.17	0.17	0.21
splitting kernel	0.07	0.05	0.05	0.04	0.03	0.05
pdf weight	0.05	0.06	0.06	0.07	0.07	0.06
MC nonclosure	0.05	0.05	0.07	0.09	0.12	0.15
scale variation	0.03	0.04	0.03	0.04	0.04	0.07
hadronization	0.02	0.01	0.01	0.01	0.01	0.01
tracking	0.01	0.01	0.01	0.01	0.01	0.01
matrix element	0.01	0.01	0.02	0.03	0.05	0.08
JES/JER	0.01	0.01	0.01	0.01	0.01	0.01
gluon reweight	0.01	0.01	0.01	0.01	0.01	0.01
Statistical	0.01	0.01	0.01	0.01	0.01	0.02
Total Uncertainty	0.18	0.18	0.2	0.21	0.23	0.29

Table 5.21 The gluon scale factor (nominal) and the difference between the nominal and systematic variation results for 80% gluon tag efficiency from BDT tagger

	500-600	600-800	800-1000	1000-1200	1200-1500	1500-2000
nominal	0.96	0.95	0.93	0.9	0.85	0.81
parton shower	0.19	0.18	0.21	0.2	0.22	0.28
splitting kernel	0.09	0.07	0.06	0.06	0.05	0.07
MC nonclosure	0.08	0.09	0.1	0.12	0.17	0.21
pdf weight	0.06	0.06	0.07	0.08	0.08	0.06
scale variation	0.05	0.05	0.05	0.05	0.07	0.08
hadronization	0.02	0.01	0.01	0.01	0.01	0.01
tracking	0.01	0.01	0.01	0.01	0.01	0.01
matrix element	0.01	0.01	0.02	0.03	0.06	0.09
JES/JER	0.01	0.01	0.01	0.01	0.01	0.01
Statistical	0.01	0.01	0.01	0.01	0.01	0.03
gluon reweight	0.01	0.01	0.01	0.01	0.01	0.02
Total Uncertainty	0.23	0.23	0.25	0.26	0.31	0.38

Figure 5.39 to Figure 5.42 show the leading uncertainties with SFs for both tagger. The SFs for quark-jets and gluon-jets corresponding to the 50% quark-jets efficiency working point (WP) fall within the range of 0.92 to 1.02, while being subject to an aggregate systematic uncertainty of approximately 20%. Among the various sources of systematic uncertainty, theoretical modelling emerges as the dominant factor contributing to the total uncertainty.

To ascertain the robustness of the findings, tests are conducted to assess the stability of results across different regions of jet $|\eta|$. The SF measurements are recomputed through the normalization of jet $|\eta|$ in the quark-/gluon-enriched subsamples. The alternate results obtained in this manner are determined to be consistent with the nominal outcome, falling within the full range of reported uncertainties.

Given the variations in the usage of different MC samples, a MC-to-MC SF is computed. This involves employing each alternative MC sample while treating the PYTHIA MC samples as pseudodata. This approach accommodates discrepancies arising from modelling difference between the PYTHIA and alternative MC samples. The MC-to-MC SFs for both jet taggers at each WP are shown in Figure 5.43 to Figure 5.46. Notably, there exists a large difference in gluon modelling between the HERWIG Dipole parton shower MC and the PYTHIA MC. This discrepancy is reflected in the relatively significant MC-to-MC SF, indicating substantial differences between these models.

The $/g$ taggers presented in this article, along with the measurement of their SFs, will enhance a variety of analyses. This includes SM measurements that depend on accurately determining jet origins, as well as searches for new physics, where their application will heighten sensitivity to potential new particles.

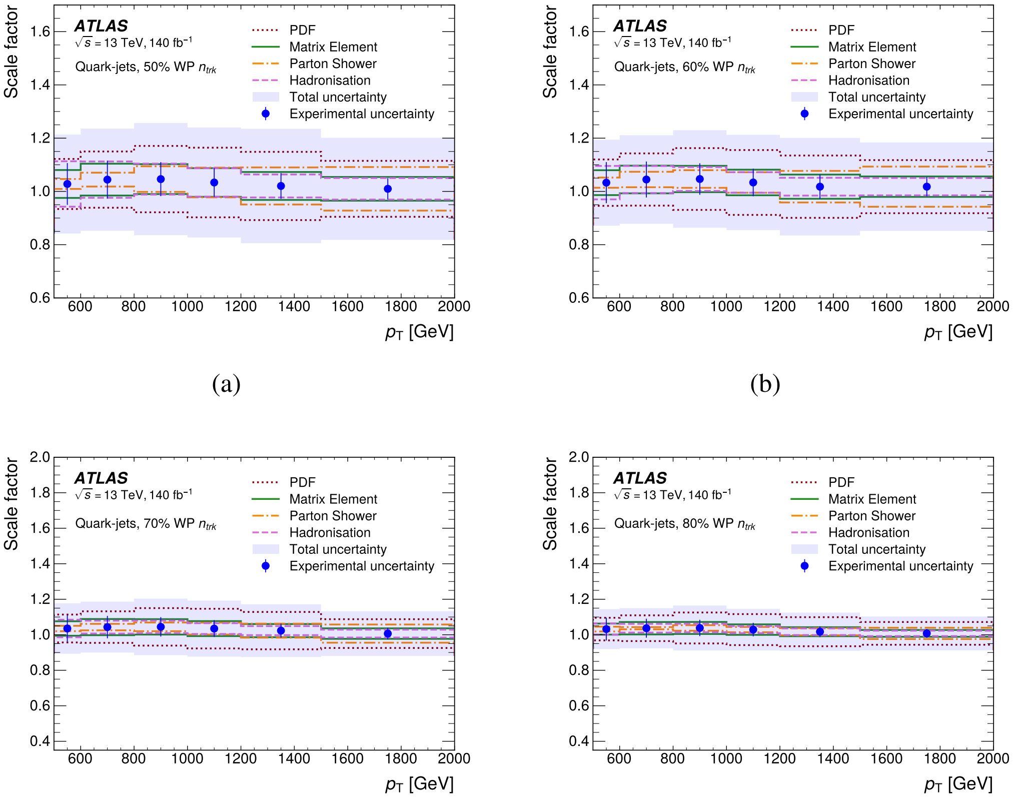

(a) (b)

(c) (d)

Figure 5.39 The SF with total and leading systematic uncertainty on the jet tagging variable N_{trk} obtained by PYTHIA 8 MCs as a function of jet p_T for quark-jets at each WP.

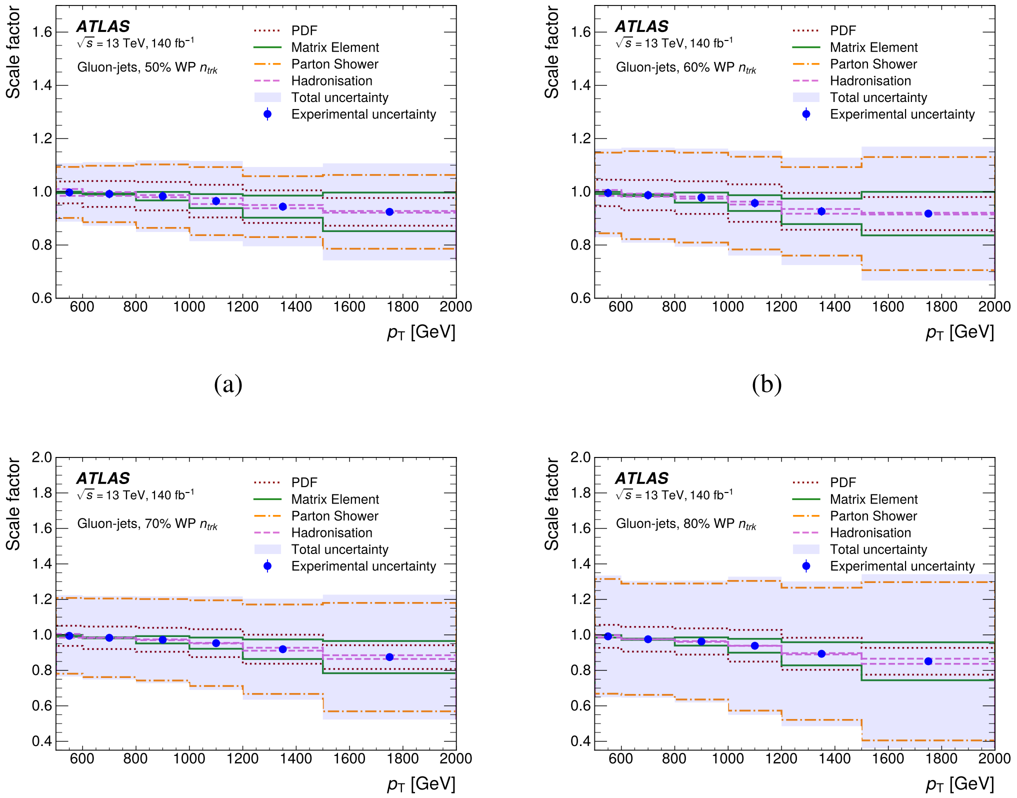

(a) (b)

(c) (d)

Figure 5.40 The SF with total and leading systematic uncertainty on the jet tagging variable N_{trk} obtained by PYTHIA 8 MCs as a function of jet p_T for gluon-jets at each WP.

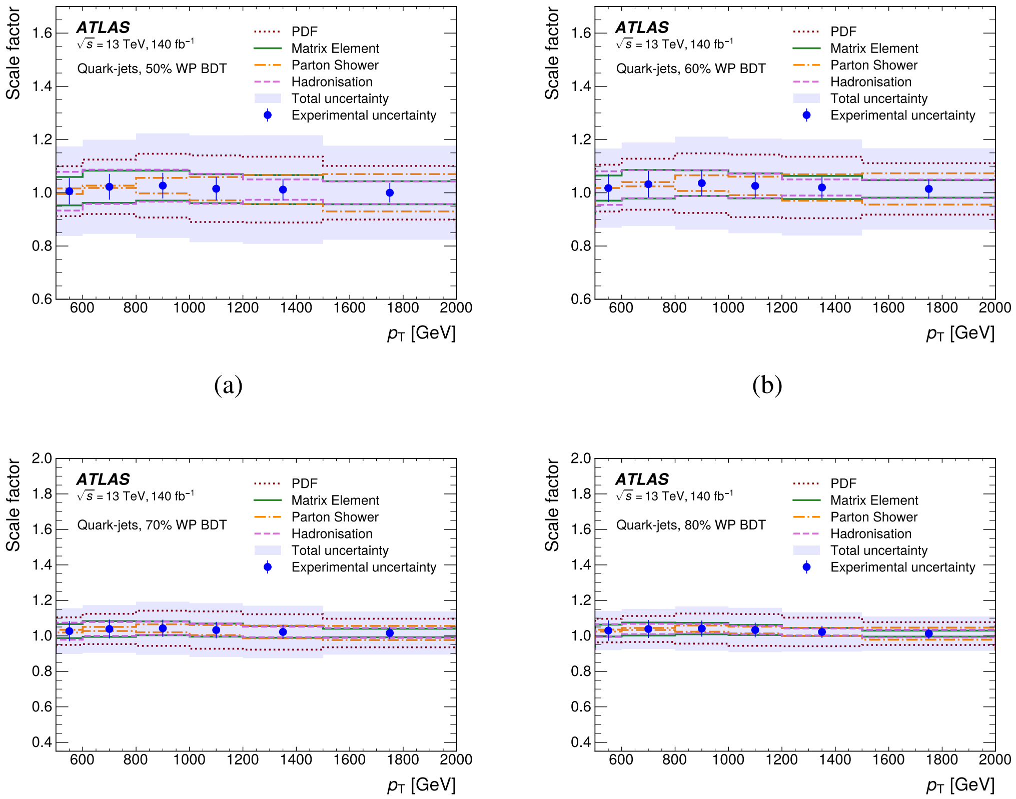

(a)

(b)

(c)

(d)

Figure 5.41 The SF with total and leading systematic uncertainty on the jet tagging variable BDT obtained by Pythia 8 MCs as a function of jet p_T for quark-jets at each WP.

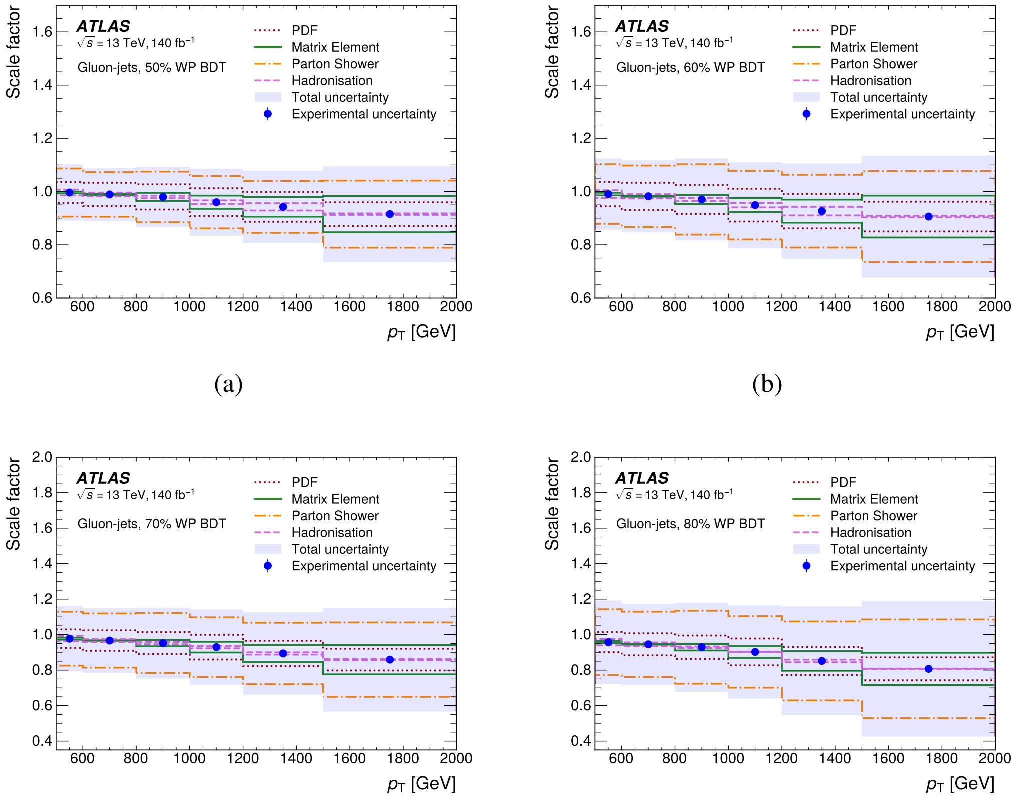

(a) (b)

(c) (d)

Figure 5.42 The SF with total and leading systematic uncertainty on the jet tagging variable BDT obtained by PYTHIA 8 MCs as a function of jet p_T for gluon-jets at each WP.

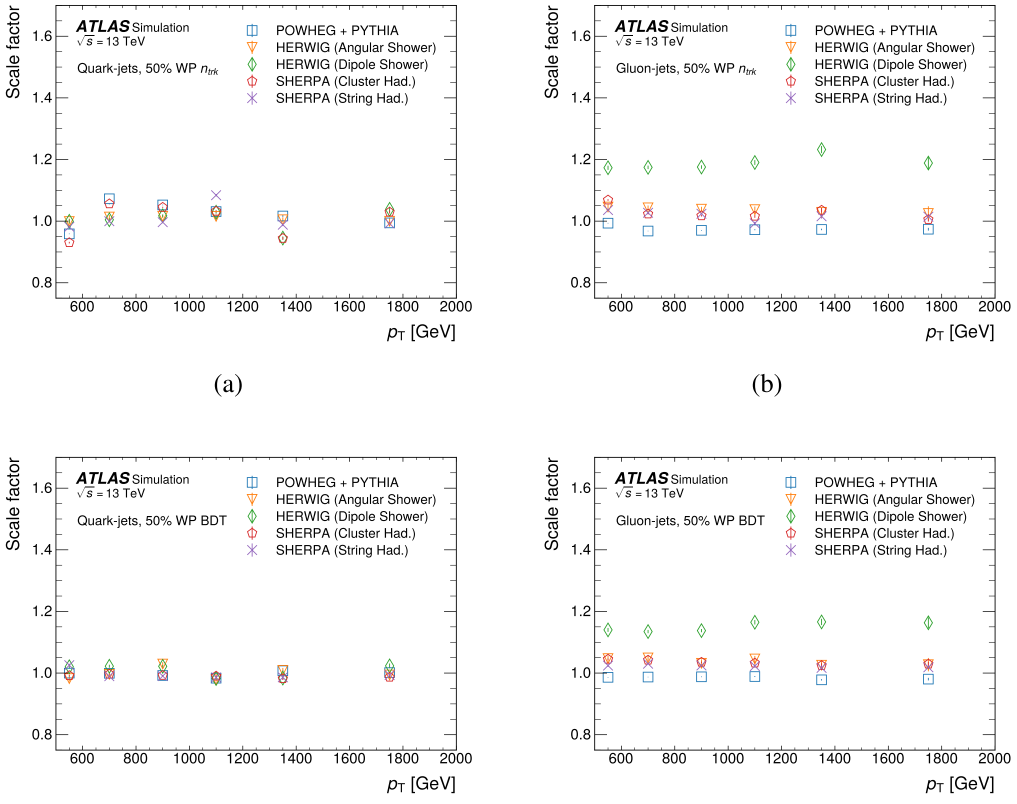

(a) (b)

(c) (d)

Figure 5.43 The MC-to-MC SF of the N_{trk}, (a) and (b), and BDT, (c) and (d), as a function of jet p_T for quark-jets (left) and gluon-jets (right) at the 50% WP. The vertical error bars show the statistical uncertainty.

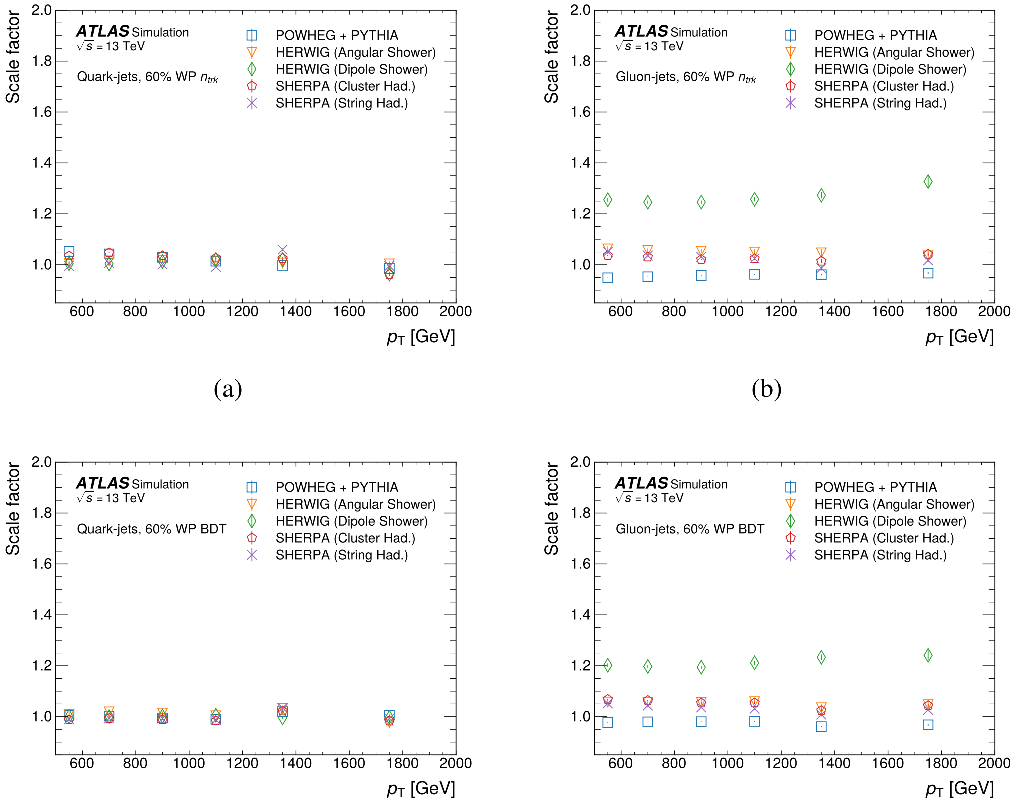

(a) (b)

(c) (d)

Figure 5.44 The MC-to-MC SF of the N_{trk}, (a) and (b), and BDT, (c) and (d), as a function of jet p_T for quark-jets (left) and gluon-jets (right) at the 60% WP. The vertical error bars show the statistical uncertainty.

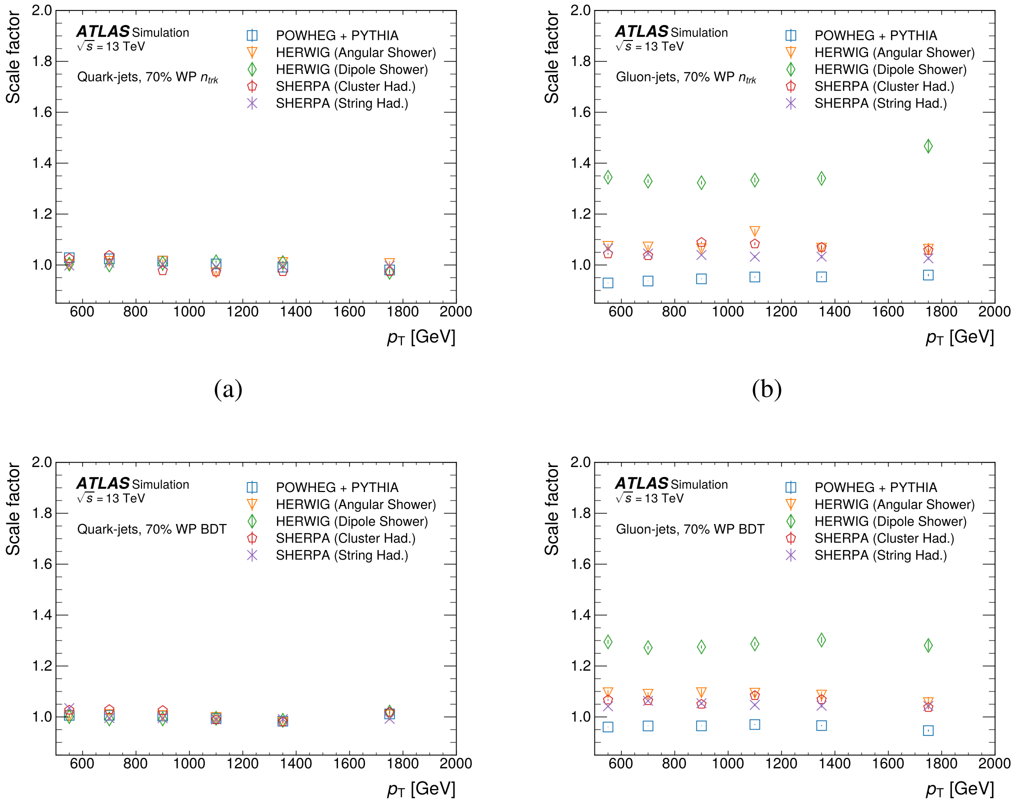

(a) (b)

(c) (d)

Figure 5.45 The MC-to-MC SF of the N_{trk}, (a) and (b), and BDT, (c) and (d), as a function of jet p_T for quark-jets (left) and gluon-jets (right) at the 70% WP. The vertical error bars show the statistical uncertainty.

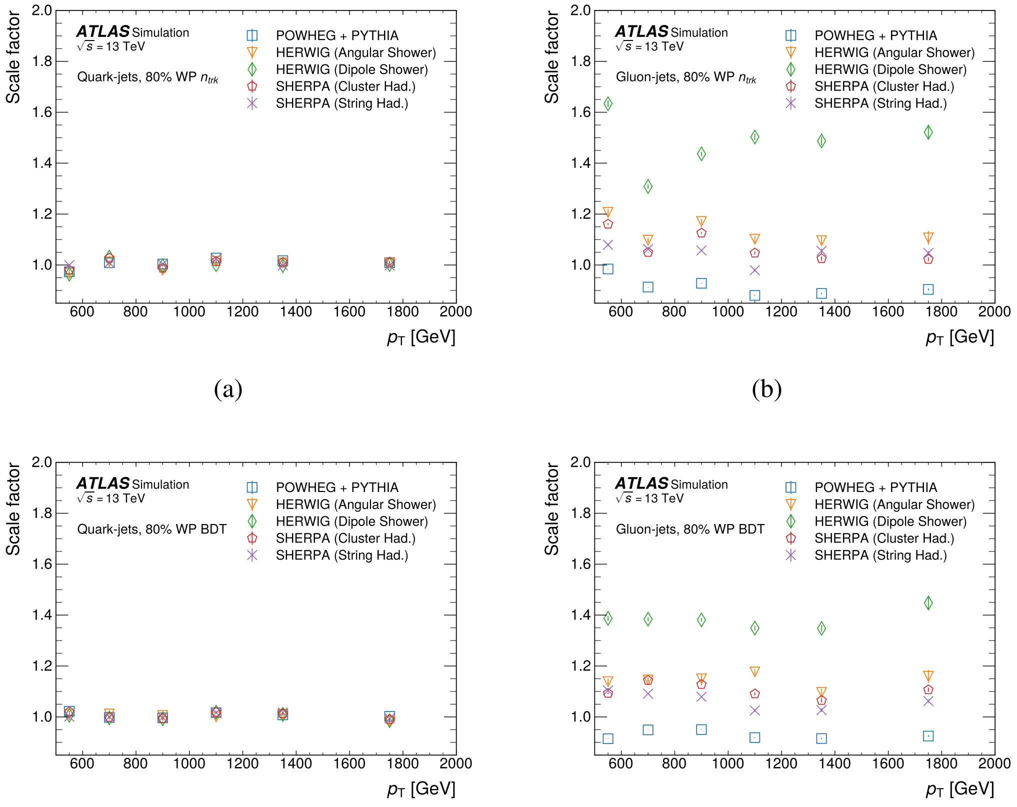

(a) (b)

(c) (d)

Figure 5.46 The MC-to-MC SF of the N_{trk}, (a) and (b), and BDT, (c) and (d), as a function of jet p_T for quark-jets (left) and gluon-jets (right) at the 80% WP. The vertical error bars show the statistical uncertainty.

6 Search for new phenomena in dijet events

As described in Section 2, the heavy resonance predicted by many BSM play a key role in understanding many fundamental phenomena. The narrow heavy resonance which decays into two gluons final state at the LHC, appears to be two hadronic jets in the detector. Produced by the QCD processes, the dijet events have a smoothly falling distribution of the invariant mass m_{jj} , whereas two jets appear to be a resonance in the m_{jj} spectrum. As a result, searches for dijet resonance are one of the flagship exotics analyses in ATLAS.

Besides, on the assumption that the resonant sample can be classified according to the type of parton that initiated the jets, the sensitivity of searches for new resonance can be improved by identifying the types of partons through which the potentially new particle interact. One of simplest examples of such tagging is gluon-tagging one or more of the jets. The jet tagging procedure based on the number of charged tracks with transverse momentum p_{T} above 500 GeV is described in Section. 5. The m_{jj} spectrum of background is estimated from the data, which is used for the search in three categories: inclusive, single-gluon, and double-gluon tagged dijet systems. The inclusive m_{jj} spectrum is thus considered as control region for quark/gluon studies.

This chapter describes searches for new heavy particles decay in dijet final state as originating from gluons or quarks, a technique of quark/gluon tagging is employed to enhance the sensitivity to the results. The search performed uses full Run 2 data at $\sqrt{s} = 13$ TeV, with higher integrated luminosity compared to previous one (Run 1), significantly improvements in the understanding of systematic uncertainties are expected. On the other hand, cross section upper limits will be set if no significantly resonances are observed.

The simplified procedures in this analysis is performed as following:

- Search for high-mass resonances in the untagged (inclusive), single-gluon tagged, and two-gluon tagged categories with dijet events.
- If significant resonances are found, claim something interesting, else the upper limits are set.
- Model independent upper-limits are set on resonance cross sections in inclusive, single-gluon tagged, and two-gluon tagged categories.

- For the specific resonance model, set lower limits on the relevant scales in inclusive, single-gluon tagged, and two-gluon tagged categories.

6.1 Monte Carlo models

. This section outlines benchmark models for both background from the QCD and for new physics signals that encapsulated in the models chosen: Strings, graviton and QBH. Full Run 2 data are used to produce EXOT2 skimmed samples used in this analysis [72].

6.1.1 QCD background

QCD processes from the MC are simulated at LO and NLO in SM perturbative theory. Due to the large range in cross section of QCD sample [73], the samples are thus sliced based on the leading jet p_{T}, to obtain comparable statistical precision across the jet p_{T} range of interest.

6.1.2 Kaluza-Klein Graviton

For the RS1 KK spin-2 graviton samples considered in this study, we focus on $k/\overline{M}_{Pl} = 0.2$. These samples encompass both gluon-gluon and quark-quark initial states, with decays exclusively to gluons or bottom quarks.

The signal templates for the KK gravitons are generated with different mass values using the PYTHIA 8 event generator. These simulations utilize the A14 tune and NNPDF2.3 PDF set.

Figure 6.47 shows the Graviton to gg invariant mass distribution for the considered mass points.

6.1.3 Quantum Black Hole

In our study, we employ the QBH model for the purpose of comparing limits with the previous iteration of the analysis. The feasibility of producing QBHs at the LHC is contingent upon the presence of sufficiently large extra dimensions within the universe [74]. This model posits that the energy scale of quantum gravity M_D, at which QBHs are generated, diminishes as the number of these large extra dimensions, denoted

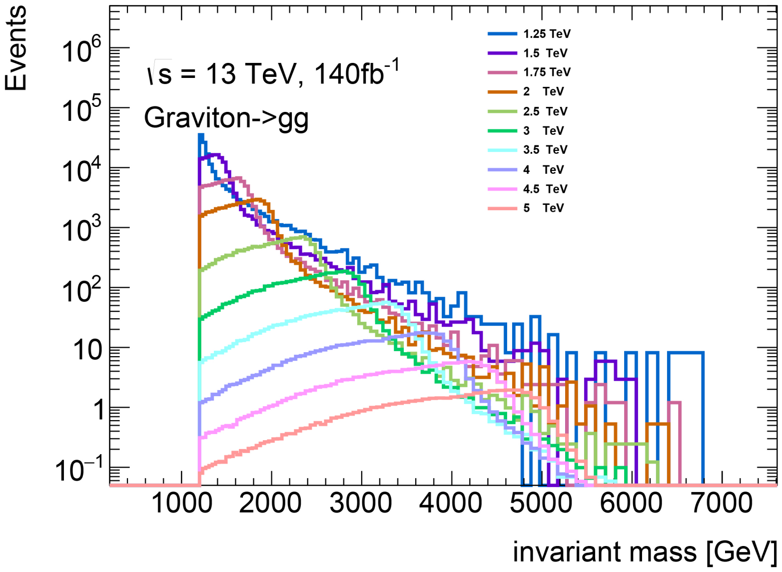

Figure 6.47 (a) Invariant mass distribution for the Graviton to gg samples

as n, increases. Consequently, a larger n permits lower mass scales at which QBHs can be formed.

Two-body isotropic final state is expected by the QBH decay at the LHC, where the M_D energy threshold could be reached [75]. Therefore the quantum gravitational effects can be probed by searches on m_{jj} spectrum. To simulate events involving quantum black holes with $n = 6$, we utilize the BlackMax [76] MC generator. This MC generator facilitates the simulation of QBH events within the $n = 6$ framework。

6.1.4 Gaussian resonances

A model-independent signal as Gaussian [77] are used to expand the sensitivity of the search to new signals that may be detectable with this analysis but not currently theoretically described. Besides, a model-independent signal could help to evaluate and compare the strength of different analyses without bias, as the case where specific models are applied and leads less sensitive to the search.

Therefore, model-independent fit function tests are produced based on model-independent signal resonances. Because this analysis is sensitive to the shape of resonance, specific models with different shapes would influence the results strongly. In general, a model-independent signal is a good feature of the analysis which verify the ability to distinguish different signal models, although the model-independent limits are still influenced by the shape of the resonance in an implicit way. The motivation to choose a Gaussian resonance as a proxy is the fact that it is similar to the 'average' signal with specific width. Besides, the shape of reconstructed jet p_{T} of any realistic signal without very specific model is produced approximately as a Gaussian resonance, without applied JER. Hence it it straightforward to use Gaussian resonances to represent any realistic resonance.

The general form of Gaussian distribution is:

$$f(x) = \frac{1}{\sigma\sqrt{2\pi}} e^{-\frac{1}{2}\left(\frac{x-\mu}{\sigma}\right)^2} \tag{6.1}$$

where the parameter μ is the mean or expectation of the distribution (and also its median and mode), while the parameter σ is its standard deviation.

6.2 Events selections

The MC and data events are divided into three categories to perform the search: the untagged dijet invariant mass spectrum, one-gluon tagged spectrum, and two-gluon tagged spectrum. The evidence of BSM resonances would appear as peaks in the m_{jj} spectrum formed by two highest p_{T} jets in the events. A series of specific cuts is applied to improved the sensitivity of the searches.

6.2.1 Observables and kinematic variables

The predominant source of dijet events in the SM is two-to-two scattering though the QCD processes. This search exams two key properties of the QCD background:

- The background at high m_{jj} appears as a smooth and continuously falling spectrum.
- The background at high energy strongly peaks in the forward region as a result of Rutherford t- and u-channel poles in the cross sections for certain scattering processes [78].

Resonances of interest have $\cos\theta$ distributions in the detector, which in contrast to Rutherford scattering, are either isotropic or have polynomial behaviour in $\cos\theta$ [1], thus a angular distribution appears. This search therefore defines a $y^*$to indicate the angle separation of the jets in the selected events:

$$y^* = (y_1 - y_2)/2 \tag{6.2}$$

to improve the sensitivity to higher energies where new phenomena are expected. The variables y_1, y_2 represent the rapidity of the leading and subleading jet. The value of the y^* cut on events is optimized for each signal as discussed in Section .6.4.1.

In this analysis, jets are reconstructed with the anti-k_t algorithm with a radius parameter R = 0.4, as implemented in the FASTJET package [79]. The EMTopo jets, reconstructed from topological clusters via procedures described in Section. 4.1, are used. The standard *Loose* cut is applied to jet quality as well as jet cleaning. The summarized jet criteria are shown in Table 6.22.

---

[1] See Ref. [78] p15 for a summary.

Parameter / Observable	Requirement
Algorithm	anti-k_t
R-parameter	0.4
Input Constituent	EMTopo
p_T	>150 GeV
$\lvert\eta\rvert$	<2.1

Table 6.22 Jet selection criteria used in this analysis.

6.2.2 Baseline selection

The triggers used in this analysis is HLT_j420. The baseline event selection is applied for all categories. The GRL and various flags that indicate the status of detector when taking data are provided by the ATLAS Data Quality (DQ) group, are applied to ensure the data integrity. Primary vertex requirement is also included to ensure good quality jets. The baseline cuts are given:

- Good Run List: Requirement that all relevant detectors were in a good state ready for physics.
- LAr: Liquid Argon Calorimeter error rejected (errorState(xAOD::EventInfo::LAr))
- Tile: Tile Calorimeter error rejected (errorState(xAOD::EventInfo::Tile))
- SCT: SCT single event upsets rejected (errorState(xAOD::EventInfo::SCT))
- Core: Incomplete event build rejected (isEventFlagBitSet(xAOD::EventInfo::Core, 18))
- All jets with $p_T > 150$ GeV, $|\eta| < 2.1$, pass *Loose* cleaning cuts
- Passes the lowest unprescaled single-jet trigger: HLT_j420
- Jet multiplicity ≥ 2
- Leading jet $p_T > 380$ GeV.
- $|\Delta\phi|$ between two jets: $|\Delta\phi| > 1.0$
- $m_{jj} > 1100$ GeV

Additional kinematic criteria are applied according to the distributions of signals, in order to optimize the search potential, are then discussed in Section 6.4.1.

6.3 Quark-Gluon sample selection

. The sensitivity of the search on the resonant is expected to increase by distinguishing the type of parton that initiated the jets. The parton types of dijet events as a function of m_{jj} from the MC with a PYTHIA8.186 at LO NNPDF2.3 PDFs is shown in Figure 6.48, suggesting that the search for new resonance can be improved by tagging quark and gluon jets.

In this section we present the search for new particles using the full Run 2 $\sqrt{s} =$ 13 TeVdataset with quark and gluon tagging method.

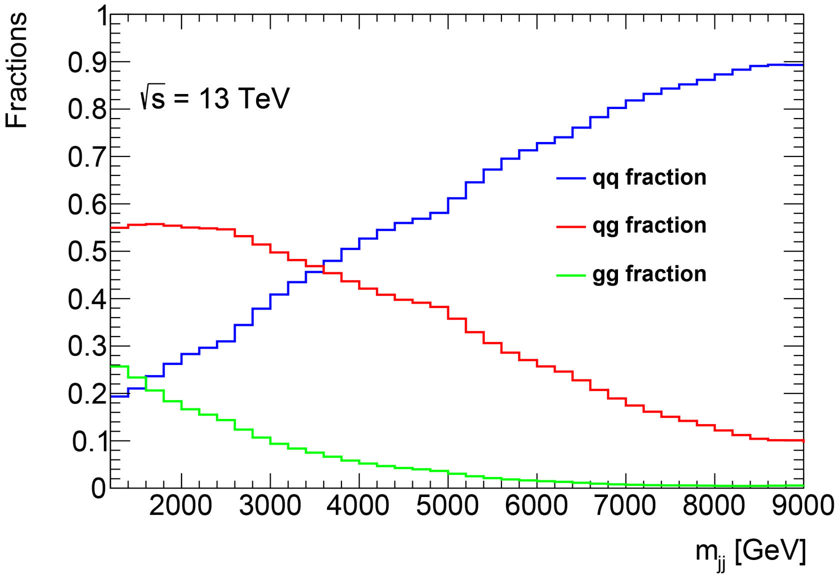

Figure 6.48 The fraction of dijet events that are initiated by quark-quark events (blue), quark-gluon events (green) and gluon-gluon events (red) in simulated data.

Previous study in ATLAS has shown that the jets can be tagged quark or gluon jets based on the number of charged tracks associated with the jets with p_{T} above 500 MeV. Samples with enhanced fractions of quark or gluon initiated jets can be created by using a selection based on the charged-particle constituent multiplicity N_{trk}. As shown in Figure 6.49, where PYTHIA 8 generator is used for MC to ensure a good agreement with the distribution of N_{trk} in data within the ID acceptance $|\eta| < 2.1$.

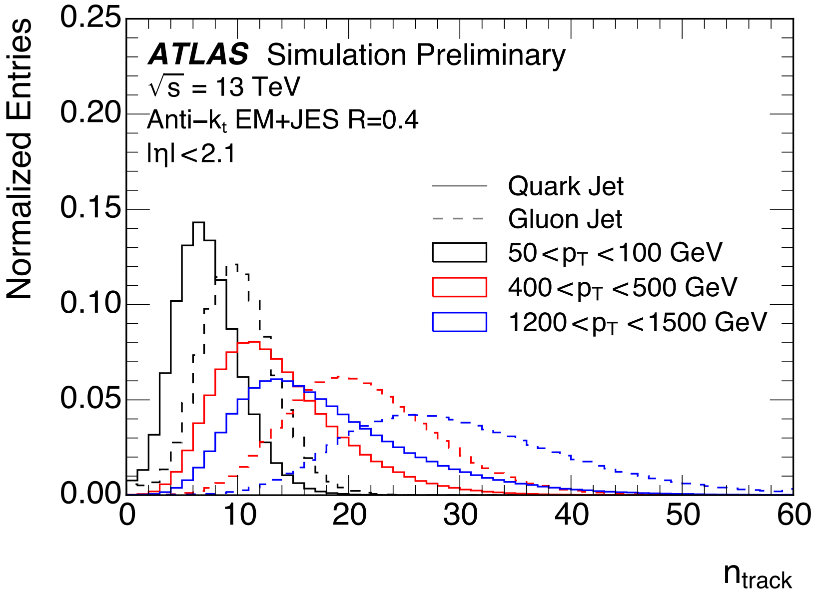

Figure 6.49 Distribution of the jet reconstructed track multiplicity (N_{trk}) in different p_{T} ranges with the PYTHIA 8 MC samples and processes with a full simulation of the ATLAS detector. Tracks are required to have $p_{\mathrm{T}} > 500$ MeV and pass quality criteria described in Ref. [42].

6.3.1 Selection criteria

The selection criteria for an quark-enriched jet sample was chosen so that 60% quark-initiated purity is achieved in each jet p_{T} bin. However, discontinuities in the m_{jj} spectrum would occur when such criteria is applied to the high mass ($p_{\mathrm{T}} > 5000$ GeV), leads to difficulties presented in resonance search.

A selection criteria is thus built as a linear function of the $\ln(p_{\mathrm{T}})$, results in a smooth m_{jj} distribution. A jet is tagged as being more likely to be quark-initiated if N_{trk} is less than the threshold n_{q} and more likely to be gluon-initiated if N_{trk} is greater than the threshold n_{g}:

$$\begin{aligned} N_{\mathrm{trk}} &\leq n_{\mathrm{q}} \text{ quark-initiated sample} \\ N_{\mathrm{trk}} &\geq n_{\mathrm{g}} \text{ gluon-initiated sample} \end{aligned} \tag{6.3}$$

where

$$n_{\mathrm{q(g)}} = c_{\mathrm{q(g)}} + m_{\mathrm{q(g)}} \ln(p_{\mathrm{T}}) \tag{6.4}$$

parameters $m_{\mathrm{q(g)}}$ and $c_{\mathrm{q(g)}}$ are constants obtained from the MC samples, these are founded by finding the value of N_{trk} that corresponds to a given efficiency for truth quark and gluon jets in p_{T} bins, and chosen to defined suitable subsamples, the p_{T} here is in units of GeV.

For each p_{T} bin, the number of tracks N_{trk} that closest to the given selection efficiency is found. Because the N_{trk} is an integer number of track thus does not correspond exactly to the selection efficiency, a linear interpolation is carried out between the given efficiencies of the selected bin and the closest bin of it, to correct the fractional number of tracks that corresponds to the selection efficiency, the corresponding uncertainty is evaluated as binomial distribution.

The jet p_{T} bin edges are divided into 480, 500, 520, 540, 560, 580, 600, 625, 650, 700, 750, 800, 900, 1000, 1400, 1600, 1800, 2000, 2500, 3000, 3500, 4000, 5000, 6000 GeV. An example of the cumulative distribution of N_{trk} for truth quark- and gluon-jets at the p_{T} range of 800 - 900 GeV is shown in Figure 6.50.

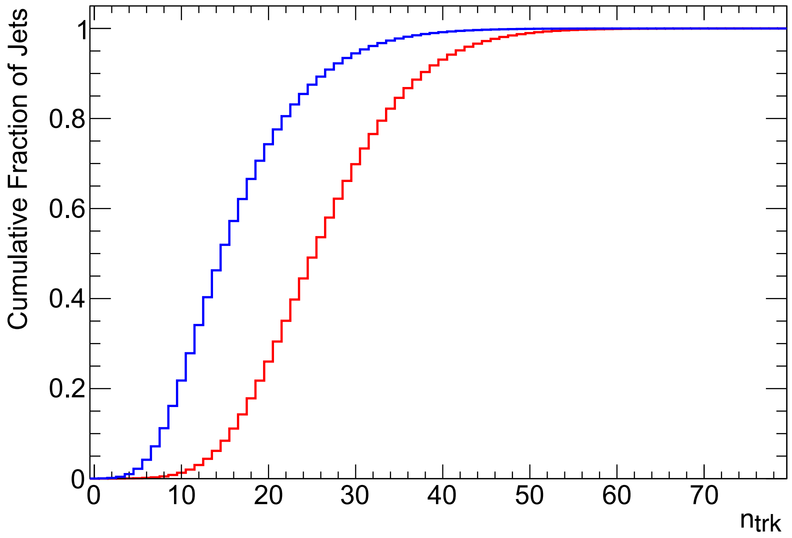

Figure 6.50 The cumulative distribution of N_{trk} for truth quark- (blue) and gluon- (red)jets satisfying 800 < p_{T} < 900 GeV.

The coefficients for Equation 6.4 are determined for quark and gluon selection efficiencies ranging from 65% to 95% in increments of 5%. The plot showcasing the N_{trk} values corresponding to selection efficiencies of 70%, 75%, and 80% is depicted in Figure 6.51, along with the optimal fit employing Equation 6.4. The constants' values for both quark and gluon selections are summarized in Tables 6.23 and 6.24. For a selection efficiency of 75%, the fitting yields a χ^2 of 33.5 (quark selection) and 2.6 (gluon selection) for 21 degrees of freedom.

Notably, the N_{trk} value that satisfies the selection efficiency attains a plateau above

4000 GeV, suggesting the potential presence of a saturation effect. To validate these findings, the data is subjected to an alternative fit function. An alternative fit function is derived as a cross check:

$$n_{\mathrm{q(g)}} = c + m\ln(p_{\mathrm{T}}) + n\sqrt{\ln(p_{\mathrm{T}})}. \tag{6.5}$$

which improve the χ^2 of the fit in a selection efficiency of 75% from 33.5 to 25.1 in quark-selection, and from 2.6 to 1.6 in gluon-selection. Figure 6.52 shows the alternative fit for quark and gluon selections. The values of the constants for both quark and gluon selections are summarised in Tables 6.25 and 6.26.

The values of the constants for both quark and gluon selections are summarised in Tables 6.23 and 6.24.

Truth-q selection efficiency	Truth-g selection efficiency	c	m
0.95	0.732	-27.568	8.789
0.90	0.563	-21.518	7.269
0.85	0.447	-17.646	6.304
0.80	0.339	-14.421	5.475
0.75	0.266	-12.497	4.957
0.70	0.206	-10.591	4.475
0.65	0.174	-8.990	4.105

Table 6.23 Values of constants m and c from Equation. 6.4 such that $N_{\mathrm{trk}} \leq n_{\mathrm{q}}$ for truth quark jets for a range of efficiencies from 65 to 95%.

Truth-g selection efficiency	Truth-q selection efficiency	c	m
0.95	0.586	-7.541	3.233
0.90	0.456	-8.980	3.779
0.85	0.377	-10.419	4.230
0.80	0.309	-12.108	4.679
0.75	0.265	-13.399	5.049
0.70	0.225	-14.841	5.430
0.65	0.202	-16.466	5.834

Table 6.24 Values of constants m and c from Equation 6.4 such that $N_{\mathrm{trk}} \geq n_{\mathrm{g}}$ for truth quark jets for a range of efficiencies from 65 to 95%.

Although the BDT-tagger developed in Chapter 5 have not been implemented in this analysis, the advanced capabilities of this tagger are expected to significantly improve the

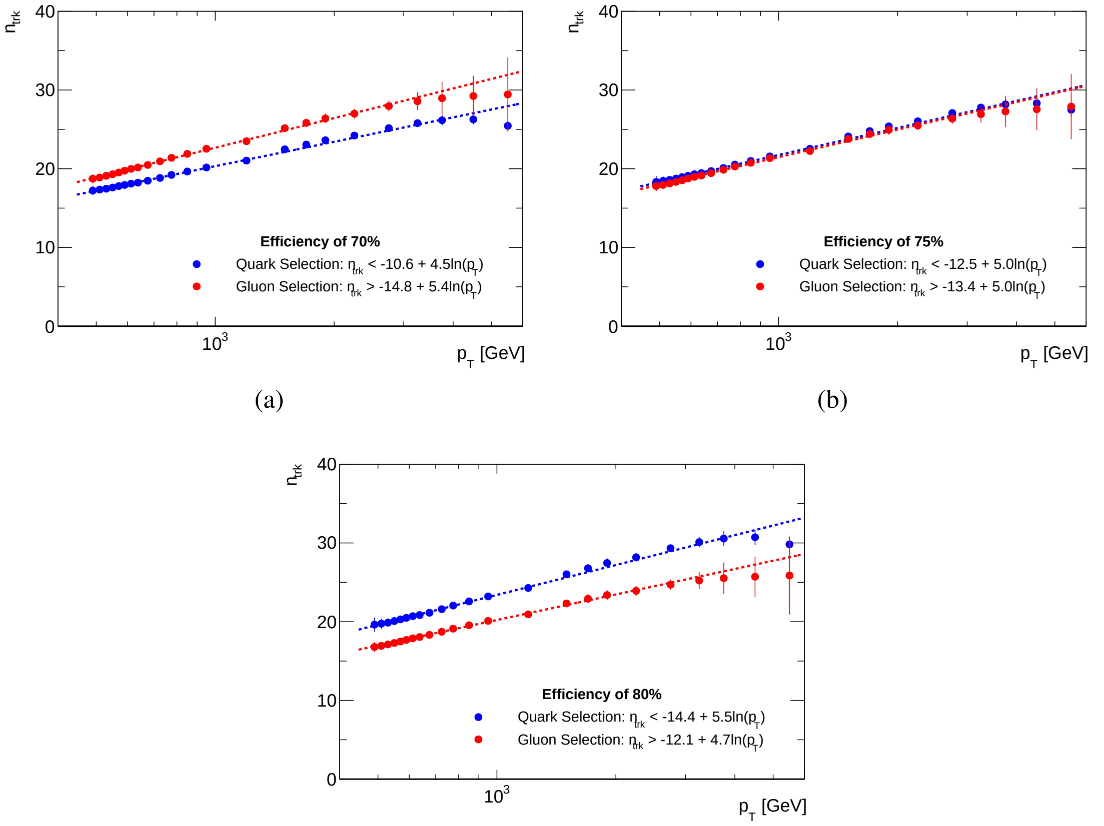

(a)

(b)

(c)

Figure 6.51 The values of N_{trk} for (a) 70%, (b) 75% and (c) 80% quark (blue) and gluon (red) selection efficiencies in each p_{T} bin along with the best fit to Equation 6.4.

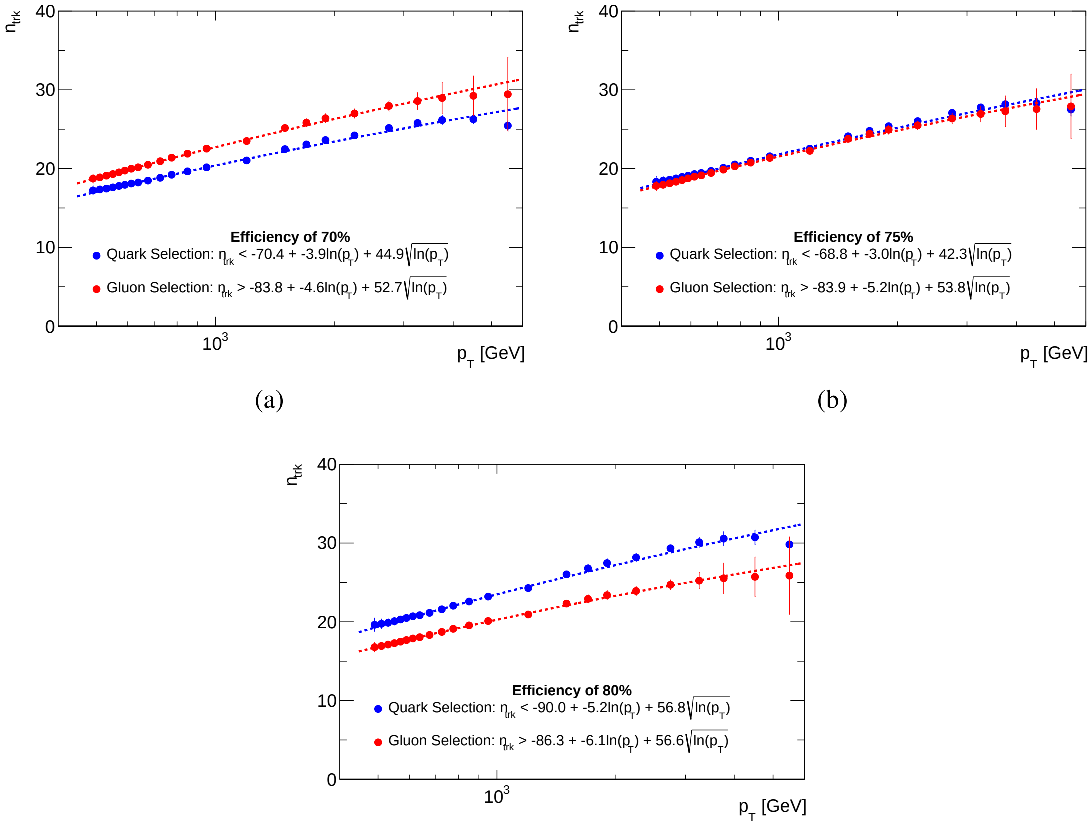

(a) (b)

(c)

Figure 6.52 The values of N_{trk} for (a) 70%, (b) 75% and (c) 80% quark (blue) and gluon (red) selection efficiencies in each p_{T} bin along with the best fit to Equation 6.5.

Truth-q selection efficiency	Truth-g selection efficiency	c	m	n
0.80	0.339	-90.009	-5.177	56.789
0.75	0.266	-68.826	-2.990	42.340
0.70	0.206	-70.383	-3.946	44.906

Table 6.25 Values of constants m and c from Equation 6.5 such that $N_{\mathrm{trk}} \leq n_{\mathrm{q}}$ for truth quark jets for a range of efficiencies from 70 to 80%.

Truth-g selection efficiency	Truth-q selection efficiency	c	m	n
0.80	0.309	-86.321	-6.114	56.621
0.75	0.265	-83.931	-5.214	53.826
0.70	0.225	-83.838	-4.619	52.681

Table 6.26 Values of constants m and c from Equation 6.5 such that $N_{\mathrm{trk}} \geq n_{\mathrm{g}}$ for truth quark jets for a range of efficiencies from 70 to 80%.

discrimination between quark and gluon-initiated jets, thereby enhancing the precision and reliability of dijet analyses in the future.

6.4 Signal optimisation

6.4.1 y^* cut optimisation

In QCD, t-channel in 2-to-2 scattering is the dominant process. Thus the dijet production from the QCD is proportional to $(1-\cos\theta^*)^{-2}$. However the distribution of $\cos\theta^*$ is supposed to be flat for signal, which means the y^* of signal will peak at 0 while that of QCD background will minimize at 0.

The significance is defined as:

$$S = \sqrt{\sum_i 2\left[(S_i+B_i)\cdot\ln\left(1+\frac{S_i}{B_i}\right)-S_i\right]} \tag{6.6}$$

where S_i (B_i) is the number of signal (background) events in bin i. The calculation of such significance only include the bins where signal samples have 95% of the area under the distribution, not include the entire m_{jj} distribution.

For some signal samples where S_i is small ($S_i << 10^{-5}$) thus the logarithm functions do not have enough precision in equation 6.6. An approximation is introduced as follows:

$$S = \sqrt{\sum_i 2\sum_{n=1}^{6}\frac{(-S_i)^{n+1}}{n\,(n+1)\,B_i^n}} \tag{6.7}$$

which is accurate up to 10 decimal places around $\frac{S_i}{B_i} = 10^{-5}$ and even more precise for smaller $\frac{S_i}{B_i}$.

Figure. 6.53 shows the significance of Graviton signal as a function of y^* cut. The significance peaks at about 0.6 to 0.8. Table 6.27 shows the y^* cut corresponding to the peak significance value for Graviton at each mass point, and the range in y^* cut around the peak that gives a significance ≥ 0.99

Figure. 6.54 shows the significance of QBH signal as a function of y^* cut. The maximum significance is at about 0.9, so the optimal cut for the QBH search is $|y^*| < 0.9$. Table 6.28 shows the y^* cut corresponding to the peak significance value for the QBH at each mass point, and the range in y^* cut around the peak that gives a significance ≥ 0.99

However, further study have provided that using multiple signal regions was an over optimisation, so in the analysis, $|y^*| < 0.8$ is used.

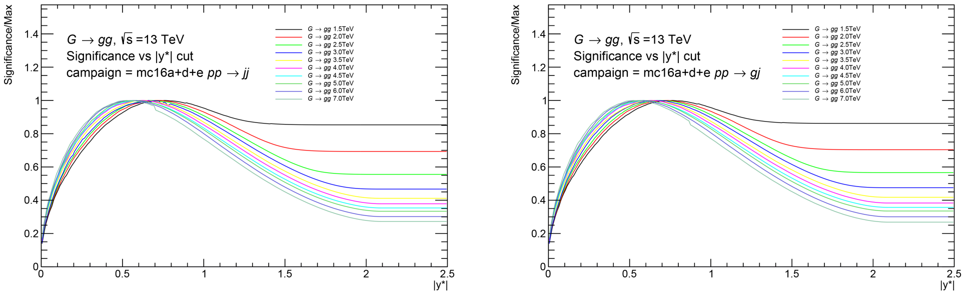

(a) Inclusive (b) ≥1 g-tag

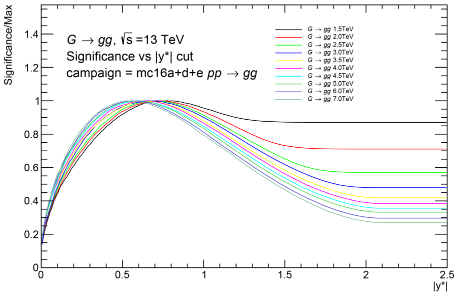

(c) 2 g-tag

Figure 6.53 Graviton significance as a function y^* cut in the case of (a) Inclusive, (b) ≥1 g-tag, (c) 2 g-tag.

Graviton Mass (TeV)	Optimal Selection			Peak Width
	Inclusive	≥ 1 g tag	2 g tag	
1.5	0.77	0.77	0.78	0.65–0.87
2.0	0.71	0.74	0.72	0.65–0.83
2.5	0.67	0.69	0.70	0.61–0.80
3.0	0.66	0.66	0.66	0.60–0.77
3.5	0.64	0.65	0.65	0.57–0.73
4.0	0.63	0.64	0.64	0.55–0.73
4.5	0.59	0.59	0.59	0.53–0.69
5.0	0.59	0.59	0.59	0.50–0.69
6.0	0.57	0.57	0.60	0.49–0.66
7.0	0.53	0.53	0.56	0.47–0.63

Table 6.27 $|y^*|$ selection leading to the maximum significance value calculated using Equation 6.6.

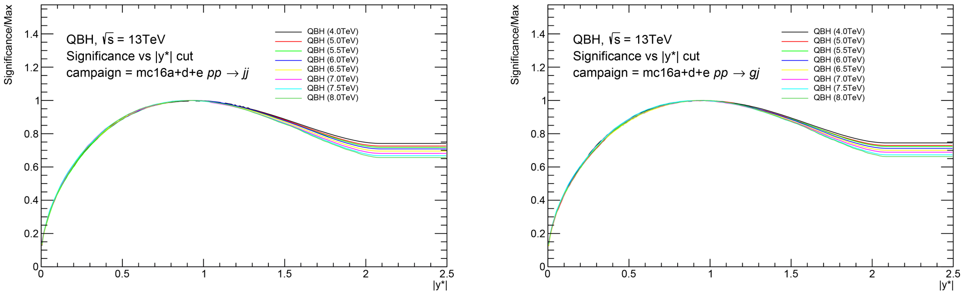

(a) Inclusive

(b) ≥1 g-tag

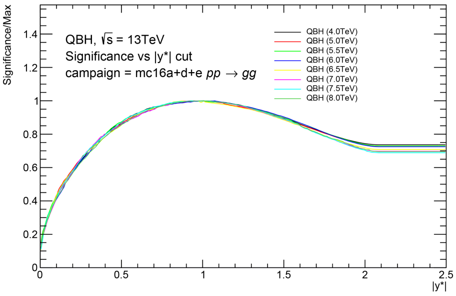

(c) 2 g-tag

Figure 6.54 QBH significance as a function y^* cut in the case of (a) Inclusive, (b) ≥1 g-tag, (c) 2 g-tag.

QBH Mass (TeV)	Optimal Selection			Peak Width
	Inclusive	≥ 1 g tag	2 g tag	
4.0	0.92	0.95	1.01	0.81–1.11
5.0	0.95	0.95	0.95	0.81–1.09
5.5	0.94	0.96	0.94	0.81–1.09
6.0	0.92	0.96	1.01	0.81–1.09
6.5	0.91	0.91	0.93	0.81–1.06
7.0	0.93	0.97	0.94	0.82–1.07
7.5	0.92	0.94	0.93	0.79–1.08
8.0	0.92	0.96	0.99	0.82–1.09

Table 6.28 $|y^*|$ selection leading to the maximum significance value calculated using Equation 6.6.

6.4.2 Optimised selection

In addition to the baseline selection described in Section 6.2.2, optimized cuts are applied to different tagging regions to improve the search potential with good tracking efficiency.

The following additional cuts are applied for the the inclusive samples.

- $|y^*| < 0.8$
- $m_{jj} > 1200$ GeV

The following additional cuts are for quark-gluon tagging.

- $|\eta| < 2.1$ (both jets) for track acceptance
- ≥ 1 gluon tagged (75% working point)
- 2 gluons tagged (75% working point)

where the 75% gluon selection criteria is $n_{\text{track}} > -13.399 + 5.049\ln(p_{\text{T}})$, with p_{T} in GeV.

6.4.3 Selected kinematic plots

In this section a selection of kinematic and monitoring plots processed with samples passed the one- and two-gluon selection criteria are shown in Figure 6.55 to6.58.

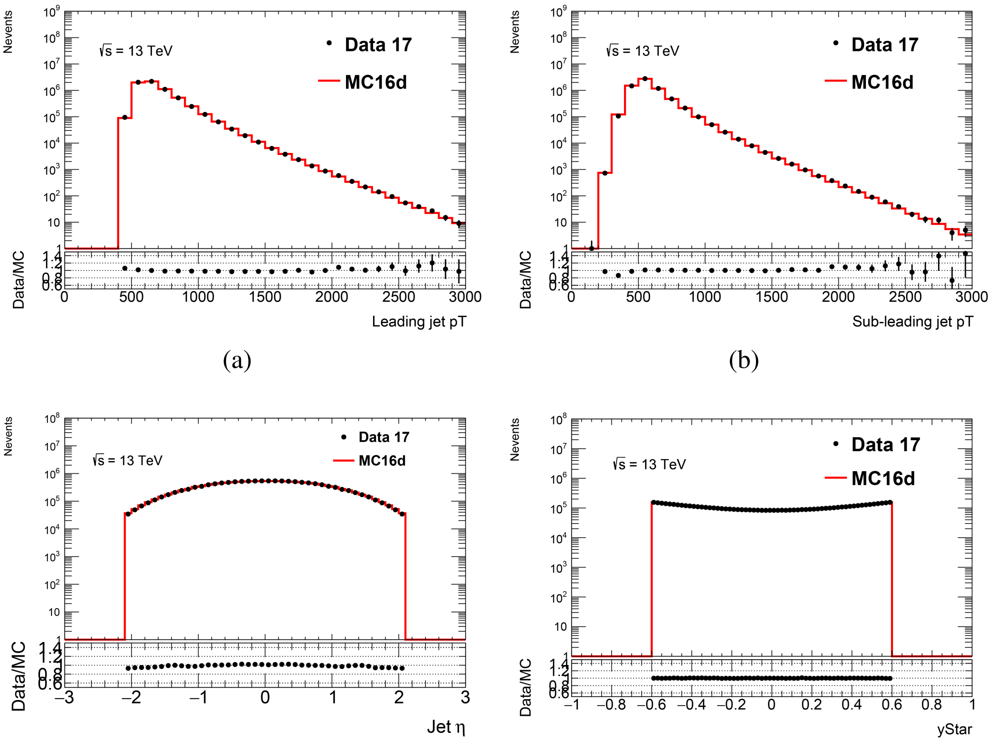

(a) (b)

(c) (d)

Figure 6.55 Monitoring plots for the one-gluon selection. (a) Leading jet p_{T} (b)Sub-leading jet p_{T} (c)) jet η, (d) y* between the two jets

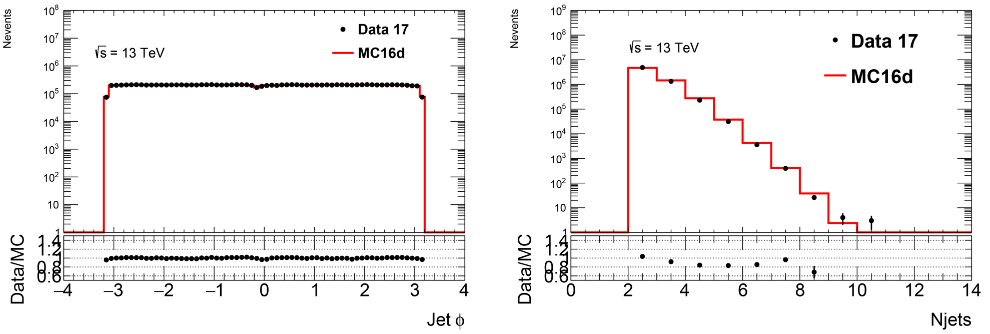

(a) (b)

Figure 6.56 Monitoring plots on the one-gluon sample. (a) $\Delta\phi$ between the two jets, (b) number of jets.

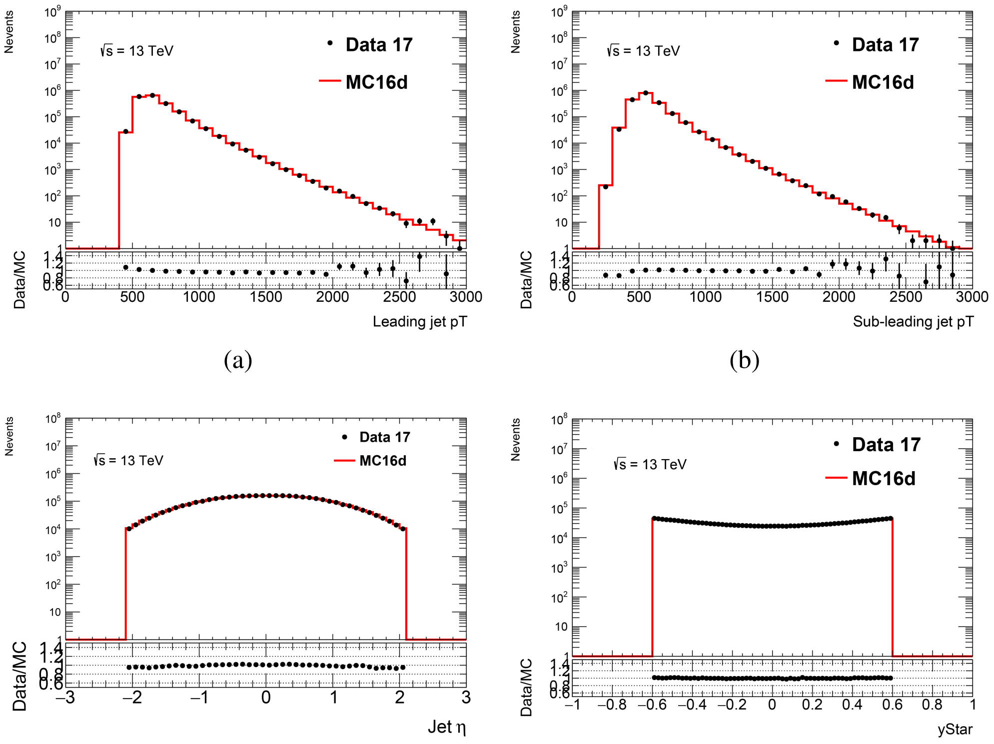

(a) (b)

(c) (d)

Figure 6.57 Monitoring plots for the gluon-gluon selection. (a) Leading jet p_{T} (b)Sub-leading jet p_{T} (c)) jet η, (d) y* between the two jets

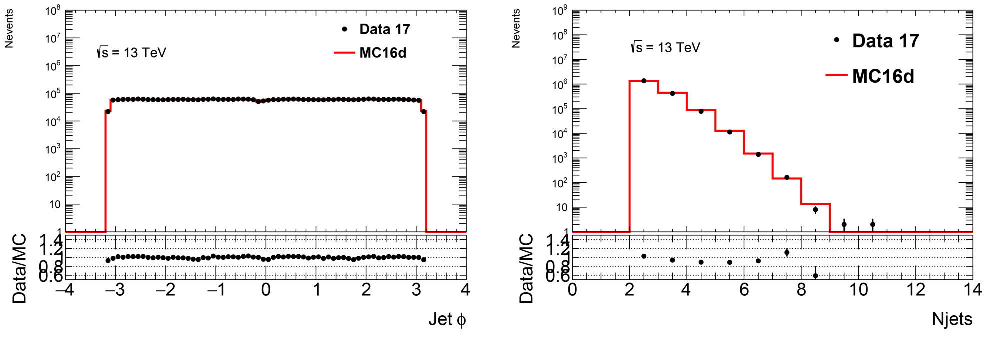

(a) (b)

Figure 6.58 Monitoring plots on the gluon-gluon sample. (a) $\Delta\phi$ between the two jets, (b) number of jets.

6.5 Analysis framework

6.5.1 Fitting framework

The fitting framework used to parameterise QCD background is based on XML Analytic Workspace Builder [80] (xmlAnaWSBuilder), which employs one-dimensional observables to create RooFit [81] workspaces. The workflow of the framework is summarised in Figure 6.59.

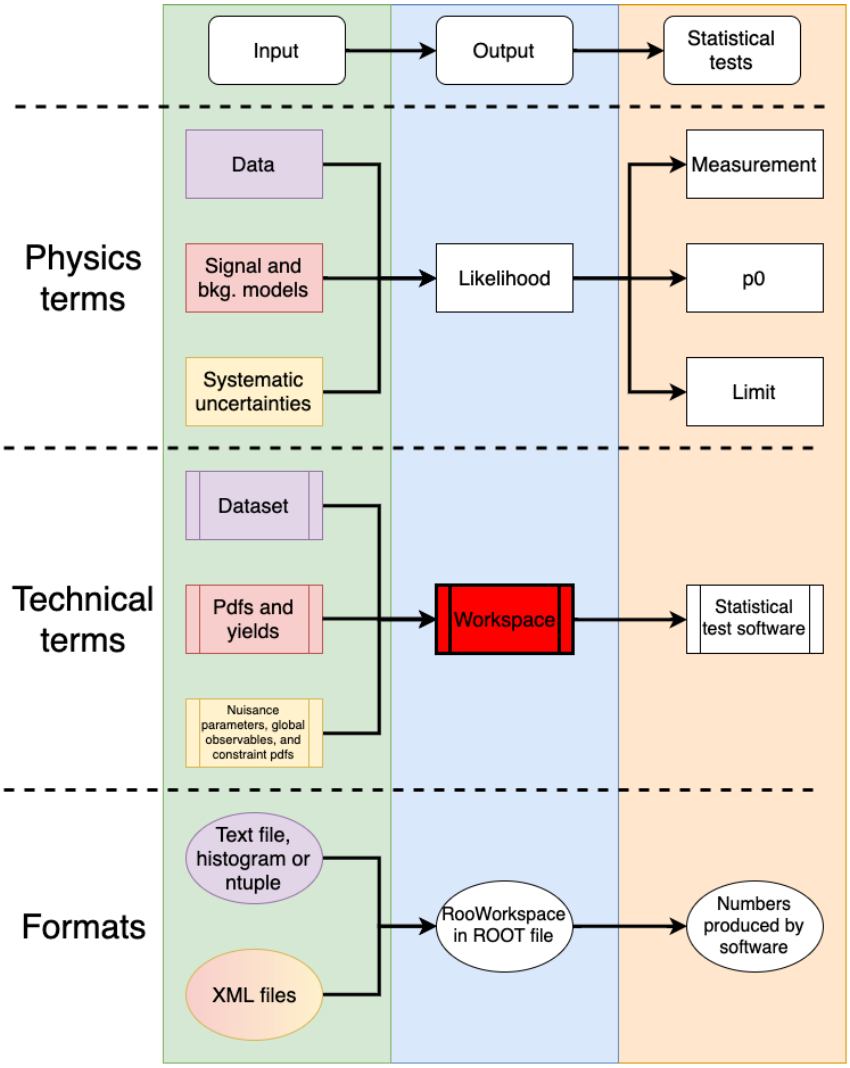

Figure 6.59 Workflow of the XmlAnaWSBuilder.

The xRooFit framework [82] that based on RooFit data fitting package is used for data fitting. Modifications are needed so that it can integrate over binned data, as RooFit evaluates its fit functions using the centre value of each bin rather than the actual average mass in each bin. As a result, significant biases could occur in the fit results [83]. Recent developments introduce a new class of `RooBinSamplingPdf` in to RooFit package, which solve such issue.

6.5.2 Statistical method

In this analysis, the discriminating variable is set to the dijet invariant mass m_{jj}, and the distribution of it is used as a probability density function (pdf) to build the likelihood function.

6.5.2.1 Parametric background models

The distribution of m_{jj} of background is parameterised by

$$f_b(m_{jj};\boldsymbol{p}_b) = f_b(m_{jj};p_1,p_2,p_3,p_4,p_5) = p_1\left(1-\frac{m_{jj}}{\sqrt{s}}\right)^{p_2}\left(\frac{m_{jj}}{\sqrt{s}}\right)^{p_3+p_4\ln\left(\frac{m_{jj}}{\sqrt{s}}\right)+p_5\left[\ln\left(\frac{m_{jj}}{\sqrt{s}}\right)\right]^2} . \tag{6.8}$$

where $\boldsymbol{p}_b$ are free parameters determined by fitting to data (or pseudo data), and $\sqrt{s} =$ 13 TeV. In some cases, $p_5 = 0$ is taken. We will assume Equation (6.8) is normalized to unity as needed.

Given that we are employing a binned likelihood approach and working with histograms, it becomes essential to determine the average count of events in the ith bin, arising from both the signal and background contributions:

$$s_i = s_{\text{tot}}\int_{\text{bin } i} f_s(m_{jj};\boldsymbol{p}_s)dm_{jj} . \tag{6.9}$$

$$b_i = b_{\text{tot}}\int_{\text{bin } i} f_b(m_{jj};\boldsymbol{p}_b)dm_{jj} . \tag{6.10}$$

where f_s and f_b are pdfs of m_{jj} for the signal and background, respectively. The quantities s_{tot} and b_{tot} represent the total mean numbers of signal and background events. The variable b_{tot} is an additional nuisance parameter. The signal normalization s_{tot} is not treated as a parameter that can be adjusted, but rather is set to the value determined by the nominal signal model. The parameter can be expressed as $s_{\text{tot}} = \sigma L\varepsilon$, where σ is fixed by the model cross section, and L and ε represent the nominal luminosity and total acceptance times efficiency, respectively.

6.5.2.2 Uncertainties

In this analysis, there are six sources of systematic uncertainties on the signal studied:

δL an uncertainty on the integrated luminosity of the data sample,

$\delta\varepsilon$ an uncertainty on the signal efficiency times acceptance,

δt an uncertainty on the gluon-tag efficiency,

δE_{JER} an uncertainty on the jet energy resolution.

δE_{JES} an uncertainty on the jet energy scale.

δS an uncertainty due to spurious signals.

All these uncertainties are treated as shape uncertainties except for δL which is a normalization uncertainty. These uncertainties are associated to nuisance parameters denoted by α_L, α_ε, α_t, $\alpha_{E_{\mathrm{JER}}}$, $\alpha_{E_{\mathrm{JES}}}$, α_S, respectively, and the values of the auxiliary measurements by θ_b, θ_L, θ_ε, θ_t, $\theta_{E_{\mathrm{JER}}}$, $\theta_{E_{\mathrm{JES}}}$, θ_S, respectively.

6.5.2.3 Likelihood function definition

A binned likelihood is used in this analysis. Consider the m_{jj} histogram of $\boldsymbol{n} = (n_1, \ldots, n_N)$ events, the likelihood function without uncertainties is built as:

$$\mathscr{L}(\mu; b_{\mathrm{tot}}, \boldsymbol{p}_s, \boldsymbol{p}_b) = \prod_{i=1}^{N} \frac{(\mu s_i + b_i)^{n_i}}{n_i!} e^{-(\mu s_i + b_i)} . \tag{6.11}$$

where the parameter of interest (POI) μ is the signal strength parameter, b_i is the number of background events in the i bin, s_i is the number of signal events in the i bin. Background-only hypothesis corresponding to $\mu = 0$, whereas nominal signal hypothesis corresponding to $\mu = 1$.

The full likelihood function with uncertainties included is defined as:

$$\begin{aligned} \mathscr{L}(\mu; b_{\mathrm{tot}}, \boldsymbol{p}_s, \boldsymbol{p}_b, \boldsymbol{\alpha}_s) &= \prod_{i=1}^{N} \frac{(\mu_i^T)^{n_i}}{n_i!} e^{-\mu_i^T} N_i(\alpha_L; \theta_L, \delta_L) N_i(\alpha_\varepsilon; \theta_\varepsilon, \delta\varepsilon) \\ &\cdot \quad N_i(\alpha_t; \theta_t, \delta E_t) N_i(\alpha_{E_{\mathrm{JER}}}; \theta_{E_{\mathrm{JER}}}, \delta E_{\mathrm{JER}}) \end{aligned} \tag{6.12}$$

$$\cdot \quad N_i(\alpha_{E_\mathrm{JES}};\theta_{E_\mathrm{JES}},\delta E_\mathrm{JES})N_i(\alpha_S;\theta_S,\delta_S)\,. \tag{6.13}$$

where μ_i^T is the total number of expected event in the i bin, which is given by:

$$\mu_i^T = \mu s_i \eta_i^L(\alpha_L)\eta_i^\varepsilon(\alpha_\varepsilon)\eta_i^t(\alpha_t)\eta_i^{E_\mathrm{JER}}(\alpha_{E_\mathrm{JER}})\eta_i^{E_\mathrm{JES}}(\alpha_{E_\mathrm{JES}}) + b_i\,. \tag{6.14}$$

The parameter $\eta^s(\alpha_s)$ are response functions for uncertainty s, and the subsidiary measurements are constrained by the $N(\alpha;\theta,\delta)$ functions.

In this analysis, constraint functions are built from standard Gaussians, together with uncertainties that mapped in the response functions. Luminosity uncertainty is fitted by a log-normal response function, the JER and JES uncertainties are given by Gaussian and asymmetric response functions, respectively. For each bin, a vertical interpolation strategy called piece-wise linear method is used independently. In the case of the asymmetric error, the polynomial interpolation and exponential extrapolation method is used.

The parameters $(\mu, N_b, \boldsymbol{p}_s, \boldsymbol{p}_b, \alpha_L)$ are fixed from the fit to data (pseudo-data) and are common for all bins, whereas parameters $(\alpha_\varepsilon, \alpha_t, \alpha_{E_\mathrm{JER}}, \alpha_{E_\mathrm{JES}}, \alpha_S)$ are different from bin to bin.

For simplicity in notation, the 18 nuisance parameters are writted as the vector $\boldsymbol{\alpha}$, where six of them have corresponding uncertainties. The simplified likelihood function is written as:

$$\mathscr{L}(\mu;\boldsymbol{\alpha}) = \prod_{i=1}^{N} \frac{[\mu_i^T(\mu,\boldsymbol{\alpha})]^{n_i}}{n_i!} e^{-\mu_i^T(\mu,\boldsymbol{\alpha})} \prod_{s=1}^{6} G_{i,s}(\alpha_s)\,. \tag{6.15}$$

6.5.2.4 Statistical method

A hypothesis test is used for estimating the compatibility between data and a theoretical hypothesis, where the pseudo datasets are generated according to a given hypothesis, and compared to the tested dataset in terms of a test statistic.

The procedure is demonstrated as follows: first, the agreement between the collected data and the null hypothesis is evaluated through a hypothesis test. The null hypothesis ($\mu = 0$) posits that only the SM background is present. If the data does not exhibit any substantial excess under this hypothesis test, the subsequent step involves establishing an exclusion limit for the targeted signal model on the resonance cross section for m_{jj} . In this scenario, the hypothesis transforms into a signal + background assumption, leading to the construction of a test statistic based on the signal + background PDF of the discriminating variable.

The statistical measurement's p-value serves as a quantification of the degree of agreement or discrepancy between a hypothesis and the observed data. Mathematically, it represents the integral of the distribution of the test statistic from the value obtained for the dataset in question to infinity. This value characterizes the probability of achieving the observed outcomes assuming the null hypothesis. A lower p-value indicates a higher degree of statistical significance for the observed incompatibility. For instance, if the p-value of the data is below 0.05, it signifies that the likelihood of the observed data aligning with the hypothesis is less than 5%. This prompts the assertion that the hypothesis can be excluded at the 95% confidence level (CL).

6.5.2.5 Test statistic and p-value definitions

A binned maximum likelihood (ML) fitting method is used to extract the signal, together with profile likelihood ratio test statistic. The test statistics used for claiming a positive signal is defined as:

$$q_0 = \begin{cases} -2\ln\frac{\mathscr{L}(0,\hat{\hat{\alpha}}(0))}{\mathscr{L}(\hat{\mu},\hat{\alpha})} & \hat{\mu} \geq 0\,, \\ 0 & \hat{\mu} < 0\,. \end{cases} \tag{6.16}$$

and the test statistic used for evaluating the upper limits is given as:

$$\tilde{q}_\mu = \begin{cases} -2\ln\frac{\mathscr{L}(\mu,\hat{\hat{\alpha}}(\mu))}{\mathscr{L}(0,\hat{\hat{\alpha}}(0)} & \hat{\mu} < \mu\,, \\ -2\ln\frac{\mathscr{L}(\mu,\hat{\hat{\alpha}}(\mu))}{\mathscr{L}(\hat{\mu},\hat{\alpha})} & 0 \leq \hat{\mu} \leq \mu\,, \\ 0 & \hat{\mu} > \mu\,. \end{cases} \tag{6.17}$$

where the parameter μ represents the signal strength associated with the hypothesis being tested. The maximum likelihood (ML) estimators that optimize the likelihood function $\mathscr{L}$ without constraints are referred to as $\hat{\mu}$ for the signal strength and $\hat{\alpha}$ for the other parameters. The parameter $\hat{\hat{\alpha}}$ represents the conditional ML estimator of α that maximizes $\mathscr{L}$ while considering a specific value of μ.

The p-value corresponding to the background-only hypothesis is expressed as:

$$p_0 = \int_{q_{0,\mathrm{obs}}}^{\infty} f(q_0|0)dq_0\,. \tag{6.18}$$

The values of $\tilde{q}_\mu$ are calculated for different values of μ by fitting a dataset where the pseudo data is represented by μ'. This calculation of $\tilde{q}_\mu$ is conducted for each pseudo dataset at various selected signal mass points, resulting in a distribution of $\tilde{q}_\mu$ denoted as $f(\tilde{q}_\mu|\mu = \mu')$. As a result, a p-value for the tested dataset is determined based on this distribution:

$$p_{\mu'} = \int_{\tilde{q}'_{\mu,\mathrm{obs}}}^{\infty} f(\tilde{q}_\mu|\mu = \mu')dq_\mu\,, \tag{6.19}$$

the term $\tilde{q}_{\mu',\mathrm{obs}}$ represents the computed value of the test statistic based on the dataset being tested. These p-values are also referred to as p_{s+b}, which signifies that they are associated with the signal plus background hypothesis.

6.5.2.6 Generation of pseudo-data

The PDF of a certain model is used for generating the pseudo datasets. Signal + background pseudo datasets are utilized to estimate the observed confidence level (CL) of a signal + background hypothesis, while background-only pseudo datasets are employed for expected CL estimations.

During the generation of pseudo datasets, all parameters in the PDF are set to their nominal values. The expected event counts in each bin follow a Poisson distribution. Nuisance parameters (NPs), which represent systematic uncertainties, are treated according to the "unconditional ensemble" approach: for each pseudo dataset, the values of α_i (associated with the NPs) are drawn from their respective constraint terms, and these values are used in both the likelihood $\mathscr{L}$ and the computation of $\tilde{q}_\mu$.

6.5.2.7 Definition of exclusion limit

The data is interpreted by the modified frequentest method (CL_S method), where p-value is modified to take into account downward background fluctuations and quoted as CL_s. The definition of CL_s is:

$$CL_s = \frac{p_{s+b}}{1 - p_b}\,, \tag{6.20}$$

where $p_{b(s+b)}$ is the integrated value of the background-only (signal + background) distribution from zero to $\tilde{q}_\mu^{\mathrm{obs}}$. Thus $1 - p_b$ is also referred to as the confidence level of the background-only hypothesis (CL_b). The CL_s limit claims exclusion at 95% CL when $CL_s = 0.05$.

6.5.2.8 Implementation

In this analysis, the background fit parameters are treated as unconstrained NPs within the complete likelihood framework used in all fits. To create the RooFit workspaces, the XML Analytic Workspace Builder is utilized. The xRooFit tool processes these workspaces and performs operations like setting limits, among others, using classes from the RooFit and RooStats libraries.

6.5.3 Background estimation

In the resonant search the SM background of the m_{jj} spectrum is established through a functional fitting procedure applied to the data. Refs. [84, 85, 86, 87, 88, 89]) have found that a parametric function of the form

$$f(x) = p_1(1-x)^{p_2}x^{p_3+p_4\ln x+p_5(\ln x)^2}. \tag{6.21}$$

where $x \equiv m_{jj}/\sqrt{s}$, accurately describes dijet mass distribution predicted by leading and next-to-leading-order QCD Monte Carlo. In the ATLAS Run 2 analysis with 139.0 fb^{-1} of data [90, 91], the four parameter version of the function ($p_5 = 0$) was found to sufficiently described the data. The introduction of gluon tagging may require more parameters to properly describe the full invariant mass spectrum, where no significant deviation is observed, as shown in Figure 6.60.

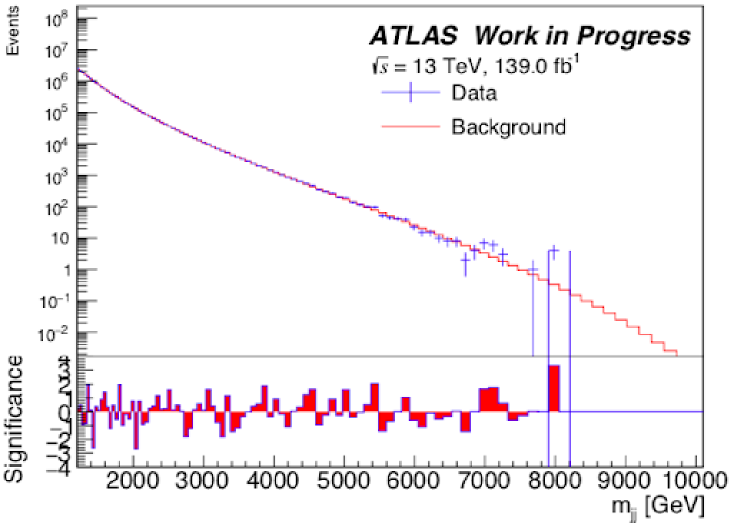

Figure 6.60 m_{jj} background fit.

6.5.4 Analysis workflow

The analysis begins with the utilization of skimmed ntuples, which are the result of applying the event selection criteria outlined in Section 6.4.2. These ntuples serve as the basis for generating pseudo-data using the background-only model. Subsequently, a 4-parameter ($p_5 = 0$) fit function described by Equation 6.21 is employed to fit this pseudo-data. The fit to the data is deemed satisfactory if it meets the following criterion:

- Global χ^2 p-value > 0.05

If the conditions mentioned above are satisfied, the background is chosen for the purpose of upper limit estimations. Conversely, if the criteria are not met, the 5-parameter version of Equation 6.21 is employed for background fitting and is subjected to the same selection criterion. If the fit using the 5-parameter function also fails to meet the criteria, the analysis reduces the range of the window and repeats the fitting process with the 5-parameter function to see if a satisfactory fit can be achieved. If this attempt still does not meet the criteria, the analysis switches to an alternative option for generating pseudo-data. Once a fit satisfying the criteria is obtained, the fit function undergoes various validation tests to ensure the appropriateness of the fit strategy. The flowchart of Figure 6.61 shows the analysis strategy.

6.5.5 Spurious signal tests

The spurious signal test is designed to estimate the difference between the signal yields from the fit and the expected signal yields that given by fitting a known template signal model on a smooth background distribution. Such difference is considered as fit bias and defined as S_{spur}:

$$S_{\text{spur}} = S_{\text{fit}} - S_{\text{template}} \tag{6.22}$$

It is crucial to verify the stability of the fit when applied to a background-only distribution. In this context, no signal is intentionally introduced into the yields, ensuring that the extracted number of signal events remains zero. In the spurious signal test, S_{spur} is determined by fitting a model comprising both signal and background components onto a background-only template. The corresponding uncertainty from the fit is denoted as σ_{fit}. Both the spurious signal S_{spur} and its associated uncertainty σ_{fit} are expected to be consistent with zero.

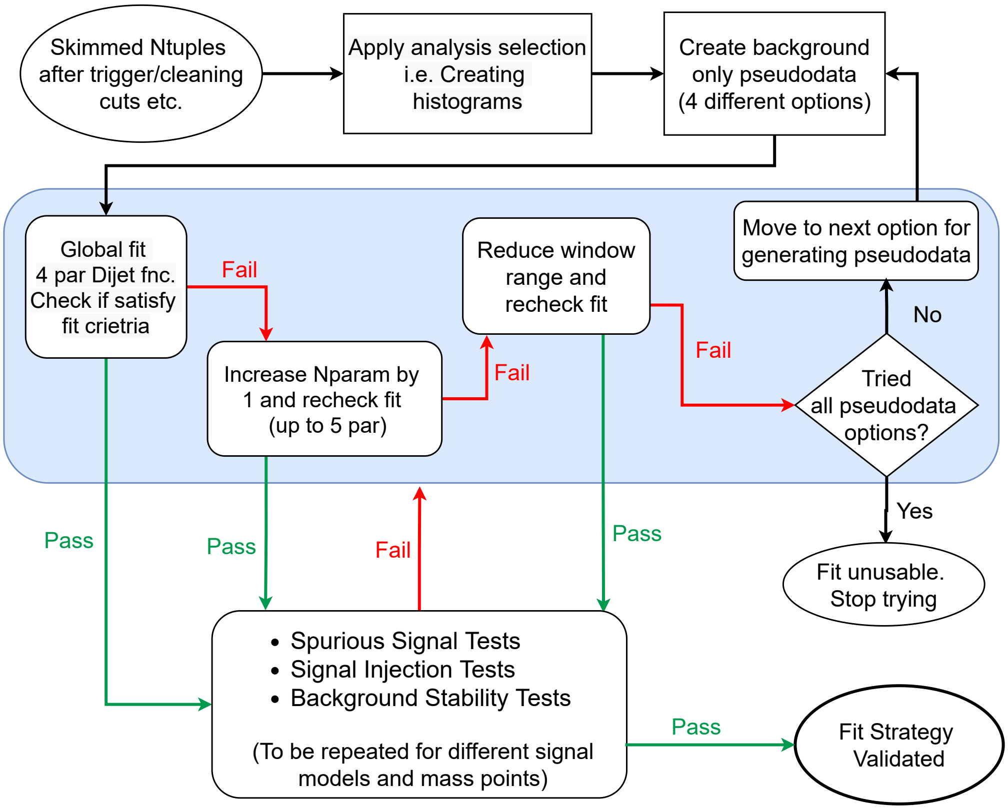

Figure 6.61 Analysis top-level flowchart.

The estimation of the spurious signal is consequently conducted through these pseudo-experiments. The mean value across all experiments is calculated, and a total of 100 pseudo-experiments have been employed. For each individual signal hypothesis, the assessment of spurious signals is conducted at various mass points. The outcomes of the model-independent tests for Gaussian signals, considering different masses and widths, are consolidated in Table 6.29 for the 1 gluon-tagged category and in Table 6.30 for the 2 gluon-tagged category.

Following the recommendations of the Statistical PUB Note [92] , the spurious signal is required to be

$$S_{\text{spur}} < (20\% - 50\%)\sigma_{\text{fit}} \tag{6.23}$$

The idea criteria is when the spurious signal satisfy: $S_{\text{spur}} < 30\%\ \sigma_{\text{fit}}$, but can be loosen up to $50\%\ \sigma_{\text{fit}}$. Most of the tested mass points and widths satisfy the spurious signal criteria. The events of thresholds above 50% is supported by modelling studies in which the background shape is modified to include a true bias of this size, and its effect on the signal yield is probed in the presence of the modelling systematics. Then, the number of retrieved events within a region of 0.1 TeV and 1 TeV is measured, to determine that the fit is stable under no signal injection both in a small region and wide region. In this analysis, the number of retrieved events is consistent with 0 in both cases all across the m_{jj} range.

Mass TeV	Width percentage [%]	Median ± Rms S_{spurious} ± Uncertainty	Ratio S_{spurious}/Uncertainty
2	5	0.19 ± 802.85	2.36E-04
2	10	3.35 ± 1313.79	2.55E-03
2	15	154.92 ± 1666.6	0.093
3	5	1.76 ± 249.13	7.06E-03
3	10	82.55 ± 520.85	0.158
3	15	344.74 ± 803.85	0.429
4	5	48.42 ± 112.34	0.431
4	10	115.89 ± 200.83	0.577
4	15	2.02 ± 242.15	8.34E-03
5	5	0.021 ± 31.77	6.61E-04
5	10	0.012 ± 31.96	3.75E-04
5	15	0.006 ± 18.98	3.16E-04
6	5	7.82E-04 ± 5.54	1.41E-04
6	10	2.84E-04 ± 5.93	4.79E-05
6	15	3.62E-04 ± 5.79	6.25E-05
7	5	8.65E-04 ± 2.66	3.25E-04
7	10	1.6E-04 ± 2.59	6.18E-05
7	15	8.34E-05 ± 2.71	3.08E-05

Table 6.29 Spurious Signal tests using Gaussian signals for 1 gluon tagged category.

Mass TeV	Width percentage [%]	Median ± Rms S_{spurious} ± Uncertainty	Ratio S_{spurious}/Uncertainty
2	5	179.84 ± 635.08	0.283
2	10	757.07 ± 1265.99	0.598
2	15	1666.24 ± 2126.08	0.784
3	5	1.83E-03 ± 85.31	2.14E-05
3	10	0.27 ± 125.63	2.15E-03
3	15	0.021 ± 113.74	1.85E-04
4	5	1.91E-03 ± 25.6	7.46E-05
4	10	3.55E-03 ± 38.68	9.18E-05
4	15	1.50E-03 ± 27.01	5.55E-05
5	5	2.72E-04 ± 7.13	3.81E-05
5	10	9.99E-05 ± 5.57	1.79E-05
5	15	2.1E-04 ± 4.72	4.45E-05
6	5	1.37E-04 ± 1.92	7.14E-05
6	10	1.47E-04 ± 3.25	4.52E-05
6	15	6.49E-05 ± 2.59	2.51E-05
7	5	1.88E-04 ± 1.19	1.58E-04
7	10	1.17E-04 ± 1.17	1.0E-04
7	15	7.83E-05 ± 1.20	6.53E-05

Table 6.30 Spurious Signal tests using Gaussian signals for 2 gluon tagged category.

6.5.6 Fit stability tests

The fit stability tests are employed to assess the behaviour of the background fit function under different scenarios: when applied to the background-only template and the signal + background template. A comparison is made between the fit results obtained from these two templates. Ideally, the background fit function should yield consistent outcomes in both cases. The results of these fit stability tests are presented in Table 6.31 through Table 6.32, encompassing various signal strengths and mass points.

Notably, the background estimation derived from the signal + background fit (B_1) aligns with the background estimation obtained from the background-only fit (B_2), indicating good agreement between the two approaches.

Mass (TeV)	Width (percentage)	Signal Strength	B_1 from S+B fit Mean ± Rms	B_2 from B-only fit Mean ± Rms
2	5	1	20062716.45 ± 4370.57	20064025.61 ± 4003.07
2	5	3	20063730.27 ± 4882.09	20067248.18 ± 4003.14
2	5	5	20062961.53 ± 4521.62	20070470.90 ± 4003.36
5	5	1	20062414.49 ± 4005.80	20062458.64 ± 4003.05
5	5	3	20062420.85 ± 4002.94	20062547.11 ± 4003.09
5	5	5	20062420.96 ± 4002.82	20062635.82 ± 4003.25
5	10	1	20062435.18 ± 4010.37	20062483.50 ± 4002.87
5	10	3	20062448.75 ± 4007.22	20062622.26 ± 4002.95
5	10	5	20061413.12 ± 3682.05	20062761.08 ± 4003.12
7	5	1	20062420.38 ± 4002.68	20062420.29 ± 4002.98
7	5	3	20062422.56 ± 4002.86	20062432.08 ± 4003.08
7	5	5	20062422.86 ± 4002.98	20062444.09 ± 4003.20

Table 6.31 Fit Stability tests using Gaussian signals for 1 gluon tagged category.

Mass (TeV)	Width (percentage)	Signal Strength	B_1 from S+B fit Mean ± Rms	B_2 from B-only fit Mean ± Rms
2	5	1	3901512.92 ± 2163.27	3902240.71 ± 2048.04
2	5	3	3901530.76 ± 2166.98	3903253.55 ± 2047.37
2	5	5	3901621.90 ± 2291.01	3905032.95 ± 2050.68
5	5	1	3901529.75 ± 2049.31	3901559.92 ± 2046.18
5	5	3	3901528.52 ± 2049.15	3901589.41 ± 2044.93
5	5	5	3901533.99 ± 2047.48	3901621.88 ± 3901586.68
5	10	1	3901536.86 ± 2047.40	3901566.44 ± 2048.23
5	10	3	3901535.71 ± 2054.62	3901616.49 ± 2050.26
5	10	5	3901538.47 ± 2049.54	3901670.56 ± 2047.94
7	5	1	3901531.27 ± 2047.30	3901538.45 ± 2049.16
7	5	3	3901540.72 ± 2068.73	3901542.75 ± 2048.46
7	5	5	3901533.13 ± 2052.64	3901540.09 ± 2048.94

Table 6.32 Fit Stability tests using Gaussian signals for 2 gluon tagged category.

6.6 Systematic uncertainties

Indeed, obtaining uncertainties for a q/g tagger built upon track multiplicity poses challenges, particularly in the higher p_{T} range. This difficulty is partly attributed to the limited statistics available beyond 1 TeV, where fewer gluon-jets are present due to their tendency to be produced at lower masses compared to quark-jets. Consequently, an issue arises in equations that necessitate the average number of tracks in quark- or gluon-jets to facilitate calculations. The scarcity of data points at higher p_{T} values hampers the robust estimation of these averages, contributing to the uncertainty challenge in this context.

The determination of the fraction of jets classified as quark- or gluon-initiated jets is accomplished through the ratio f_q^f/f_g^c, where the superscript f (c) designates the jet with the higher (lower) η value in simulated dijet events. These fractions are derived by convolving parton distribution functions with matrix element calculations. The number of charged tracks events in the jet with higher η can be described by the following system of equations [42]:

$$\langle n^f_{\text{charged}} \rangle = f_q^f \langle n^q_{\text{charged}} \rangle + f_g^f \langle n^g_{\text{charged}} \rangle \, \langle n^c_{\text{charged}} \rangle = f_q^c \langle n^q_{\text{charged}} \rangle + f_g^c \langle n^g_{\text{charged}} \rangle \,. \tag{6.24}$$

These equations require two samples with different fractions of quark- and gluon-jets. While theoretically valid even at high p_{T} values, their applicability diminishes in the high p_{T} regime due to the exceedingly small fractions of gluon jets. Notably, the main sources of uncertainty stem from discrepancies in the MC modelling and the challenges associated with reconstructing charged tracks within jets. This is especially relevant as the separation between tracks is comparable to the resolution of the detector. Consequently, the efficiency of the tagger relies on the accurate resolution of tracks for precise N_{trk} determination, which in turn is constrained by available statistics.

They systematic uncertainty can be estimated by using pure MC simulations and is expected to be substantial, yet smaller than that obtained from data at the edges of the mass range. This technique is particularly effective where statistics are not limited, such as in the central region of the p_{T} distribution. Such an approach has proven to be the optimal choice. To extend the uncertainties into the higher p_{T} regime, particle-level effects and MC reconstruction effects are incorporated. These uncertainties pertain to "in-situ" considerations, making it reasonable to employ them during an extrapolation procedure.

The procedure is performed at constant p_{T} ranges, as N_{trk} depends only on p_{T} and the parton type that initiating jets, uncertainties can be computed by comparing the distribution of N_{trk} in bins of jet p_{T} , which generated from different simulation models. Thus different type of MC generators could introduce underlying uncertainties to the results. Details on different types of theoretical uncertainties and the samples used to estimate them are described in Section 5.7. Uncertainties from experiments are described in Section 6.5.2.2.

The distribution of N_{trk}versus jet p_{T} for 75% gluon tagging working point can be seen in Figure 6.62 for the two Herwig samples.

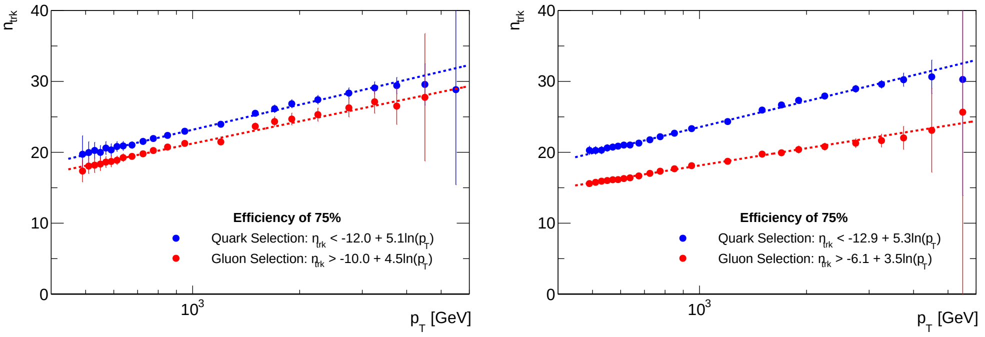

(a) (b)

Figure 6.62 The values of N_{trk} for 75% quark (blue) and gluon (red) selection efficiencies in each p_{T} bin obtained with (a) Herwig Angular-ordered, and (b) Herwig Dipole MC samples.

Sherpa with Cluster-based hadronisation (Sherpa CSS) and Sherpa with String-based hadronisation (Sherpa Lund) model hadronisation, and therefore underlying events, differently. The systematic uncertainty due to hadronisation modelling is estimated from the Sherpa CSS and Sherpa Lund modelling sample. The distribution of N_{trk} versus jet p_{T} for 75% gluon tagging working point can be seen in Figure 6.63 for the two Sherpa samples.

The values of constants m and c from Equation 6.4 such that $N_{\mathrm{trk}} \geq n_{\mathrm{g}}$ for truth quark jets for 75% efficiencies with different dijet MC samples mentioned above are shown in Table 6.33.

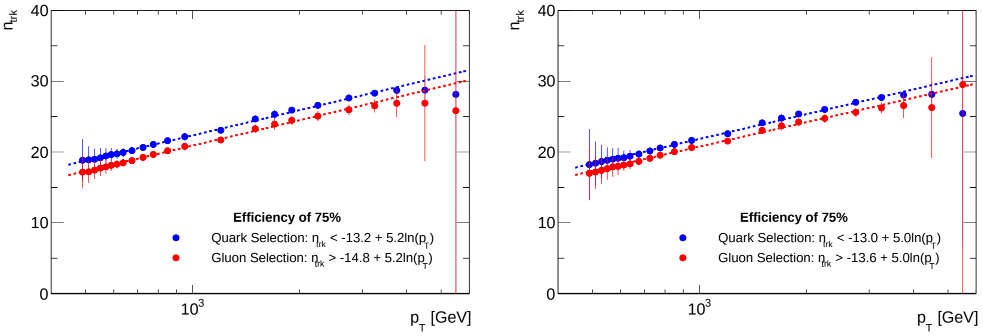

(a) (b)

Figure 6.63 The values of N_{trk} for 75% quark (blue) and gluon (red) selection efficiencies in each p_{T} bin obtained with (a) Sherpa CSS, and (b) Sherpa Lund MC samples.

MC samples	Truth-g selection efficiency	Truth-q selection efficiency	c	m
Pythia	0.75	0.265	-13.399	5.049
Sherpa Lund	0.75	0.283	-13.559	4.969
Sherpa CSS	0.75	0.306	-14.819	5.151
Herwig angular-ordered	0.75	0.474	-6.061	3.504
Herwig dipole-ordered	0.75	0.308	-10.013	4.524

Table 6.33 Values of constants m and c from Equation 6.4 obtained with different MC samples.

untagged Limits [TeV]						
	Obs	Exp $^{+2\sigma}$	Exp $^{+1\sigma}$	Exp	Exp $^{-1\sigma}$	Exp $^{-2\sigma}$
Graviton	3.81	3.16	3.41	3.67	3.91	4.10
QBH	9.88	9.46	9.64	9.86	9.98	10.03

Table 6.34 Limits in the untagged region for signal models.

6.7 Results

Given that no significant deviation from the expected background is observed, the limits derived on several signal models that could cause a resonance in the dijet invariant mass distribution through a frequentist approach. The data used in this analysis is pseudodata, following the ATLAS blind analysis procedure. For the 1-g tagged and 2-g tagged categories, the upper limits are set on the signal cross-section times acceptance times gluon-tagging selection efficiency times branching ratio. The anticipated limits are determined using the asymptotic approximation of the test statistic's distribution, complemented by pseudo-experiments shaped by the background uncertainty values from the maximum-likelihood fit. For signal interpretations in the high-mass regions where the relative discrepancy from the asymptotic approximation exceeds 1%, pseudo-experiments are utilized. The derived limits undergo logarithmic interpolation. No variations are made to the theoretical cross-sections of the signal. Both background and signal sample systematic uncertainties are factored into the limits by adjusting all sources of uncertainty based on Gaussian probability distributions. In the context of the signal models assessed, the couplings of the new physics resonance are notably strong relative to the perturbative QCD scale at the given signal mass, rendering interference with QCD components negligible.

The upper limits obtained on graviton in all categories are shown in Figures 6.64, and on QBH models are given in Figures 6.65. The observed limit in 2-g tagged region gives higher m_{jj} than that in 1-g tagged and untagged regions. Table 6.34 provides a summary of the signal masses corresponding to the lower limits for each benchmark model under consideration in untagged region, whereas Table 6.35 for 1-g tagged and Table 6.36 for 2-g tagged region. The observed excess in Figure 6.64 (c) are mainly caused by pseudodata modelling.

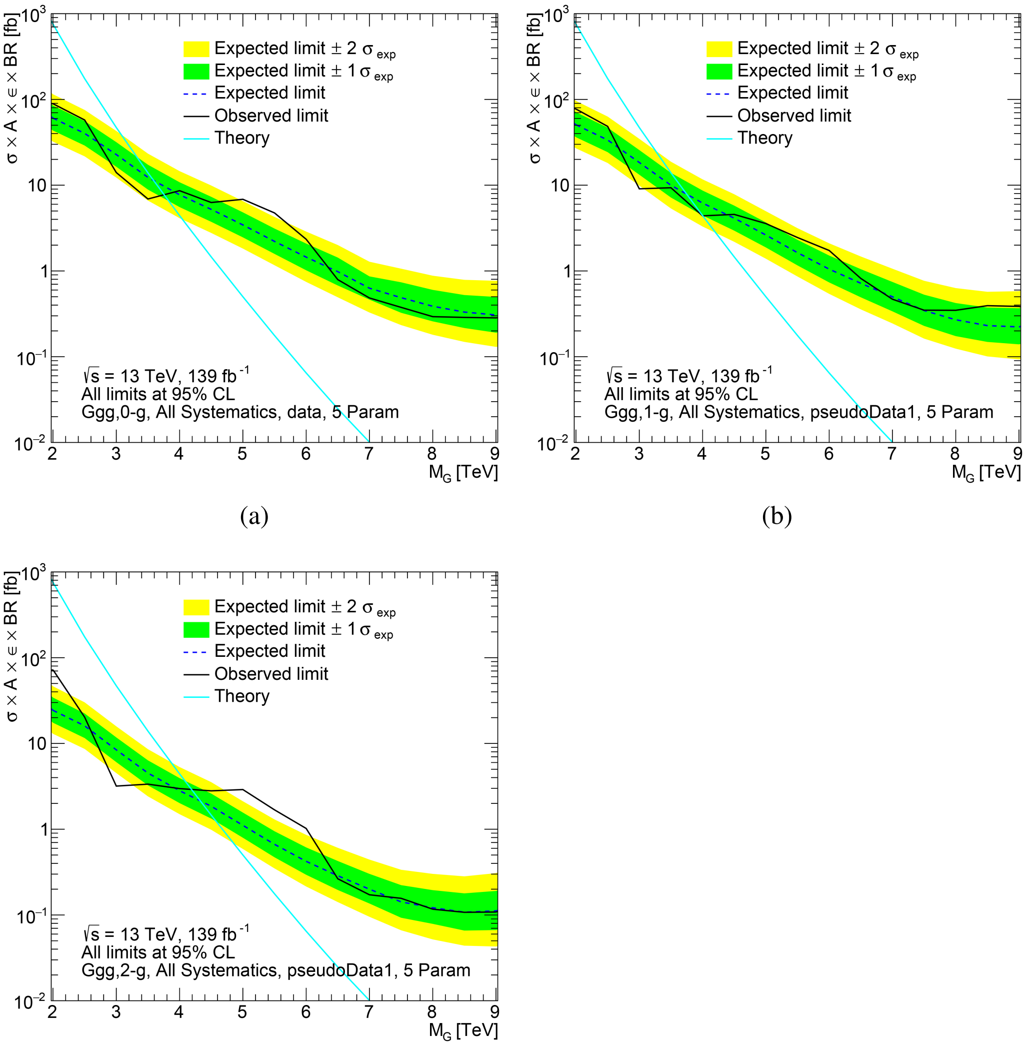

(a) (b)

(c)

Figure 6.64 Upper limits set in the untagged (a), 1-g tagged (b) and 2-g (c) tagged Signal Region using Graviton model with systematics included using the full 139 fb^{-1} Run-2 dataset.

1-g tagged Limits [TeV]						
	Obs	Exp $^{+2\sigma}$	Exp $^{+1\sigma}$	Exp	Exp $^{-1\sigma}$	Exp $^{-2\sigma}$
Graviton	4.01	3.36	3.51	3.85	4.00	4.31
QBH	9.89	9.47	9.68	9.88	9.99	10.04

Table 6.35 Limits in the 1-g tagged region for signal models.

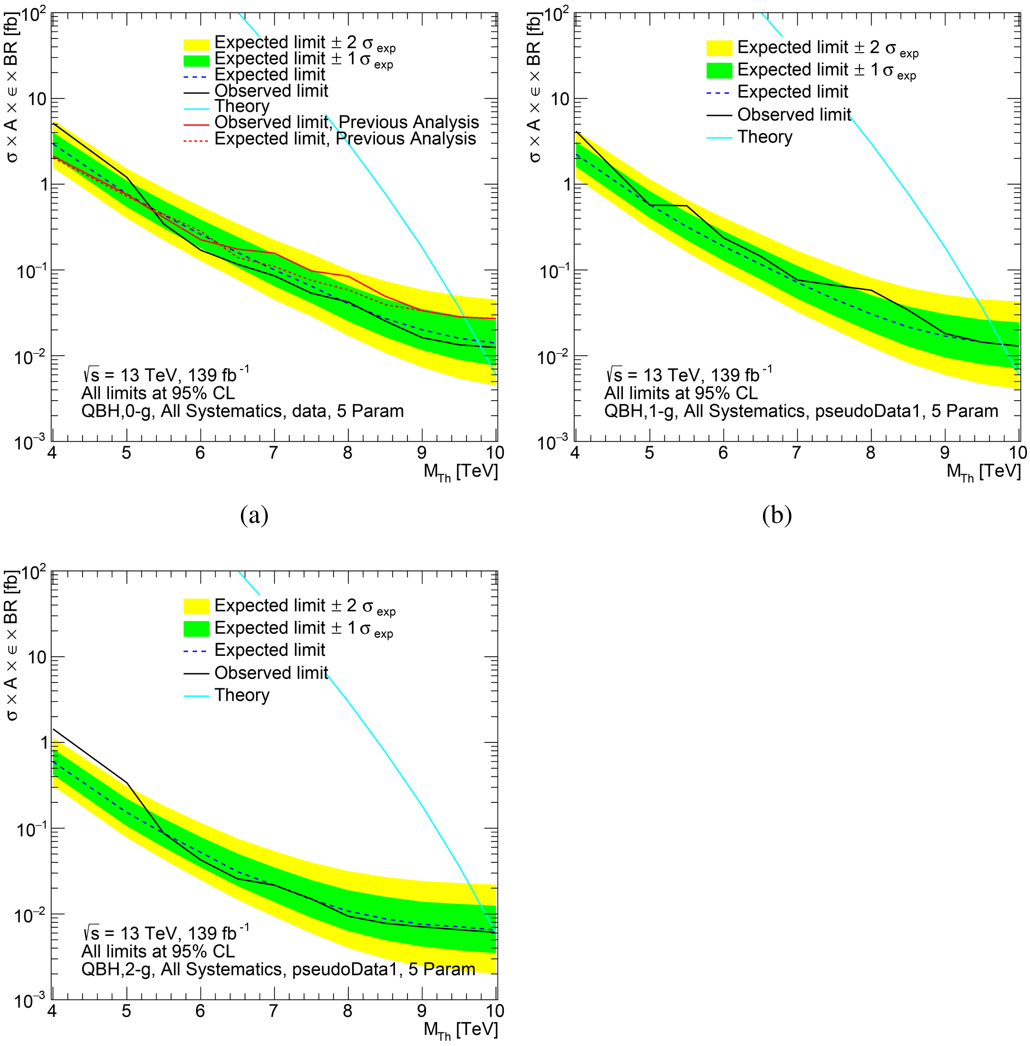

(a) (b)

(c)

Figure 6.65 Upper limits set in the untagged (a), 1-*g* tagged (b) and 2-*g* (c) tagged Signal Region using QBH model with systematics included using the full 139 fb^{-1} Run-2 dataset.

	2-*g* tagged Limits [TeV]					
	Obs	Exp $^{+2\sigma}$	Exp $^{+1\sigma}$	Exp	Exp $^{-1\sigma}$	Exp $^{-2\sigma}$
Graviton	4.26	3.93	4.15	4.41	4.66	4.93
QBH	10.00	9.73	9.90	10.00	10.05	10.07

Table 6.36 Limits in the 2-*g* tagged region for signal models.

7 Conclusions

From 2015 to 2018, the proton-proton collision at the LHC have achieved an unprecedented centre-of-mass energy of $\sqrt{s}$ = 13 TeV, with a total integrated luminosity of 140 fb^{-1} that have been recorded by the ATLAS experiment. Such huge amount of collision data allows scientists to test models beyond the SM in a more efficient way, leading to a deeper understanding of physics beyond the SM.

This thesis presents a search for new resonances that potentially decay into a pair of jets using the data collected by the ATLAS detector during 2015-2018. Resonances predicted by the BSM can decay into quarks and/or gluons. The sensitivity of the search could be significantly increased by introducing jet taggers. This study leverages the extensive dataset recorded between 2015 and 2018 to extend the taggers' applicability to high-energy jets. Two distinct jet tagging methods are explored: a tagger centred on the charged-particle jet constituent multiplicity (N_{trk}), and a BDT-based tagger, which integrates various individual jet substructure observables.

The matrix method is adopted to estimate the distribution shapes of the tagging variables for quark- and gluon-jets. This entails combining information from samples enriched with quark- and gluon-jets, acquired from a selection of dijet events characterized by jet p_{T} ranging from 500 GeV to 2 TeV. The considered variables exhibit a satisfactory agreement with the MC simulations, with discrepancies relative to data measurements being less than 25% across various defined regions.

The BDT-tagger demonstrates superior performance over the N_{trk}-only tagger in distinguishing quark-jets from gluon-jets within the jet p_{T} range of 500 GeV to 1200 GeV. Above this range, the performance of the two taggers becomes comparable. The evaluation of tagger performance differences between data and MC samples is facilitated through the data-to-MC SFs. Four working points of 50%, 60%, 70%, 80% together with all systematics are provided so that analyses can use it based on their own interest. These factors are measured across varying jet-p_{T} intervals, exhibiting a range from 0.92 to 1.02, with a cumulative uncertainty of approximately 20%. The primary contributor to this uncertainty stems from divergent modelling choices within MC simulations, constituting approximately 18% for both taggers. To account for variations between different MC generators, MC-to-MC SFs are also presented, ranging from 0.9 to 1.1 for the majority of MC samples.

The q/g taggers developed in this study and the associated measurement of their SFs hold relevance for various analyses. These applications encompass SM measurements that rely on accurate jet origin identification, as well as BSM physics searches that can capitalize on heightened sensitivity to the presence of new particles. This thesis performs the searches on m_{jj} spectrum. Besides the general dijet search, events featuring jets recognized as either one or two gluon-jets are specifically examined. Benchmark models Graviton and QBH are tested. Because no significant excess in data are found, an upper limit is set to each model in 95% CLs. In this analysis, a comprehensive summary of the lower limits on the signal masses for our benchmark models are given. For example, the observed lower limit set on Graviton mass is 3.81 TeV in untagged region, whereas in 1-g tagged region the mass increases to 4.01 TeV and in 2-g tagged region is 4.26 TeV. For QBH model, the observed lower limit set on its mass is 9.88 TeV in untagged region, whereas in 1-g tagged region the mass increases to 9.89 TeV and in 2-g tagged region, the mass below 10.00 TeV are excluded at 95% CL. The incorporation of gluon-tagging has been greatly enhanced by advancements in the gluon-jet tagging algorithm by 5% for each gluon tagged, especially at high transverse momentum. This has notably improved the sensitivity, offering gains that extend beyond those anticipated from the mere increase in integrated luminosity.

REFERENCES

[1] ATLAS Collaboration. "Search for the Standard Model Higgs boson produced by vector-boson fusion and decaying to bottom quarks in $\sqrt{s} = 8$ TeV pp collisions with the ATLAS detector". In: *JHEP* 11 (2016), p. 112. DOI: `10.1007/JHEP11(2016)112`. arXiv: `1606.02181 [hep-ex]`.

[2] CMS Collaboration. "Electroweak production of two jets in association with a Z boson in proton-proton collisions at $\sqrt{s} = 13$ TeV". In: *Eur. Phys. J. C* 78 (2018), p. 589. DOI: `10.1140/epjc/s10052-018-6049-9`. arXiv: `1712.09814 [hep-ex]`.

[3] ATLAS Collaboration. "Search for diboson resonances with boson-tagged jets in pp collisions at $\sqrt{s} = 13$ TeV with the ATLAS detector". In: *Phys. Lett. B* 777 (2018), p. 91. DOI: `10.1016/j.physletb.2017.12.011`. arXiv: `1708.04445 [hep-ex]`.

[4] Lyndon Evans and Philip Bryant. "LHC Machine". In: *JINST* 3 (2008), S08001. DOI: `10.1088/1748-0221/3/08/S08001`.

[5] CMS Collaboration. "Study of quark and gluon jet substructure in Z+jet and dijet events from pp collisions". In: *JHEP* 01 (2022), p. 188. DOI: `10.1007/JHEP01(2022)188`. arXiv: `2109.03340 [hep-ex]`.

[6] CMS Collaboration. *Performance of quark/gluon discrimination using pp collision data at* $\sqrt{s} = 8$ *TeV*. CMS-PAS-JME-13-002. 2013. URL: `https://cds.cern.ch/record/1599732`.

[7] CMS Collaboration. "Measurements of jet charge with dijet events in pp collisions at $\sqrt{s} = 8$ TeV". In: *JHEP* 10 (2017), p. 131. DOI: `10.1007/JHEP10(2017)131`. arXiv: `1706.05868 [hep-ex]`.

[8] CMS Collaboration. "Studies of jet mass in dijet and W/Z + jet events". In: *JHEP* 05 (2013), p. 090. DOI: `10.1007/JHEP05(2013)090`. arXiv: `1303.4811 [hep-ex]`.

[9] CMS Collaboration. "Measurement of the jet mass in highly boosted $t\bar{t}$ events from pp collisions at $\sqrt{s} = 8$ TeV". In: *Eur. Phys. J. C* 77.7 (2017), p. 467. DOI: `10.1140/epjc/s10052-017-5030-3`. arXiv: `1703.06330 [hep-ex]`.

[10] CMS Collaboration. "Measurement of jet substructure observables in $t\bar{t}$ events from proton-proton collisions at $\sqrt{s} = 13$ TeV". In: *Phys. Rev. D* 98 (2018), p. 092014. DOI: 10.1103/PhysRevD.98.092014. arXiv: 1808.07340 [hep-ex].

[11] CMS Collaboration. "Measurements of the differential jet cross section as a function of the jet mass in dijet events from proton-proton collisions at $\sqrt{s} = 13$ TeV". In: *JHEP* 11 (2018), p. 113. DOI: 10.1007/JHEP11(2018)113. arXiv: 1807.05974 [hep-ex].

[12] A. Altheimer et al. "Jet substructure at the Tevatron and LHC: new results, new tools, new benchmarks". In: *J. Phys. G* 39 (2012), p. 063001. DOI: 10.1088/0954-3899/39/6/063001. arXiv: 1201.0008 [hep-ph].

[13] J. R. Andersen et al. "Les Houches 2015: Physics at TeV Colliders Standard Model Working Group Report". In: *9th Les Houches Workshop on Physics at TeV Colliders*. May 2016. arXiv: 1605.04692 [hep-ph].

[14] Andrew J. Larkoski, Jesse Thaler, and Wouter J. Waalewijn. "Gaining (mutual) information about quark/gluon discrimination". In: *JHEP* 11 (2014), p. 129. DOI: 10.1007/JHEP11(2014)129. arXiv: 1408.3122 [hep-ph].

[15] CDF Collaboration. "Study of jet shapes in inclusive jet production in $p\bar{p}$ collisions at $\sqrt{s} = 1.96$ TeV". In: *Phys. Rev. D* 71 (2005), p. 112002. DOI: 10.1103/PhysRevD.71.112002. arXiv: hep-ex/0505013.

[16] OPAL Collaboration. "Experimental properties of gluon and quark jets from a point source". In: *Eur. Phys. J. C* 11 (1999), pp. 217–238. DOI: 10.1007/s100520050628. arXiv: hep-ex/9903027.

[17] CLEO Collaboration. "Comparison of particle production in quark and gluon fragmentation at $\sqrt{s} \sim 10$ GeV". In: *Phys. Rev. D* 76 (2007), p. 012005. DOI: 10.1103/PhysRevD.76.012005. arXiv: 0704.2766 [hep-ex].

[18] DELPHI Collaboration. "The scale dependence of the hadron multiplicity in quark and gluon jets and a precise determination of C_A/C_F". In: *Phys. Lett. B* 449 (1999), pp. 383–400. DOI: 10.1016/S0370-2693(99)00112-4. arXiv: hep-ex/9903073.

[19] ZEUS Collaboration. "Substructure dependence of jet cross sections at HERA and determination of alpha(s)". In: *Nucl. Phys. B* 700 (2004), pp. 3–50. DOI: `10.1016/j.nuclphysb.2004.08.049`. arXiv: `hep-ex/0405065`.

[20] ATLAS Collaboration. *Quark versus Gluon Jet Tagging Using Jet Images with the ATLAS Detector*. ATL-PHYS-PUB-2017-017. 2017. URL: `https://cds.cern.ch/record/2275641`.

[21] Patrick T. Komiske, Eric M. Metodiev, and Matthew D. Schwartz. "Deep learning in color: towards automated quark/gluon jet discrimination". In: *JHEP* 01 (2017), p. 110. DOI: `10.1007/JHEP01(2017)110`. arXiv: `1612.01551 [hep-ph]`.

[22] C. Frye, A. J. Larkoski, J. Thaler and K. Zhou. "Casimir meets Poisson: improved quark/gluon discrimination with counting observables". In: *JHEP* 09 (2017), p. 083. DOI: `10.1007/JHEP09(2017)083`. arXiv: `1704.06266 [hep-ph]`.

[23] J. Gallicchio and M. D. Schwartz. "Quark and Gluon Tagging at the LHC". In: *Phys. Rev. Lett.* 107 (2011), p. 172001. DOI: `10.1103/PhysRevLett.107.172001`. arXiv: `1106.3076 [hep-ph]`.

[24] J. Gallicchio and M. D. Schwartz. "Quark and gluon jet substructure". In: *JHEP* 04 (2013), p. 090. DOI: `10.1007/JHEP04(2013)090`. arXiv: `1211.7038 [hep-ph]`.

[25] Philippe Gras et al. "Systematics of quark/gluon tagging". In: *JHEP* 07 (2017), p. 091. DOI: `10.1007/JHEP07(2017)091`. arXiv: `1704.03878 [hep-ph]`.

[26] Patrick T. Komiske, Eric M. Metodiev, and Jesse Thaler. "An operational definition of quark and gluon jets". In: *JHEP* 11 (2018), p. 059. DOI: `10.1007/JHEP11(2018)059`. arXiv: `1809.01140 [hep-ph]`.

[27] Particle Data Group. *The Review of Particle Physics*. URL: `http://pdg.lbl.gov`.

[28] Oskar Klein. "Quantum Theory and Five-Dimensional Theory of Relativity. (In German and English)". In: *Z. Phys.* 37 (1926). Ed. by J. C. Taylor, pp. 895–906. DOI: `10.1007/BF01397481`.

[29] Lisa Randall and Raman Sundrum. “A Large mass hierarchy from a small extra dimension”. In: *Phys. Rev. Lett.* 83 (1999), pp. 3370–3373. DOI: 10.1103/PhysRevLett.83.3370. arXiv: hep-ph/9905221.

[30] Stephen Hawking. “Gravitationally Collapsed Objects of Very Low Mass”. In: *Monthly Notices of the Royal Astronomical Society* 152.1 (Apr. 1971), pp. 75–78. DOI: 10.1093/mnras/152.1.75.

[31] S. W. Hawking. “Particle Creation by Black Holes”. In: *Commun. Math. Phys.* 43 (1975). Ed. by G. W. Gibbons and S. W. Hawking, pp. 199–220. DOI: 10.1007/BF02345020.

[32] ATLAS Collaboration. “The ATLAS Experiment at the CERN Large Hadron Collider”. In: *JINST* 3 (2008), S08003. DOI: 10.1088/1748-0221/3/08/S08003.

[33] B. Abbott et al. “Production and integration of the ATLAS Insertable B-Layer”. In: *JINST* 13 (2018), T05008. DOI: 10.1088/1748-0221/13/05/T05008. arXiv: 1803.00844 [physics.ins-det].

[34] ATLAS Collaboration. “Performance of the ATLAS trigger system in 2015”. In: *Eur. Phys. J. C* 77 (2017), p. 317. DOI: 10.1140/epjc/s10052-017-4852-3. arXiv: 1611.09661 [hep-ex].

[35] ATLAS Collaboration. *The ATLAS Collaboration Software and Firmware*. ATL-SOFT-PUB-2021-001. 2021. URL: https://cds.cern.ch/record/2767187.

[36] ATLAS Collaboration. “Jet reconstruction and performance using particle flow with the ATLAS Detector”. In: *Eur. Phys. J. C* 77 (2017), p. 466. DOI: 10.1140/epjc/s10052-017-5031-2. arXiv: 1703.10485 [hep-ex].

[37] Matteo Cacciari, Gavin P. Salam, and Gregory Soyez. “The anti-k_t jet clustering algorithm”. In: *JHEP* 04 (2008), p. 063. DOI: 10.1088/1126-6708/2008/04/063. arXiv: 0802.1189 [hep-ph].

[38] ATLAS Collaboration. “Jet energy scale and resolution measured in proton–proton collisions at $\sqrt{s} = 13$ TeV with the ATLAS detector”. In: *Eur. Phys. J. C* 81.8 (2021), p. 689. DOI: 10.1140/epjc/s10052-021-09402-3. arXiv: 2007.02645 [hep-ex].

[39] ATLAS Collaboration. "Jet energy scale measurements and their systematic uncertainties in proton-proton collisions at $\sqrt{s} = 13$ TeV with the ATLAS detector". In: *Phys. Rev. D* 96 (Oct. 2017), p. 072002. DOI: 10.1103/PhysRevD.96.072002. arXiv: 1703.09665 [hep-ex].

[40] G. Altarelli and G. Parisi. "Asymptotic freedom in parton language". In: *Nucl. Phys. B* 126.2 (1977), pp. 298–318. DOI: https://doi.org/10.1016/0550-3213(77)90384-4.

[41] ATLAS Collaboration. "Light-quark and gluon jet discrimination in pp collisions at $\sqrt{s} = 7$ TeV with the ATLAS detector". In: *Eur. Phys. J. C* 74 (2014), p. 3023. DOI: 10.1140/epjc/s10052-014-3023-z. arXiv: 1405.6583 [hep-ex].

[42] ATLAS Collaboration. *Quark versus Gluon Jet Tagging Using Charged-Particle Constituent Multiplicity with the ATLAS Detector*. ATL-PHYS-PUB-2017-009. Geneva, 2017. URL: https://cds.cern.ch/record/2263679.

[43] ATLAS Collaboration. "Luminosity determination in *pp* collisions at $\sqrt{s} = 13$ TeV using the ATLAS detector at the LHC". In: (Dec. 2022). arXiv: 2212.09379 [hep-ex].

[44] ATLAS Collaboration. "ATLAS data quality operations and performance for 2015–2018 data-taking". In: *JINST* 15.04 (2020), P04003. DOI: 10.1088/1748-0221/15/04/P04003. arXiv: 1911.04632 [physics.ins-det].

[45] Torbjörn Sjöstrand et al. "An introduction to PYTHIA 8.2". In: *Comput. Phys. Commun.* 191 (2015), p. 159. DOI: 10.1016/j.cpc.2015.01.024. arXiv: 1410.3012 [hep-ph].

[46] NNPDF Collaboration, Richard D. Ball, et al. "Parton distributions with LHC data". In: *Nucl. Phys. B* 867 (2013), p. 244. DOI: 10.1016/j.nuclphysb.2012.10.003. arXiv: 1207.1303 [hep-ph].

[47] ATLAS Collaboration. *ATLAS Pythia 8 tunes to 7 TeV data*. ATL-PHYS-PUB-2014-021. 2014. URL: https://cds.cern.ch/record/1966419.

[48] Enrico Bothmann et al. "Event generation with Sherpa 2.2". In: *SciPost Phys.* 7.3 (2019), p. 034. DOI: 10.21468/SciPostPhys.7.3.034. arXiv: 1905.09127 [hep-ph].

[49] Steffen Schumann and Frank Krauss. “A parton shower algorithm based on Catani–Seymour dipole factorisation”. In: *JHEP* 03 (2008), p. 038. DOI: 10.1088/1126-6708/2008/03/038. arXiv: 0709.1027 [hep-ph].

[50] Jan-Christopher Winter, Frank Krauss, and Gerhard Soff. “A modified cluster-hadronization model”. In: *Eur. Phys. J. C* 36 (2004), pp. 381–395. DOI: 10.1140/epjc/s2004-01960-8. arXiv: hep-ph/0311085.

[51] Sayipjamal Dulat et al. “New parton distribution functions from a global analysis of quantum chromodynamics”. In: *Phys. Rev. D* 93.3 (2016), p. 033006. DOI: 10.1103/PhysRevD.93.033006. arXiv: 1506.07443 [hep-ph].

[52] Torbjorn Sjöstrand, Stephen Mrenna, and Peter Z. Skands. “PYTHIA 6.4 physics and manual”. In: *JHEP* 05 (2006), p. 026. DOI: 10.1088/1126-6708/2006/05/026. arXiv: hep-ph/0603175.

[53] Johannes Bellm et al. “Herwig 7.0/Herwig++ 3.0 release note”. In: *Eur. Phys. J. C* 76.4 (2016), p. 196. DOI: 10.1140/epjc/s10052-016-4018-8. arXiv: 1512.01178 [hep-ph].

[54] L. A. Harland-Lang et al. “Parton distributions in the LHC era: MMHT 2014 PDFs”. In: *Eur. Phys. J. C* 75.5 (2015), p. 204. DOI: 10.1140/epjc/s10052-015-3397-6. arXiv: 1412.3989 [hep-ph].

[55] Paolo Nason. “A new method for combining NLO QCD with shower Monte Carlo algorithms”. In: *JHEP* 11 (2004), p. 040. DOI: 10.1088/1126-6708/2004/11/040. arXiv: hep-ph/0409146.

[56] Stefano Frixione, Paolo Nason, and Carlo Oleari. “Matching NLO QCD computations with parton shower simulations: the POWHEG method”. In: *JHEP* 11 (2007), p. 070. DOI: 10.1088/1126-6708/2007/11/070. arXiv: 0709.2092 [hep-ph].

[57] Simone Alioli et al. “A general framework for implementing NLO calculations in shower Monte Carlo programs: the POWHEG BOX”. In: *JHEP* 06 (2010), p. 043. DOI: 10.1007/JHEP06(2010)043. arXiv: 1002.2581 [hep-ph].

[58] The NNPDF Collaboration, Richard D. Ball, et al. “Parton distributions for the LHC run II”. In: *JHEP* 04 (2015), p. 040. DOI: 10.1007/JHEP04(2015)040. arXiv: 1410.8849 [hep-ph].

[59] ATLAS Collaboration. “Performance of the ATLAS track reconstruction algorithms in dense environments in LHC Run 2”. In: *Eur. Phys. J. C* 77.10 (2017), p. 673. DOI: 10.1140/epjc/s10052-017-5225-7. arXiv: 1704.07983 [hep-ex].

[60] Matteo Cacciari and Gavin P. Salam. “Pileup subtraction using jet areas”. In: *Phys. Lett. B* 659.1 (2008), pp. 119–126. DOI: https://doi.org/10.1016/j.physletb.2007.09.077. arXiv: 0707.1378 [hep-ph].

[61] CDF Collaboration. “Measurement of b-jet shapes in inclusive jet production in $p\bar{p}$ collisions at $\sqrt{s}$ = 1.96 TeV”. In: *Phys. Rev. D* 78 (2008), p. 072005. DOI: 10.1103/PhysRevD.78.072005. arXiv: 0806.1699 [hep-ex].

[62] ATLAS Collaboration. “Measurement of jet shapes in top-quark pair events at $\sqrt{s}$ = 7 TeV using the ATLAS detector”. In: *Eur. Phys. J. C* 73.12 (2013), p. 2676. DOI: 10.1140/epjc/s10052-013-2676-3. arXiv: 1307.5749 [hep-ex].

[63] ATLAS Collaboration. “Measurement of the flavour composition of dijet events in pp collisions at $\sqrt{s} = 7$ TeV with the ATLAS detector”. In: *Eur. Phys. J. C* 73.2 (2013), p. 2301. DOI: 10.1140/epjc/s10052-013-2301-5. arXiv: 1210.0441 [hep-ex].

[64] ATLAS Collaboration. “Measurement of jet charge in dijet events from $\sqrt{s}$ = 8 TeV pp collisions with the ATLAS detector”. In: *Phys. Rev. D* 93.5 (2016), p. 052003. DOI: 1103/PhysRevD.93.052003. arXiv: 1509.05190 [hep-ex].

[65] David Krohn et al. “Jet Charge at the LHC”. In: *Phys. Rev. Lett.* 110 (May 2013), p. 212001. DOI: 10.1103/PhysRevLett.110.212001. arXiv: 1209.2421 [hep-ph].

[66] Ian Moult, Lina Necib, and Jesse Thaler. “New angles on energy correlation functions”. In: *JHEP* 12 (2016), p. 153. DOI: 10.1007/JHEP12(2016)153. arXiv: 1609.07483 [hep-ph].

[67] Andrew J. Larkoski, Gavin P. Salam, and Jesse Thaler. “Energy correlation functions for jet substructure”. In: *JHEP* 06 (2013), p. 108. DOI: 10.1007/JHEP06(2013)108. arXiv: 1305.0007 [hep-ph].

[68] Guolin Ke et al. “LightGBM: A Highly Efficient Gradient Boosting Decision Tree”. In: *Advances in Neural Information Processing Systems 30 (NIPS 2017)*. Curran Associates, Inc. URL: `https://proceedings.neurips.cc/paper_files/paper/2017/file/6449f44a102fde848669bdd9eb6b76fa-Paper.pdf`.

[69] Takuya Akiba et al. *Optuna: A Next-generation Hyperparameter Optimization Framework*. 2019. arXiv: `1907.10902 [cs.LG]`.

[70] A. Buckley et al. “LHAPDF6: parton density access in the LHC precision era”. In: *Eur. Phys. J. C* 75 (2015), p. 132. DOI: `https://doi.org/10.1140/epjc/s10052-015-3318-8`. arXiv: `1412.7420 [hep-ph]`.

[71] S. Mrenna and P. Skands. “Automated parton-shower variations in PYTHIA 8”. In: *Phys. Rev. D* 94.7 (2016), p. 074005. DOI: `10.1103/PhysRevD.94.074005`. arXiv: `1605.08352 [hep-ph]`.

[72] DerivationProductionTeam. *Exotics derivation twiki page*. URL: `https://twiki.cern.ch/twiki/bin/view/AtlasProtected/DerivationframeworkExotics`.

[73] Zach Marshall. *Re-re-defining the standard QCD di-jet samples: beginning to like event weights*. ATL-COM-PHYS-2015-417. 2015. URL: `https://cds.cern.ch/record/2016630`.

[74] P. Meade and L. Randall. “Black holes and quantum gravity at the LHC”. In: *JHEP05* 2008 (2008), p. 003. DOI: `10.1088/1126-6708/2008/05/003`. arXiv: `0708.3017 [hep-ph]`.

[75] Luis A. Anchordoqui et al. “Inelastic black hole production and large extra dimensions”. In: *Phys. Lett.* B594 (2004), pp. 363–367. DOI: `10.1016/j.physletb.2004.05.051`. arXiv: `hep-ph/0311365 [hep-ph]`.

[76] De-Chang Dai et al. “BlackMax: a black-hole event generator with rotation, recoil, split branes, and brane tension”. In: *Phys. Rev.* D77 (2008), p. 076007. DOI: `10.1103/PhysRevD.77.076007`. arXiv: `0711.3012 [hep-ph]`.

[77] Eugene Lukacs. “A characterization of the normal distribution”. In: *The Annals of Mathematical Statistics* 13.1 (1942), pp. 91–93.

[78] Robert M. Harris and Konstantinos Kousouris. “Searches for dijet resonances at hadron colliders”. In: *Int. J. Mod. Phys.* A26 (2011), pp. 5005–5055. DOI: 10.1142/S0217751X11054905. arXiv: 1110.5302 [hep-ex].

[79] Matteo Cacciari, Gavin P. Salam, and Gregory Soyez. “FastJet User Manual”. In: *Eur. Phys. J.* C72 (2012), p. 1896. DOI: 10.1140/epjc/s10052-012-1896-2. arXiv: 1111.6097 [hep-ph].

[80] Hongtao Yang. *XML Analytic Workspace Builder*. 2021. URL: https://twiki.cern.ch/twiki/bin/viewauth/AtlasProtected/XmlAnaWSBuilder (visited on 06/22/2021).

[81] Wouter Verkerke and David Kirkby. *The RooFit toolkit for data modeling*. 2003. arXiv: physics/0306116 [physics.data-an].

[82] Will Buttinger. *xRooFit*. 2023. URL: https://gitlab.cern.ch/will/xroofit (visited on 07/24/2023).

[83] V. V. Gligorov et al. *Avoiding biases in binned fits*. 2021. arXiv: 2104.13879 [physics.data-an].

[84] P. Bagnaia et al. “Measurement of Jet Production Properties at the CERN anti-p p Collider”. In: *Phys. Lett.* 144B (1984), pp. 283–290. DOI: 10.1016/0370-2693(84)91822-7.

[85] CDF Collaboration, T. Aaltonen et al. “Search for new particles decaying into dijets in proton-antiproton collisions at $\sqrt{s} = 1.96$ ”. In: *Phys. Rev. D* 79 (Aug. 2009), p. 112002. DOI: 10.1103/PhysRevD.79.112002. arXiv: 0812.4036 [hep-ex].

[86] ATLAS Collaboration. “Search for New Particles in Two-Jet Final States in 7 TeV Proton–Proton Collisions with the ATLAS Detector at the LHC”. In: *Phys. Rev. Lett.* 105 (2010), p. 161801. DOI: 10.1103/PhysRevLett.105.161801. arXiv: 1008.2461 [hep-ex].

[87] CMS Collaboration. “Search for Dijet Resonances in 7 TeV *pp* Collisions at CMS”. In: *Phys. Rev. Lett.* 105 (2010), p. 211801. DOI: 10.1103/PhysRevLett.105.211801. arXiv: 1010.0203 [hep-ex].

[88] ATLAS Collaboration. “A search for new physics in dijet mass and angular distributions in pp collisions at $\sqrt{s} = 7$ TeV measured with the ATLAS detector”. In: *New J. Phys.* 13 (2011), p. 053044. DOI: `10.1088/1367-2630/13/5/053044`. arXiv: `1103.3864 [hep-ex]`.

[89] ATLAS Collaboration. “Search for new phenomena in the dijet mass distribution using pp collision data at $\sqrt{s} = 8$ TeV with the ATLAS detector”. In: *Phys. Rev. D* 91 (2015), p. 052007. DOI: `10.1103/PhysRevD.91.052007`. arXiv: `1407.1376 [hep-ex]`.

[90] ATLAS Collaboration. “Search for new resonances in mass distributions of jet pairs using 139 fb^{-1} of pp collisions at $\sqrt{s} = 13$ TeV with the ATLAS detector”. In: *JHEP* 03 (2020), p. 145. DOI: `10.1007/JHEP03(2020)145`. arXiv: `1910.08447 [hep-ex]`.

[91] Nishu Nishu et al. *Search for New Phenomena in Dijet Events using the complete Run-2 dataset collected with the ATLAS Detector at $\sqrt{s}$ =13 TeV*. Tech. rep. ATL-COM-PHYS-2018-1538. Geneva: CERN, Nov. 2018. URL: `https://cds.cern.ch/record/2646455`.

[92] ATLAS Collaboration. *Recommendations for the Modeling of Smooth Backgrounds*. ATL-PHYS-PUB-2020-028. 2020. URL: `https://cds.cern.ch/record/2743717`.

8 Acknowledgements

First of all, I would like to extend my heartfelt gratitude to my parents for their unconditional love, encouragement, and support during my journey towards this PhD. Without them, I wouldn't have been able to come this far.

I am also thankful to my supervisors, Prof. Shu Li from the Tsung-Dao Lee Institute & Shanghai Jiao Tong University and Prof. Shih-Chieh Hsu from the University of Washington, Seattle, for their invaluable guidance, expertise, and mentorship. Their insightful feedback and patient guidance have been instrumental in shaping the direction of my research and future career. Moreover, this thesis would not have been possible without the collective contributions of my collaborators: Iain Bertram; Ke Li; Ben Nachman; Haoran Zhao; Nishu Nishu; Rongqian Qian; Jack Lindon; Jyoti Prakash Biswal; Davide Melini; Lorenzo Rossini; Reina Coromoto Camacho Toro; Matt LeBlanc.

Thankful to myself for persevering and completing my studies after suffered from the 4-months quarantine, the myocardial anoxia, the loss of a loved one, and the pain of depression.